Title
CHAOS AND RELATED NONLINEAR NOISE PHENOMENA IN JOSEPHSON TUNNEL JUNCTIONS

Author
Miracky, R.F.

Publication Date
1984-07-01

Lawrence Berkeley Laboratory
UNIVERSITY OF CALIFORNIA

Materials & Molecular Research Division

CHAOS AND RELATED NONLINEAR NOISE PHENOMENA IN JOSEPHSON TUNNEL JUNCTIONS

R.F. Miracky
(Ph.D. Thesis)

July 1984

Prepared for the U.S. Department of Energy under Contract DE-AC03-76SF00098

DISCLAIMER

LBL-18193

CHAOS AND RELATED NONLINEAR NOISE PHENOMENA IN JOSEPHSON TUNNEL JUNCTIONS

Robert Foster Miracky
Ph.D. Thesis

Lawrence Berkeley Laboratory
University of California
Berkeley, California 94720

July 1984

Chaos and Related Nonlinear Noise Phenomena in Josephson Tunnel Junctions

by

Robert Foster Miracky

ABSTRACT

The nonlinear dynamics of Josephson tunnel junctions shunted by a resistance with substantial self-inductance have been thoroughly investigated. The current-voltage characteristics of these devices exhibit stable regions of negative differential resistance. Very large increases in the low-frequency voltage noise with equivalent noise temperatures of 10^6 K or more, observed in the vicinity of these regions, arise from switching, or hopping, between subharmonic modes. Moderate increases in the noise, with temperatures of about 10^3 K, arise from chaotic behavior. Both of these conclusions are substantiated by analog simulations. Measurements of the low-frequency spectrum of the hopping noise in one type of junction show a $1/f^2$-dependence, independent of both bias current and temperature. A simple amplifier utilizing the negative differential resistance is found to exhibit a "noise rise."

Analog and digital simulations indicate that under somewhat rarer circumstances the same junction system can sustain a purely deterministic hopping between two unstable subharmonic modes, accompanied by excess low-frequency noise. Unlike the noise-induced case, this chaotic process occurs over a much narrower range in bias current and is destroyed by the addition of thermal noise. The differential equation describing the junction system can be reduced to a one-dimensional mapping in the vicinity of one of the unstable modes. A general analytical calculation of switching processes for a class of mappings yields

the frequency dependence of the noise spectrum in terms of the parameters of the mapping.

Finally, the concepts of noise-induced hopping near bifurcation thresholds are applied to the problem of the three-photon Josephson parametric amplifier. Analog simulations indicate that the noise rise observed in experimental devices arises from occasional hopping between a mode at the pump frequency ω_p and a mode at the half harmonic $\omega_p/2$. The hopping is induced by thermal noise associated with the shunt resistance.

John Clarke
7/26/84

ACKNOWLEDGEMENTS

Numerous people educated, assisted, encouraged, cajoled, entertained, or simply made things more tolerable for, me during my graduate physics career at Berkeley. At the top of the list is my thesis advisor, Professor John Clarke. His knack for staying abreast of both basic and applied physics has been a model for all of his students, not only myself. The egalitarian spirit with which he conducts the laboratory has made the research group an active and exciting place to work in. Special thanks must go out to Wolf Goubau, with whom I worked on several geophysics experiments. His persistence and adherence to fundamentals is unsurpassed in my book. I also wish to express my appreciation to several colleagues: Michel Devoret, Tom Gamble, Roger Koch, Dan Seligson, and Kurt Wiesenfeld. Learning physics, among other things, from such individuals has been both inspiring and humbling. I also appreciate the help I have received from all past and present Clarke group members, especially my office-mate Claude Hilbert.

And then there are the individuals who made the tangible contributions. I am indebted to Professor Edgar Knobloch for helping to fill in the holes in my knowledge of nonlinear dynamics. Professor Ted Van Duzer of the Electrical Engineering Department kindly loaned me the Josephson electronic analog so instrumental in this work. I tip my hat to John Martinis for graciously fabricating the small-area junctions discussed herein. Rita Jones patiently taught me the idiosyncracies of the IBM PC, even when I used up all of her printer ribbons. And, lastly, I wish to thank Gloria Pelatowski for drafting all forty-five figures of this thesis, doing so always with a smile.

Although acknowledgement is hardly necessary, the contributions of my parents and family have been incalculable, despite their being thousands of miles removed during the course of this work.

This work was supported by the Director, Office of Energy Research, Office of Basic Energy Sciences, Materials Sciences Division of the U.S. Department of Energy under Contract Number DE-AC03-76SF00098.

TABLE OF CONTENTS

CHAPTER I

INTRODUCTION

A. General

A current Frontier of Physics is the study of the dynamics of nonlinear systems. Unlike most Frontiers, which are localized at some point on the periphery of Knowledge, Nonlinear Dynamics is a field interwoven throughout the body of Physics, serving as a common theme uniting many of its subspecialties. It is perhaps more appropriate then that Nonlinear Dynamics be called a "Superspecialty". This universal character of Nonlinear Dynamics has stimulated basic research in fields as diverse as fluid dynamics, laser studies, solid state electronics, astrophysics, and even meteorology.

One aspect in particular has received widespread attention: namely, "Chaos." What is it, and why is it important to Physics? Several excellent review papers have been already been written to answer these questions (see, for example, May, 1976; Eckmann, 1981; Ott, 1981), so we shall highlight only a few key points of relevance to our own studies.

Much of the mathematical work in regard to nonlinear systems has been in the area of bifurcation theory. Given some function y which depends not only on an independent variable x, but also on a control parameter μ, $y = y(x,\mu)$, bifurcation theory seeks to answer the question: For what value of μ does the response $y(x,\mu)$ undergo abrupt transitions, where the character of the solution changes drastically, analogous to, say, a phase transition? Needless to say, numerous types of bifurcations are possible. But the most frequently discussed is the "period-doubling" bifurcation. To be more specific, if x is also a continuous and periodic function of time [$y = y(x(t),\mu)$] with fundamen-

tal frequency f_0, a period-doubling occurs if, as μ is varied, the fundamental frequency of y changes from f_0 to $f_0/2$.

Chaos generally arives only after one or more simple bifurcations have already taken place. Simply put, chaos is a **deterministic** response of a nonlinear dynamical system which is nevertheless aperiodic and whose power spectrum possesses broad-band "noise-like" components. Chaos is possible only in nonlinear differential equations which are of at least third-order and autonomous (i.e., no explicit time dependence), or second-order and nonautonomous: The Poincare-Bendixson theorem (Jordan and Smith, 1977) forbids chaotic solutions in second-order, autonomous systems. If we restrict ourselves to dissipative systems, we know from Liouville's theorem that volumes in phase space contract with time. The set of points to which a chaotic flow is attracted, analogous to a limit cycle for simple oscillations, is termed a "strange" attractor, in light of the aperiodicity of chaotic systems.

One of the goals of experimental studies of chaos, including our own, has been to classify in a variety of systems the transitions from simple oscillations to chaotic ones. Theoretical studies have suggested that there are three primary transitions to chaos. First, there is the Feigenbaum (1978, 1979) period-doubling scenario. Here an infinite cascade of individual period-doublings leads to a chaotic state as the control parameter is varied. A number of universal scaling laws govern this transition. The second route to chaos is that of Pomeau-Manneville (1980) intermittency. In this case, quiescent, or "laminar," durations occur in $y(x(t),\mu)$ which are occasionally interrupted by noisy intervals. Again, scaling laws govern the mean times of quiescent periods. Finally, there is the scenario of Newhouse, Ruelle, and Takens (1978).

Here, chaos arises after three so-called Hopf bifurcations, at each of which an incommensurate frequency is added to the spectrum of the response $y(x(t),\mu)$. In our own studies, only the first two of these scenarios are relevant.

One final subject which has received less theoretical attention, but which is very important experimentally, is the role of noise in nonlinear systems, especially those operated near bifurcation points. While chaos is a deterministic phenomenon, existing in mathematical systems without external noise, it is interesting to understand how chaos manifests itself in real physical systems where noise is always present. This is one of the questions addressed in detail in this Thesis.

Large-scale nonlinear systems, such as the earth's atmosphere and plasmas of ionized gases, have been the focus of much of the recent excitement in nonlinear dynamics. However, rich phenomena can be observed in many smaller-scale systems, especially in solid state electronics. Perhaps the most familiar nonlinear electronic device is the p-n semiconductor junction. Recent experiments (Testa, Perez, and Jeffries, 1982) have uncovered very interesting behavior which occurs when a p-n junction is placed in series with a resistor and inductor, and driven with a sinusoidal voltage. It was observed that many of the same effects found in simple one-dimensional mappings of the interval $[x_{n+1} = f(x_n),\ 0 \leq x_n \leq 1]$, such as period-doubling bifurcations, chaos, intermittency, and crises, were also observable in this physical system.

Another nonlinear electronic device is the Josephson junction (Josephson, 1962). Many practical devices have been developed which rely on its extreme nonlinearity, including magnetometers based on Superconducting QUantum Interference Devices (SQUID's) (Clarke, 1980),

digital circuits (Zappe, 1983), voltage standards (Taylor et al., 1967), and parametric amplifiers (Claeson, 1983). Although there have been extensive analyses of the operation of these devices, it is only recently that the possibility of **chaotic** behavior in Josephson devices has been considered (Huberman, Crutchfield, and Packard, 1980; Pedersen and Davidson, 1981; Kautz, 1981a, 1981b; D'Humieres et al., 1982). These studies have been practically motivated, as it has been suggested that chaos is the source of the excess noise found in Josephson parametric amplifiers (more on this in Chapter IV). Much of this work has been numerical, and directed toward an ac-biased, resistively shunted junction, whose equation is identical to that of the driven, damped pendulum:

$$\ddot{\delta} + (1/\sqrt{\beta_c})\dot{\delta} + \sin\delta = i_{dc} + i_{ac}\cos(\omega t). \qquad (1.1)$$

These researchers found that for $\beta_c = 25$, $\omega \leq 1$, $i_{dc} = 0$, and $i_{ac} \leq 1$, period doubling, intermittency, phase-locking, as well as chaos, were indeed possible in Eq. (1.1). One question still remains: What implications do these simulation results have on experiments performed on real junctions?

B. Thesis Outline

The subsequent chapters of this Thesis address three distinct topics concerned with the rather complicated nonlinear dynamics of Josephson tunnel junctions. In Chapter II we explore in considerable detail the variety of phenomena observable in a dc-biased Josephson tunnel junction shunted by a capacitance and a resistance having a non-negligible self-inductance. We were motivated to perform these experiments by the desire to answer the following questions:

1) Is chaos observable in an actual Josephson junction system?
2) Which, if any, of the familiar scenarios are possible?
3) Are there any new transitions to chaos in this system?
4) What is the role of thermal noise in the observed behavior?
5) How well does the lumped circuit model account for the observed phenomena?

In addition to obtaining the answers to these questions, several new phenomena were also observed. The current-voltage characteristics of such junctions show stable regions of negative dynamic resistance, unlike junctions with zero inductance. Experimental measurements of the noise resulting from both chaos as well as an unexpected hopping process will be discussed, along with the analog simulations which allowed us to interpret these results. We also present and interpret measurements of the noise power spectrum of the hopping noise in one type of junction. We conclude this Chapter with a description of studies of the low-frequency amplification and noise properties of a junction biased on a negative resistance.

In Chapter III we describe an unanticipated phenomenon occurring in the above junction system. In the process of trying to understand the

origin of excess noise observed in actual Josephson tunnel junctions, it was discovered that analog simulations for comparable parameters exhibited an apparently deterministic 1/f-type power spectrum of the noise over two decades at low frequencies. Further simulations, both analog and digital, have confirmed the origin of this noise in the governing circuit equation, and, unlike the noise-induced hopping described in Chapter II, this effect was destroyed by the addition of external noise. We describe how this noise can be explained in terms of hopping between two unstable oscillations. We then go to to show that the long-time dynamics of this hopping are determined exclusively by the character of a one-dimensional mapping of one of the junction variables in the vicinity of one of the unstable orbits.

Chapter IV reexamines the performance of the three-photon Josephson parametric amplifier in light of the phenomenon of noise-induced transitions near bifurcations, uncovered in the work of Chapter II. This device has historically been plagued with an heretofore unexplained excess noise phenomenon, termed "noise rise." Simulations of the complete amplifier circuit, including the resonant coupling circuit, will be detailed, and the results interpreted in light of recent developments in nonlinear dynamics.

CHAPTER II

CHAOS IN JOSEPHSON TUNNEL JUNCTIONS

A. Introduction

As mentioned in Chapter I, there have been extensive analytical and numerical studies of the ac-driven Josephson junction system, Eq. (1.1). On the experimental side, however, little has been done. It has proved rather difficult to perform controlled experiments which can be modelled by Eq.(1.1), using conventionally fabricated Josephson junctions, while still operating at frequencies for which the lumped circuit model is an appropriate one. Only very recently have the first experimental results of chaos in this system been reported (Octavio and Readi Nasser, 1984). Still, the Josephson junction, by virtue of its simple nonlinearity, remains an attractive system through which universal aspects of chaos can be studied. In principle, any Josephson circuit possessing enough reactive elements to make the governing equation third-order should exhibit chaos, and thus provide a vehicle for the study of its appearance in a real physical system.

One such circuit is a dc-biased resistively shunted Josephson tunnel junction, whose external resistance has a non-neglible self-inductance associated with it (Fig. 1). Although there have been no previous experiments demonstrating chaos in this circuit, there have been several studies of other, simpler nonlinear phenomena. One of these is a type of "relaxation oscillation" which can arise under certain circumstances. As an understanding of these relaxation oscillations is fundamental to an appreciation of chaos in this system, we shall briefly highlight this topic.

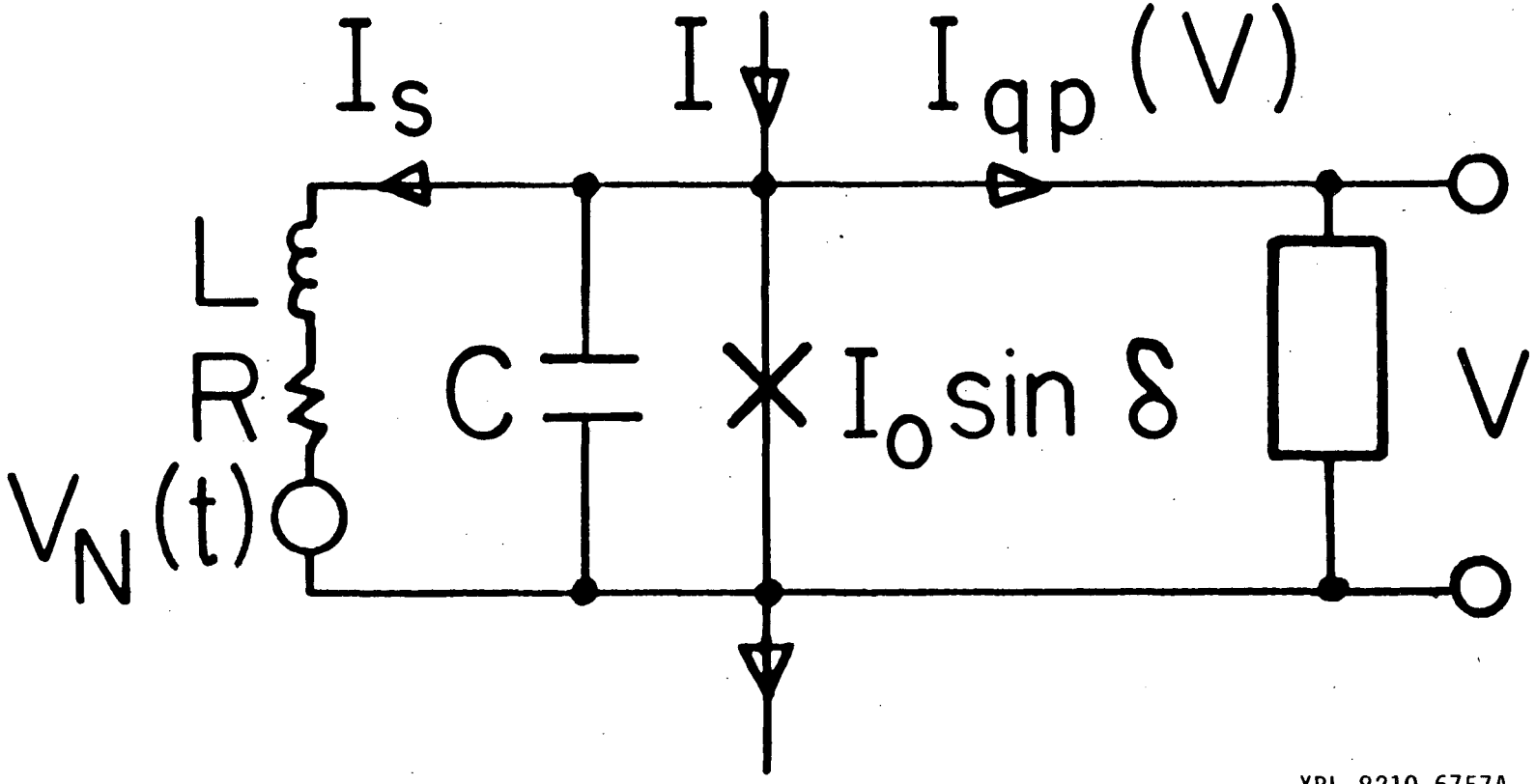

XBL 8210-6757A

Figure 1. Schematic representation of a Josephson tunnel junction with critical current I_0 and self-capacitance C shunted with an external resistance R which has a self-inductance L; I_{qp} is the quasiparticle tunneling current and V_N is the Johnson voltage noise associated with the resistance.

Generally speaking, a relaxation oscillation is a periodic phenomenon in a nonlinear system, which consists of at least two oscillations or transients with different characteristic times. Greater insight into the physics of relaxation oscillations in this particular system can be gained by referring to a mechanical pendulum analog of the Josephson junction (Fig. 2). In this model, a rigid pendulum (corresponding to the junction) is connected at its pivot point to an axle around which is applied a constant torque T (dc bias current). The connecting axle, however, is not rigid, but has torsional elasticity, obeying Hooke's law with force constant K. This energy storage element corresponds to the inductance of Fig. 1. If the applied torque exceeds the critical value Mgl (critical current), the pendulum will rotate. For large torques the pendulum phase angle θ (junction phase angle δ) increases monotonically, as a good, or "grabbing," automobile clutch rotates when it is torqued. However, the presence of the torsional elasticity in the axle allows the pendulum to be out of phase with respect to the axle postion at which the torque is applied, measured by the angle ϕ. As a consequence, for lower values of the torque, the pendulum will occasionally fall backwards (negative junction voltage), as a "slipping" clutch might. For relatively small K values ("twisty" axle), the pendulum may undergo damped natural oscillations for a number of cycles, until the torsional axle has been "wound up," and the driving torque can again be transferred to the pendulum itself. The origin of subharmonic relaxation oscillations is now apparent: Several 2π-revolutions of ϕ may occur before a complete oscillation period (including both rotations and relaxations of the pendulum) has elapsed.

Relaxation oscillations occurring in resistively-shunted Josephson

MECHANICAL ANALOG

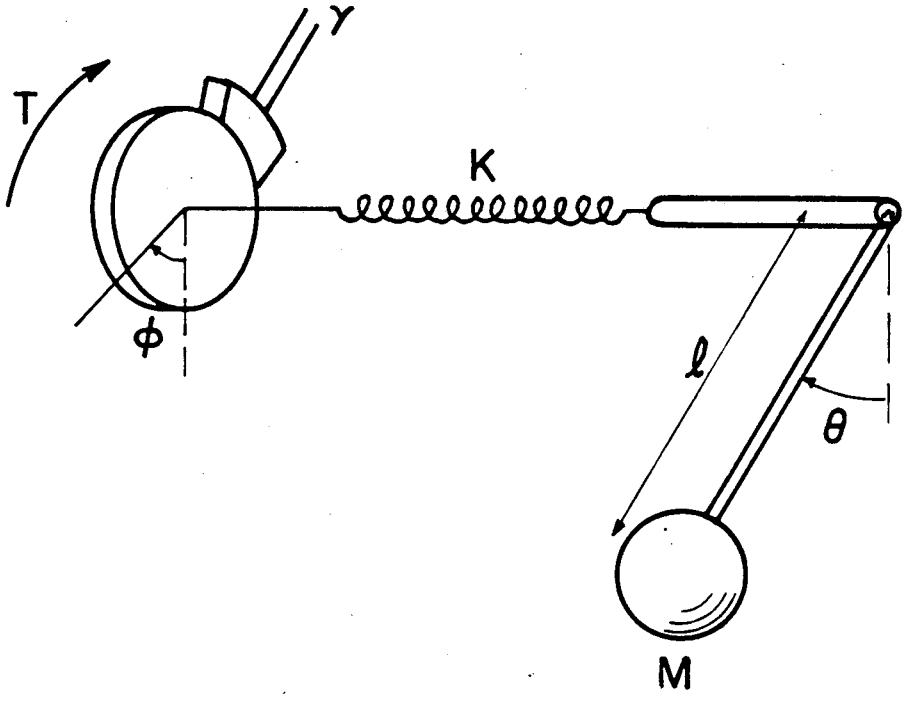

Correspondence:

$$\theta \longleftrightarrow \delta$$
$$Mg\ell \longleftrightarrow I_0$$
$$M\ell^2 \longleftrightarrow (\Phi_0/2\pi)C$$
$$\gamma \longleftrightarrow (\Phi_0/2\pi)\,1/R$$
$$K \longleftrightarrow (\Phi_0/2\pi)\,1/L$$
$$T \longleftrightarrow I$$
$$\gamma\dot{\phi} \longleftrightarrow I_s$$

XBL 846-7018

Figure 2. Pendulum mechanical analog of the Josephson junction circuit of Fig. 1.

point contacts were first reported by Zimmerman and Silver (1967). Several years later Sullivan et al. (1970) observed subharmonic oscillations (i.e., the fundamental period of oscillation is an integer times the Josephson frequency, determined from the mean voltage), and invoked feedback originating with the inductor to interpret them. The authors confined themselves to the zero-capacitance limit, offering no precise analytical or numerical results. Dempsey, Levinsen, and Ulrich (1975) considered the finite capacitance case and showed numerically that extensive subharmonic behavior is possible for a wide range of parameters. They suggested that the key factor for the existence of relaxation oscillations is that the amounts of energy which can be stored in the electric and magnetic fields of the circuit components must be roughly comparable to the junction coupling energy. No aperiodic behavior was reported.

Several researchers have constructed devices to take advantage of these interesting properties. Taur and Richards (1975) achieved amplification at 5 MHz, as well as mixing at 36 GHz, for junctions biased along a negative differential resistance region appearing in the DC current-voltage characteristic. More recently, Calander, Claeson, and Rudner (1981a, 1981b) have conducted extensive studies of relaxation oscillations at 10 GHz as well as injection locking of relaxation oscillations to weak external signals. To interpret the phenomena they observed, the authors appealed to a simple model which considers the voltage response separately in the zero- and finite-voltage states. The duration of the former is determined by the L/R time constant of the shunt, and typically results in lengthly quiescent periods (as $L/R >> 1/f_J$, where f_J is the Josephson frequency). When the current through

the junction reaches the critical current, the junction switches briefly to the voltage state before rapidly relaxing back to the supercurrent state. It is these two distinct time constants which allow the resulting periodic response to be classified as a relaxation oscillation. Calander, Claeson, and Rudner (1981a,1981b) verified the model through its dependences on L/R and I/I_0. Unfortunately, the devices did not perform well enough to warrant continued investigation: Excessive noise temperatures were observed (10^3 K $\leq T_N \leq 10^5$ K), as well as saturation at low powers.

This same circuit also enters into considerations of ultra-high performance dc SQUID's. Koch, Van Harlingen, and Clarke (1982), in performing calculations and measurements of quantum noise in single junctions and dc SQUID's, demonstrated that for junctions near the quantum limit with finite shunt inductances, there are significant increases in the low-frequency noise mixed down from frequencies near harmonics of the Josephson frequency. They conjectured that such effects were due to nonlinear interactions between the LC-resonance and Josephson frequencies. Obviously, for successful low-noise performance of such devices, chaos, which in many practical situations is indistinquishable from other, natural sources of noise, must be avoided.

Aside from these device implications, a significant motivation for conducting studies of chaos in this system is the relative ease with which meaningful experiments can be performed. First, the junction is dc-biased, affording a precise measurement of the bias current, which serves as the "control parameter" in this system. Secondly, the range of junction parameters for which complicated behavior, including chaos, is expected, is easily accessible. (The justification for this belief

is discussed below.) Finally, both noise measurements and spectral analysis can be performed at radio frequencies, unlike the ac-driven experiment, which requires microwaves.

After developing the equations of motion for this junction system, we discuss experiments on two types of Josephson tunnel junctions, and analog simulations conducted to interpret the results (Miracky, Clarke, and Koch, 1983). We then describe measurements of the spectrum of the low-frequency noise in these junctions. Finally, we address the question of the usefulness as low frequency amplifiers of the negative resistance regions appearing in the I-V characteristics.

B. Equations of Motion

We begin with the Stewart-McCumber lumped circuit model of a dc-biased Josephson tunnel junction (Barone and Paterno, 1982). A Josephson tunnel junction consists of two superconductors separated by a thin insulating barrier through which pairs of electrons (Cooper pairs) are able to tunnel coherently (Josephson, 1962). This flow of electrons constitutes a supercurrent, which is equal to $I_0 \sin\delta$, where δ is the phase difference of the order parameters in the separate superconductors. A shunting capacitance C must be included in the model to account for the overlap of the two electrodes. The distinct process of single-electron, or quasiparticle, tunneling is represented by a current $I_{qp}(V)$, which is a nonlinear function of the voltage V across the junction. For the types of junctions we shall consider here, the quasiparticle current is generally very small. Most importantly, we focus on those devices to which an external shunting resistance R has been added which has a self-inductance L.

The resulting circuit is shown in Fig. 1, and is governed by the

equations

$$I = I_0 \sin\delta + \hbar C/2e\,\ddot{\delta} + I_S + I_{qp}, \tag{2.1}$$

and

$$\hbar/2e\,\dot{\delta} = RI_S + L\dot{I}_S + V_N, \tag{2.2}$$

where V_N is the thermal voltage noise generated by the resistance R. If we introduce a dimensionless time variable

$$\tau = (2\pi I_0 R/\Phi_0)t, \tag{2.3}$$

where $\Phi_0 = h/2e$ is the flux quantum, Eqs. (2.1) and (2.2) become

$$i = \sin\delta + \beta_C\,\ddot{\delta} + i_S + i_{qp}, \tag{2.4}$$

and

$$\dot{\delta} = i_S + \beta_L\dot{i}_S + v_N, \tag{2.5}$$

with $i=I/I_0$, $i_S=I_S/I_0$, $i_{qp}=I_{qp}/I_0$, $v_N=V_N/I_0R$, $\beta_C=2\pi I_0R^2C/\Phi_0$, $\beta_L=2\pi LI_0/\Phi_0$. The dot now denotes differentiation with respect to τ.

Neglecting the quasiparticle current and the noise voltage, we combine Eqs. (2.4) and (2.5) to give the third-order equation

$$\beta_L\beta_C\dddot{\delta} + \beta_C\ddot{\delta} + \dot{\delta}(1 + \beta_L\cos\delta) + \sin\delta = i. \tag{2.6}$$

The system is seen to depend on three dimensionless parameters: β_L, β_C, and i. The first two are fixed with respect to a given junction, but the continuously variable third one serves conveniently as the "control parameter." If one makes the correspondences listed for the pendulum analog in Fig. 2, an identical equation can be derived for it.

It is helpful to have expressions in these dimensionless units for the characteristic frequencies of the system. The junction plasma frequency Ω_P is $1/\sqrt{\beta_C}$, the LC-resonance frequency Ω_{LC} is $1/\sqrt{\beta_L\beta_C}$, the Q of the LC-resonance is $\sqrt{(\beta_L/\beta_C)}$, and the L/R-time constant τ_{LR} is β_L. Thus, for $\beta_L \sim 10$ and $\beta_C \sim 0.1$, $\Omega_P \sim 3$, $\Omega_{LC} \sim 1$, $Q \sim 10$, and $\tau_{LR} \sim 10$.

Henceforth in this chapter we shall study the dynamics of Eq. (2.6)

only by means of analog and digital simulations. We leave for the Appendix an analytic calculation of the first period-doubling bifurcation as i is reduced.

C. Experiment

We shall now describe experiments performed to observe chaotic behavior in thin-film Josephson tunnel junctions. We begin with a description of the junction samples, focusing on both the parameter specification and the fabrication procedures. Next the several experimental measurements made on such junctions will be outlined. The results of these measurements will then be presented and discussed. The interpretation of the results on the basis of analog simulations follows in the next section.

1. Choice of Parameters

The first step is to determine suitable junction parameters. A naive physical understanding of the origin of chaos in this particular circuit may assist in the task. One might expect significant deviations from the resistively shunted junction model (RSJ) when the energy stored in the inductance is of the same order as the junction coupling energy:

$$LI_0^2/2 \geq I_0\Phi_0/2\pi, \tag{2.7a}$$

implying

$$\beta_L \geq 2. \tag{2.7b}$$

In addition, let us assume that the LC-resonance plays a crucial role. The intrinsic junction plasma resonance should then be damped out sufficiently to ensure that it does not dominate. This implies that $\beta_C \leq 1.0$, giving us a second criterion.

Two types of junctions were studied: "small-area" [10 μm × 10 μm -- Fig. 3(a)] and "large-area" [400 μm × 350 μm -- Fig. 3(b)]. The former are more interesting from a device perspective, as they are similar to

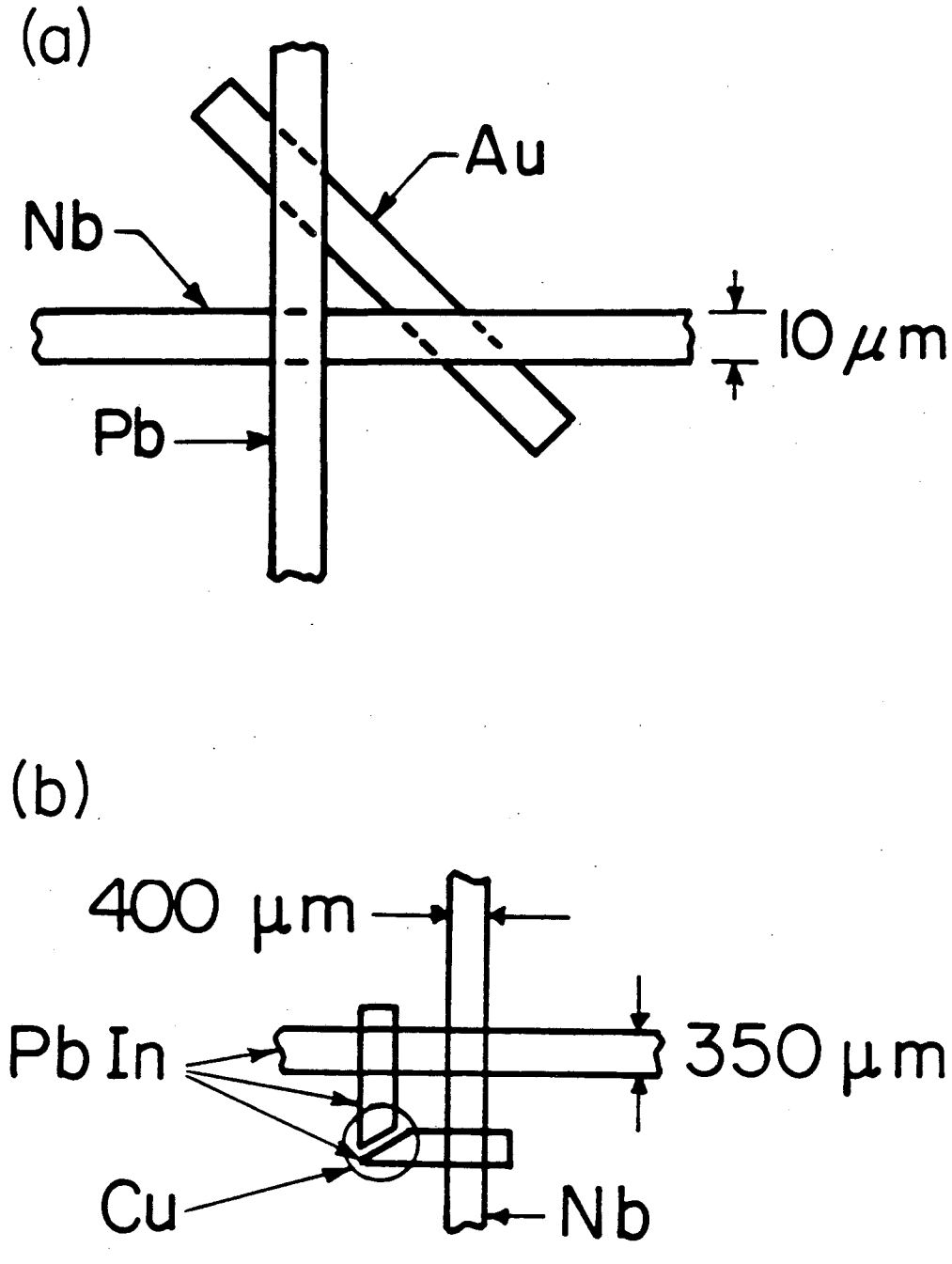

XBL 846-7112

Figure 3. (a) Small- and (b) large-area Josephson tunnel junctions shunted by an external resistance with substantial self-inductance. In (b), the loop is overlaid with a superconducting PbIn ground plane, insulated from the loop with a layer of SiO.

the types of junctions used in such devices as dc SQUID's, while the latter are more suitable for direct observation of subharmonic behavior and chaos, as will be seen. In general, the parameters β_C and β_L can be tuned by altering I_0 with an applied magnetic field. This technique is very effective for large-area junctions, but of limited use for the small-area junctions. Still another constraint is the need to keep the critical current as large as the device technology permits. The chaotic "noise" power (really "signal" for this experiment) increases with I_0, as power spectral densities scale like $I_0\Phi_0R/2\pi$. The technology of small-area junctions restricts their critical currents to the range 0.1 to 1.0 mA. The only real flexibility in altering parameters of the small-area junctions then is in varying the size of the shunt loop. Combining Eq. (2.7a) with the estimate $L \sim \mu_0 d$, where d is the shunt loop size, implies that, for a junction with a critical current of 500 μA, d should be greater than 1 μm. This is just the size scale for the small-area junctions, so by changing the placement of the shunt [the Au strip in Fig. 3(a)], d could be varied sufficiently to give a range of β_L between about 1 and 10. Typical parameters for these junctions were $I_0 = 0.5$ mA, $C = 4$ pF, $R = 0.4$ Ω, and $L = 4$ pH, from which we obtain $\beta_C \approx 1.0$ and $\beta_L \approx 6.0$. From measurements of $I_{qp}(V)$ made on unshunted junctions fabricated in the same batch as shunted ones, we estimate that $\alpha = R/R_{sg} \approx 5\times10^{-3}$, where R_{sg} is the quasiparticle resistance below the gap voltage.

A more systematic procedure was followed in choosing junction parameters in the case of the large-area junctions. The primary constraint was the requirement that the characteristic voltage oscillations (Josephson oscillations) have their fundamental frequency, or low order

subharmonic (with subharmonic number between, say, 1 and 5), at radio frequencies below 1 GHz. This was motivated by the desire to simpify the amplification and spectral analysis of these signals, and to avoid the need for microwave technology. Parasitic effects generally increase with frequency, but they are of even greater concern here as one must attempt to match 50 Ω to the low-impedance (≲ 1 Ω) tunnel junction. The scale of the Josephson frequency is set by:

$$f_J = (2e/h)\ (I_0R) = (484\ \text{MHz}/\mu\text{V})\ (I_0R). \qquad (2.8)$$

If one requires that $f_J \lesssim 1$ GHz, this implies that $I_0R \lesssim 2\mu V$.

Secondly, we require that $\beta_C = 2\pi I_0R^2C/\Phi_0$ be $\lesssim 0.3$, to keep the junction overdamped. [It should be noted that this limit may not be appropriate for other types of devices, such as voltage-controlled oscillators based on the relaxation oscillation mode of the junction. (Silver, Sandell, and Wilcox, 1983).] Expressing this in terms of the junction capacitance per unit area C_R and critical current density j_0 we have:

$$\beta_C = (2\pi/\Phi_0)\ (RI_0)^2\ (C_R/j_0). \qquad (2.9)$$

For thermally-oxidized Nb-Pb junctions, $C_R \approx 0.044\ \text{pF}/(\mu\text{m})^2$ (Barone and Paterno, 1982). For $\beta_C \approx 0.1$ and $RI_0 \approx 2\mu V$, we have that

$$j_0 \approx 5.3 \times 10^{-9}\ \text{A}/(\mu\text{m})^2 = 5.3 \times 10^{-3}\ \mu\text{A}/(\mu\text{m})^2. \qquad (2.10)$$

Generally one keeps $I_0 \lesssim 1$ mA, in order to reduce self-field effects (i.e., the interaction between the magnetic field produced by a bias current through a junction on the junction critical current itself.) This implies that the junction area A_J should be

$$A_J = 1.9 \times 10^5\ (\mu\text{m})^2, \qquad (2.11)$$

or that the length of one side of the junction should be 430 μm. Thus we have that junctions should be approximately 400 μm on a side, a

situation easily achieved without the need for photolithography.

We have shown that the shunt resistance R should be ≈ 2 mΩ, a rather small resistance for thin films of either Au or Cu with dimensions on the order of 100 μm. The requirement that $\beta_L \geq 10$ implies, for I_0 = 1 mA, that L ≥ 3 pH, or, if L ~ $\mu_0 d$, that d ≥ 2.6 μm: This is clearly impractical if the film widths are 400 μm. However, by covering the entire junction and shunt loop area with a superconducting ground plane, the effective inductance can be reduced by roughly the ratio of the strip width to the ground plane/strip separation, a number on the order of several hundred to one thousand. It is more convenient to be able to vary both R and L separately, in contrast to the arrangement with the small-area junctions. The configuration used to do this is shown in Fig. 3(b). The resistance is formed by the Cu film which bridges the narrow (~ 75 μm) gap in the otherwise superconducting PbIn shunt loop. The resistance is thus controlled by the Cu film thickness, and the inductance by the size of the shunt loop.

Typical parameters for the large-area junctions were I_0 = 1 mA, C = 5 nF, R = 2 mΩ, and L = 5 pH, giving $\beta_C \approx 0.1$ and $\beta_L \approx 15$. Separate measurements on unshunted junctions give $\sigma = R/R_{sg} \approx 1\times10^{-3}$.

2a. Sample preparation: Small-area junctions

The small-area junctions were fabricated in nine batches of six junctions on a 50 mm diameter Si wafer, using photolithographic lift-off techniques. First, a Au strip about 10 μm wide and 160 nm thick was deposited, followed by a Nb strip about 200 nm thick. The lift-off for the Nb strip was performed, and the resist patterned for the PbIn (5 wt.%In) strip. The wafer was diced to give nine individual substrates, each with six junctions; each substrate was processed individually from

this point. The surface of the Nb was cleaned by ion-milling in Ar, and oxidized with a radio frequency discharge in an ArO_2 mixture. The PbIn film, about 300 nm thick, was then deposited and lifted off.

2b. Sample preparation: Large-area junctions

The large-area junctions were prepared three at a time on 3"x1" glass microscope slides. For the first set of film depositions, a cleaned sample slide was placed in an evaporator and the chamber pressure was reduced to less than 3×10^{-6} Torr. The shunt was formed by evaporating onto the slide through aperture masks first Cu and then PbIn (10 wt.% In). The circular Cu film was typically 290 nm thick. The L-shaped PbIn strip, about 170 nm thick, was positioned such that the corner coincided with the Cu spot [see Fig. 3(b)]. A 3-mil wire placed between the PbIn mask and substrate itself masked a fine gap in the PbIn where it overlapped the Cu, thus forming the shunt resistance. By varying the Cu film thickness, resistances ranging from 1 to 40 mΩ could be obtained.

After bleeding the vacuum chamber to atmospheric pressure, the sample was removed and mounted underneath a mask which defined the base junction electrode. The sample mount was then transferred to a vacuum chamber containing a Sloan sputtergun. The system was evacuated to a base pressure of less that 10^{-6} Torr. Argon was then bled into the system for about ten minutes, after which time the ionization discharge was initiated by increasing the chamber pressure to about 30 μm while applying 400 V across the sputtergun electrodes. Once the discharge had commenced, a steady current of about 4 A was maintained by controlling the Ar pressure, as the Nb was sputtered onto the substrate. Three minutes of sputtering resulted in a film thickness of about 150 nm.

After bleeding the system to atmospheric pressure, the sample was then immediately transferred to a oven for the thermal oxidation in air of the Nb surface to form the tunneling barrier. This was done at approximately 130°C for about seven minutes; different barrier thicknesses could be grown by varying the oxidation time. After completing the oxidation, the sample was then transferred back to the evaporator where the counter electrode and remaining films were deposited, again through aperture masks. First, the counter electrode of PbIn, approximately 170 nm thick, was evaporated. A 130 nm-thick layer of SiO was then deposited, to serve as insulation between the junction electrodes and a 210 nm-thick PbIn ground plane which covered the entire junction area. Finally, a 130 nm-thick disk of SiO was evaporated atop the ground plane to serve as passivation. Once removed from the vacuum chamber, the slide was diced into individual junction samples, ready for testing.

3. Measurements

The sample junctions were tested individually after being mounted at the end of a 100-cm long insert and immersed in a 5-liter capacity superinsulated fiberglass cryostat containing liquid helium. Twisted pairs of wires ran the length of the insert and were press-mounted to the junction electrodes to permit the several electrical measurements. First, current-voltage (I-V) characteristics were measured in the case of the small-area junctions by slowly sweeping the current bias, and measuring the resulting voltage. In the case of the large-area junctions, current-dV/dI measurements were made instead, as the low junction voltage signals made I-V measurements using conventional low-noise amplifiers (such as the Brookdeal 5004) difficult.

In addition to the dc I-V (I-dV/dI) measurements, the noise at

approximately 100 kHz was measured for both types of junctions, as a function of current bias. A schematic of the circuit used to perform this measurement is contained in Fig. 4(a). A cooled resonant tank circuit, consisting of a coil of inductance L_T wound from Nb wire and a capacitance C_T, was connected directly across the junction under test. This arrangement transformed the junction impedance in order to better match the relatively low junction impedance (1 Ω in the case of the small-area junctions and 2 mΩ in the case of the large-area ones) to the somewhat higher optimal noise matching impedance (5 kΩ) of the Brookdeal 5004 preamplifier. Equivalently, the voltage across the capacitor is amplified by a factor $Q = \omega L_T/R_T$, which was approximately 60 (500) for the small- (large-) area junctions, in a bandwidth ω_0/Q, where $\omega_0 = 1/\sqrt{(L_T C_T)}$. The output of the preamplifier was then fed into a PAR HR-8 lock-in amplifier, used in the low-frequency mixer mode: A reference signal set to $\omega_0/2\pi$ multiplied the input, producing a narrow bandwidth signal at zero frequency which could be monitored with a RMS meter. This signal, suitably filtered of high frequencies, is a direct measure of the noise at 100 kHz. It is more convenient to express it in terms which allow ready comparison to other sources of noise, such as Johnson noise originating in the shunt resistance R. Hence we define an equivalent noise temperature T_N in the bandwidth B of the tank circuit as:

$$T_N = \langle V_N^2 \rangle / 4 k_B R B, \tag{2.12}$$

where $\langle V_N^2 \rangle$ is the mean square voltage noise monitored with the RMS meter.

A second measurement was made in the case of the large-area junctions, illustrated in Fig. 4(b). A 50-Ω semi-rigid coaxial cable was

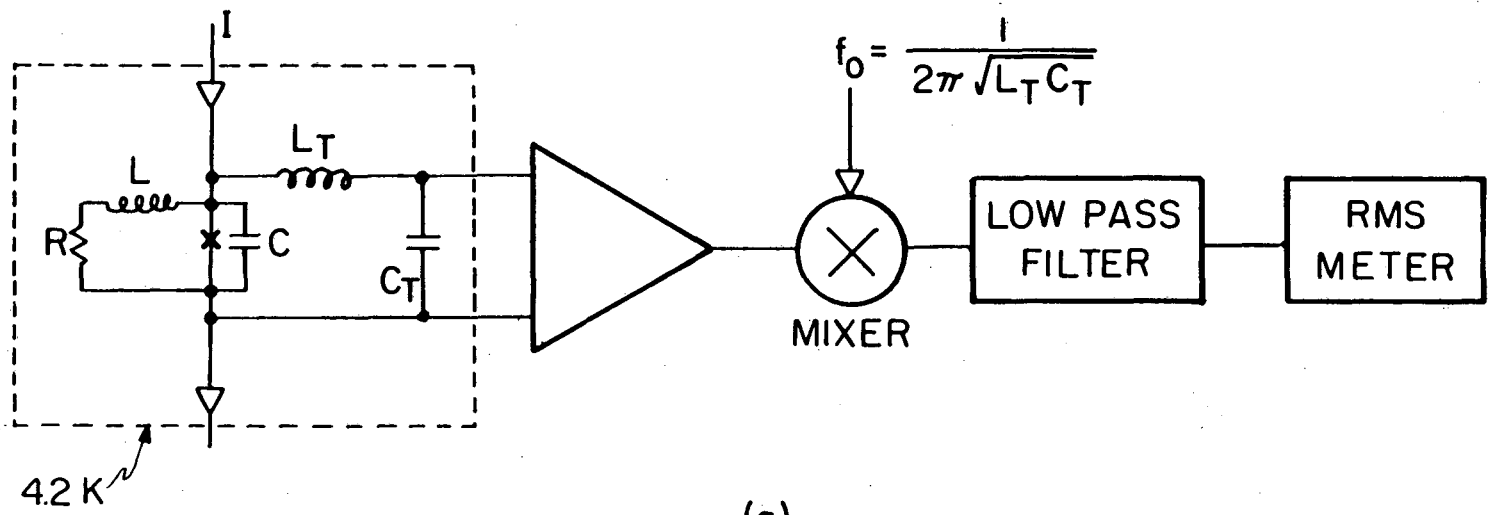

Figure 4. Block diagrams of experiments to measure (a) low-frequency noise, and (b) high-frequency signals in the types of junctions illustrated in Fig. 3. L_T and C_T represent components of an external tank circuit.

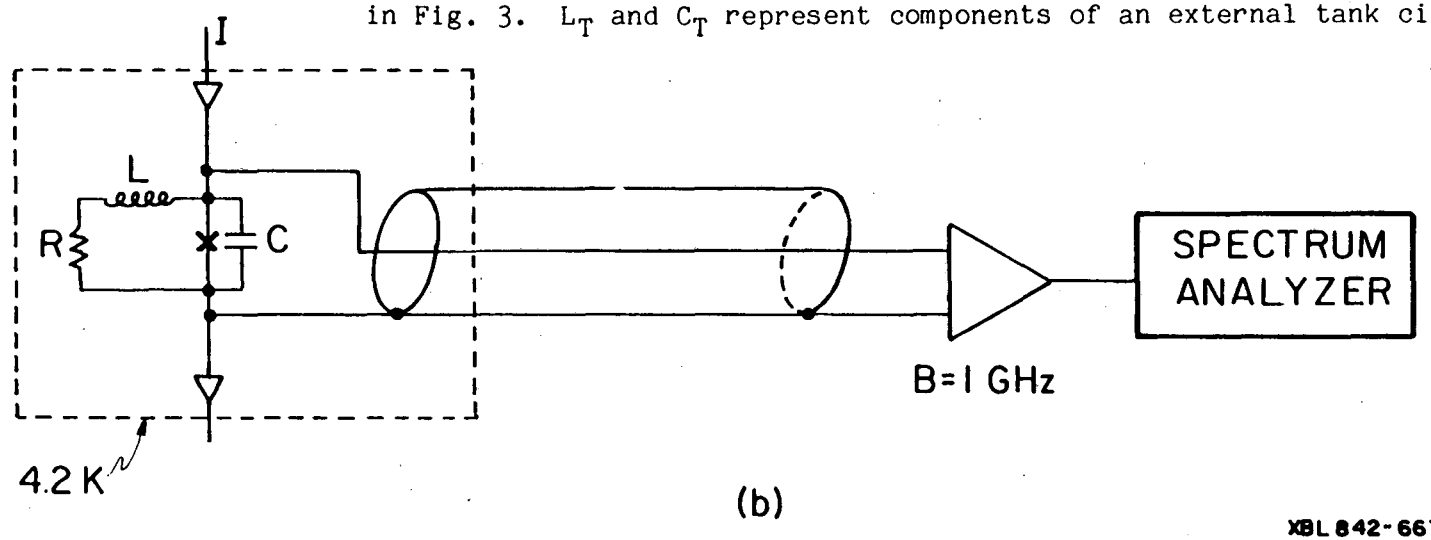

XBL 842-6675

connected directly across the junction voltage electrodes and, at the top of the cryostat, to a wide-band (1 GHz) amplifier, with a noise figure of about 1.3 dB. The output of the amplifier was fed into a HP 3559A spectrum analyzer, allowing the spectrum of the voltage oscillations to be monitored.

D. Results

In Fig. 5 we show the results of the low-frequency measurements [Fig. 4(a)] from a typical large-area junction. Here we plot together the noise temperature T_N and the differential resistance dV/dI as a function of I, in order to determine whether excess noise is correlated with structure on the I-V characteristic. The differential resistance shows a great deal of structure, including regions of negative differential resistance (NDR). The noise also shows considerable structure, and one can distinguish three types of features. First, there are regions of bias current for which the junction has a noise temperature below the system noise temperature, 70 K. Second, there are a number of fairly broad regions for which the noise temperature varies from about 300 K at high bias currents to about 2300 K at currents just above the critical current. Third, there are a number of narrow but exceedingly noisy peaks for which the noise temperature is greater than 5×10^4 K, the saturation value for the electronics; in other measurements we have determined that these peaks may have noise temperatures as high as 10^6 to 10^8 K. These noise spikes are usually in the vicinity of negative resistance regions, but do not appear consistently at any specific feature: For example, the spike at 1.56 mA in Fig. 5 occurs near dV/dI = 0, while that at 4.32 mA occurs near a minimum in dV/dI.

Results from another, similar large-area junction, one with a some-

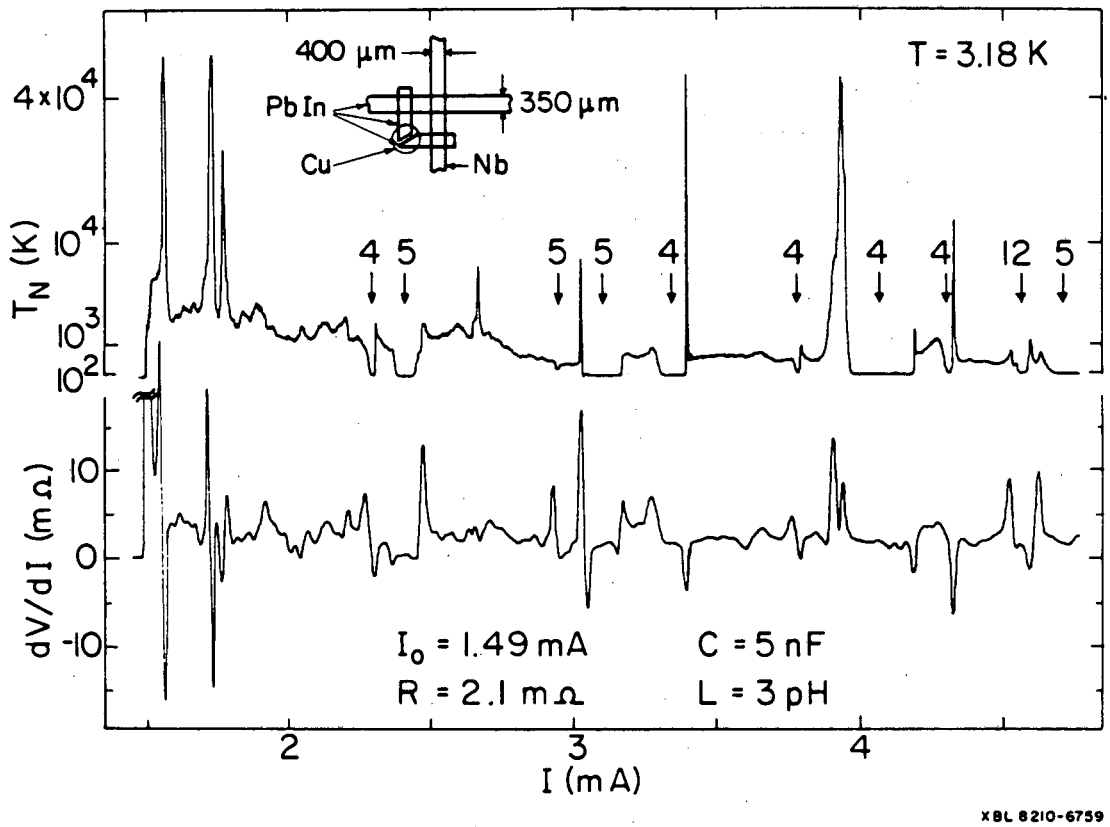

Figure 5. T_N (upper) and dV/dI (lower) vs I (for increasing I) for a typical large-area junction with $\beta_C \approx 0.11$, $\beta_L \approx 12$, and $\Gamma = 8.9\times10^{-5}$. The numbers indicate order of subharmonics. T_N was measured in a bandwidth of 244 Hz about 117 kHz. Inset shows junction configuration.

what lower critical current, are contained in Fig. 6. Although the structure observed here in both the noise temperature and differential resistance graphs is noticeably different from that in Fig. 5, the same four aspects are observed: bias points of negative differential resistance, regions of low noise ($T_N < 32$ K, the system noise level here), broad intervals where $T_N \sim 3\times10^2$ K, and large spikes where $T_N \sim$ 3000 K. In this case, the noise spikes are sometimes but by no means always associated with local maxima in the differential resistance.

To investigate further the origin of this structure we performed the high-frequency signal measurement of Fig. 4(b). Because of the extreme impedance mismatch between the junction (2 mΩ) and the semi-rigid-coax/preamplifier system (50 Ω), the preamplifier noise temperature was very high, about 3×10^6 K. In the regions of very low noise for both junctions, we were able to observe stable subharmonic oscillations of the Josephson frequency. By separately measuring the dc voltage V_{dc} across the junction with a low-noise voltmeter (Fluke 845 AB) and the lowest frequency present in the spectrum analyzer output, f_1, the subharmonic number n is determined from the relation:

$$n = V_{dc}/(\Phi_0 f_1). \tag{2.13}$$

These numbers are indicated in Figs. 5 and 6. Such subharmonic oscillations are in fact the relaxation oscillations discussed in Sec. A. In regions of bias current where the junction noise temperature was of the order of 10^3 K, the subharmonic spectral components vanished, but the noise temperature of the high-frequency amplifier was far too high for us to make any observations of the nature of the noise at these frequencies.

We believe the large noise spikes generally arise from switching, or

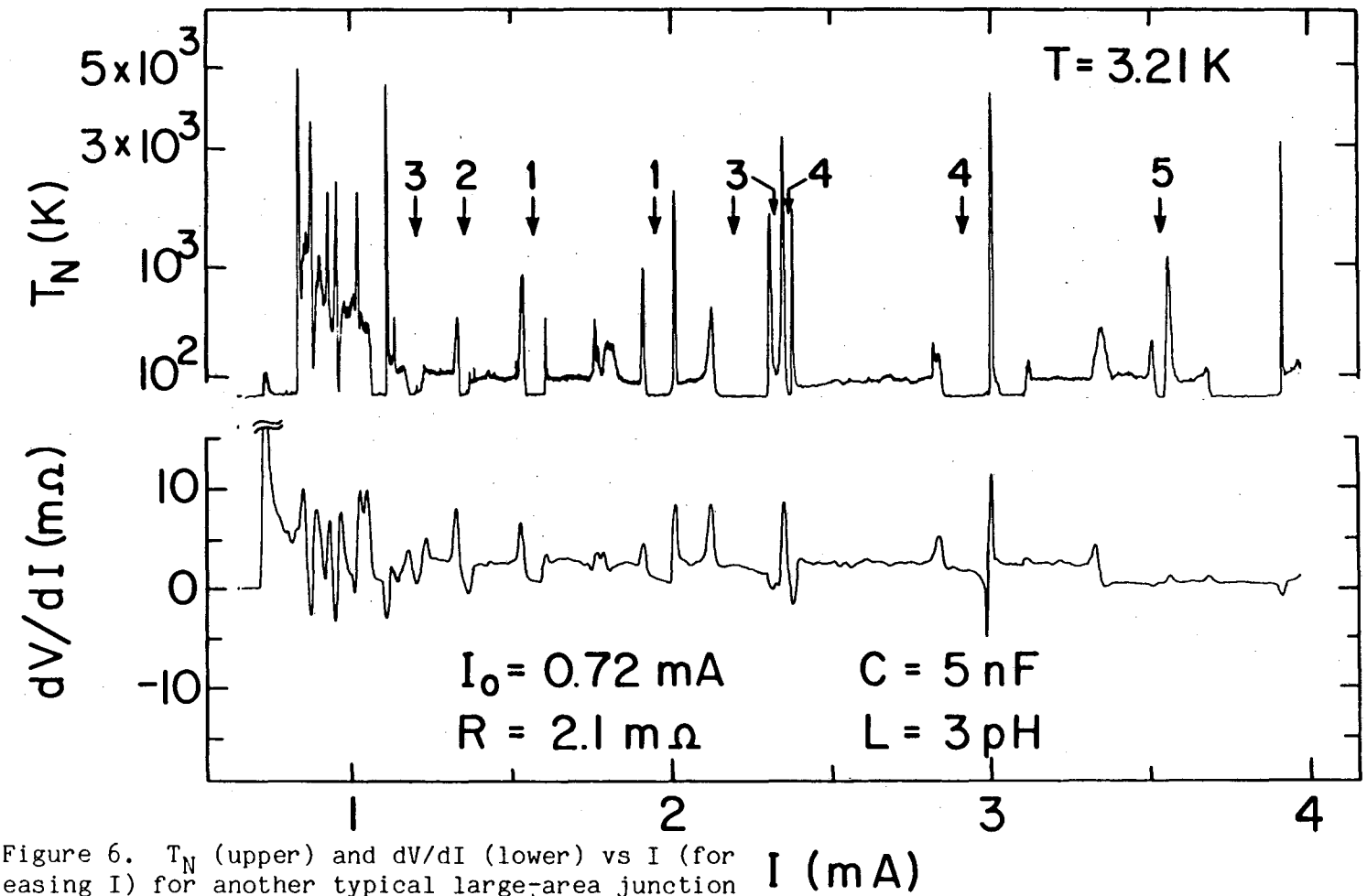

XBL834-5504

Figure 6. T_N (upper) and dV/dI (lower) vs I (for increasing I) for another typical large-area junction with $\beta_C \approx 0.05$, $\beta_L \approx 7$, and $\Gamma = 1.9\times10^{-4}$. The numbers indicate order of subharmonics. T_N was measured in a bandwidth of 244 Hz about 117 kHz.

hopping, between two different oscillatory modes. As evidence of this, Fig. 7 shows two well-defined peaks at 335 and 377 MHz observed when a different junction was biased on a large noise spike. As one sweeps the bias current through the region where the noise spike occurs, one observes first one peak, then the growth of the second peak as the first one shrinks, and finally the disappearance of the first peak. For bias points where only a single peak was observed, no excess low frequency noise was measured. Thus, the junction is apparently hopping between two subharmonic relaxation modes, giving rise to copious levels of noise at frequencies below the characteristic switching frequencies. Switching between subharmonic and "noisy" modes (T_N - 10^3 K) can also occur, as is suggested by the appearance of noise spikes on the boundaries between noise-free and moderately noisy regions in Figs. 5 and 6. The connection between this moderately noisy region and chaos is made on the basis of simulations, to be discussed in Sec. E of this chapter.

I-V characterisitcs and low-frequency noise measurements were similarly obtained for several small-area junctions. Figures 8 and 9 are two representative examples, for slightly different values of R and I_0. Here the bottom voltage scale refers to the I-V characteristic (curve on right in figure), and the top noise temperature scale is a measure of the low-frequency noise (curve on left). (Note: the T_N scale in Fig. 8 is linear in $\sqrt{\langle V_N^2 \rangle}$, while that in Fig. 9 is logarithmic in $\langle V_N^2 \rangle$.) As the junction resistance is much larger here than in the large-area junctions, a smaller tank circuit Q, typically 57, was needed to optimally match the junction to the preamplifier. In general, much less structure is apparent in the I-V characterictics for the small area junctions, compared with curves from the large-area ones. For the junctions dis-

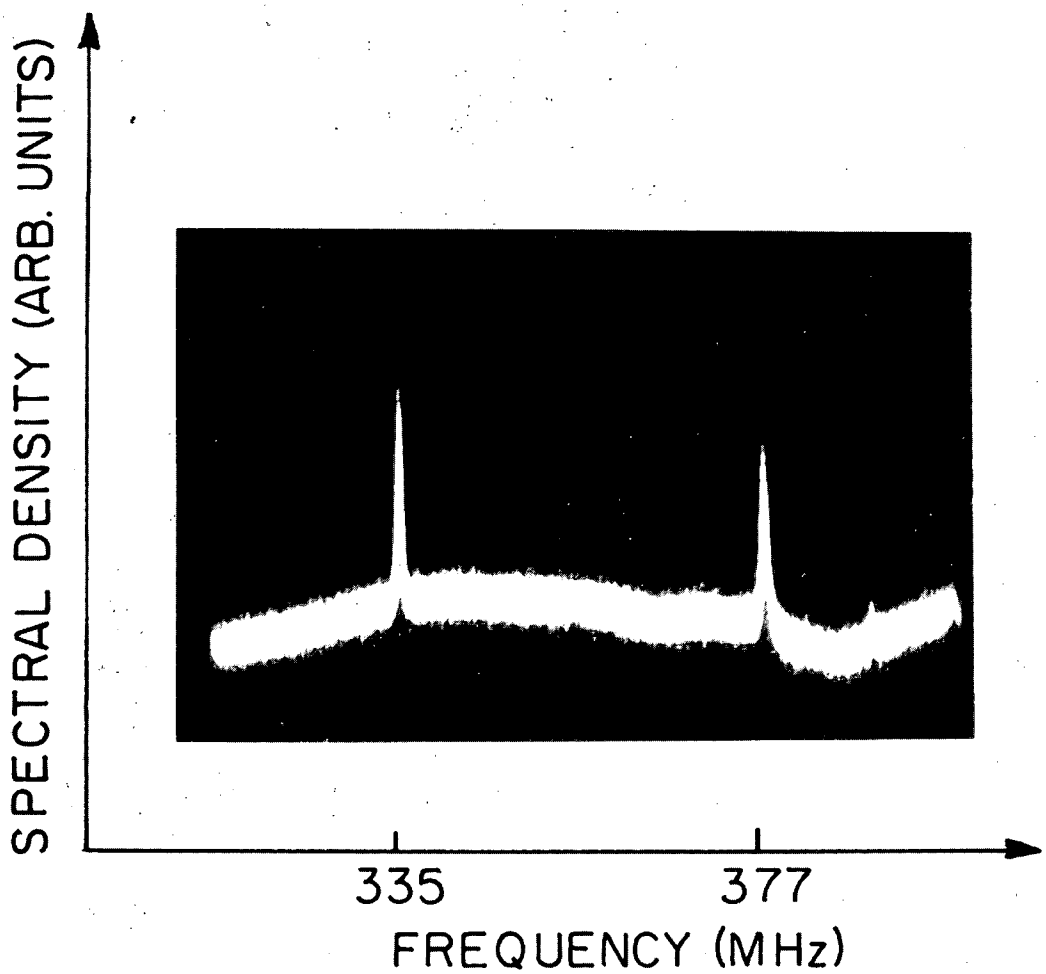

XBB 820-9646

Figure 7. Spectral density of the voltage across another large-area junction at 4.2 K with I_0 = 2.35 mA, I = 6.68 mA, C ≈ 5 nF, R = 1.7 mΩ, and L ≈ 3 pH, giving $\beta_C \approx 0.10$, $\beta_L \approx 21$, and $\Gamma = 7.5\times10^{-5}$.

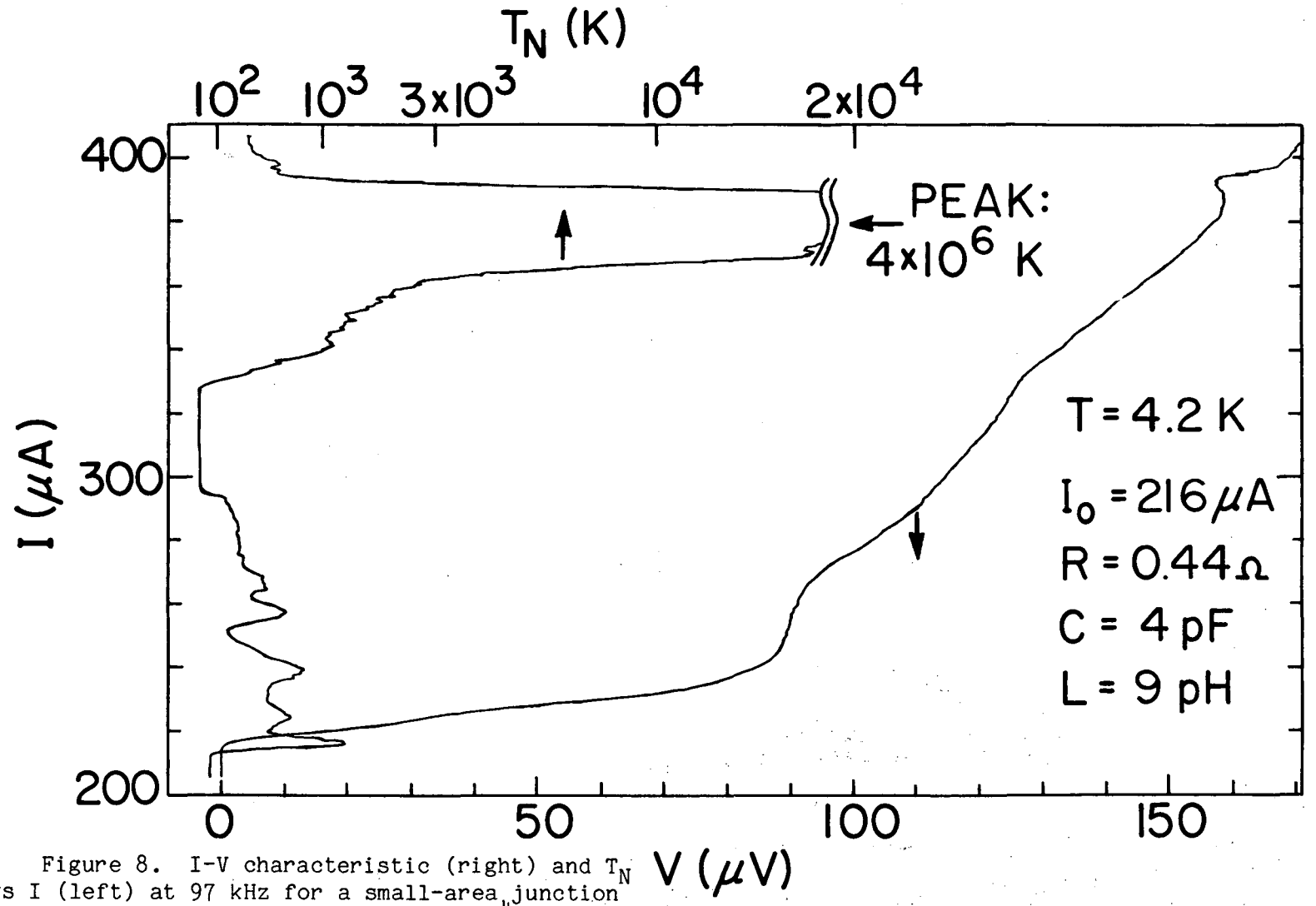

Figure 8. I-V characteristic (right) and T_N vs I (left) at 97 kHz for a small-area junction with $\beta_C \approx 0.5$, $\beta_L \approx 6$, and $\Gamma = 8.1\times10^{-4}$. T_N was measured at a reduced frequency of 3.4×10^{-7}.

XBL834-5503

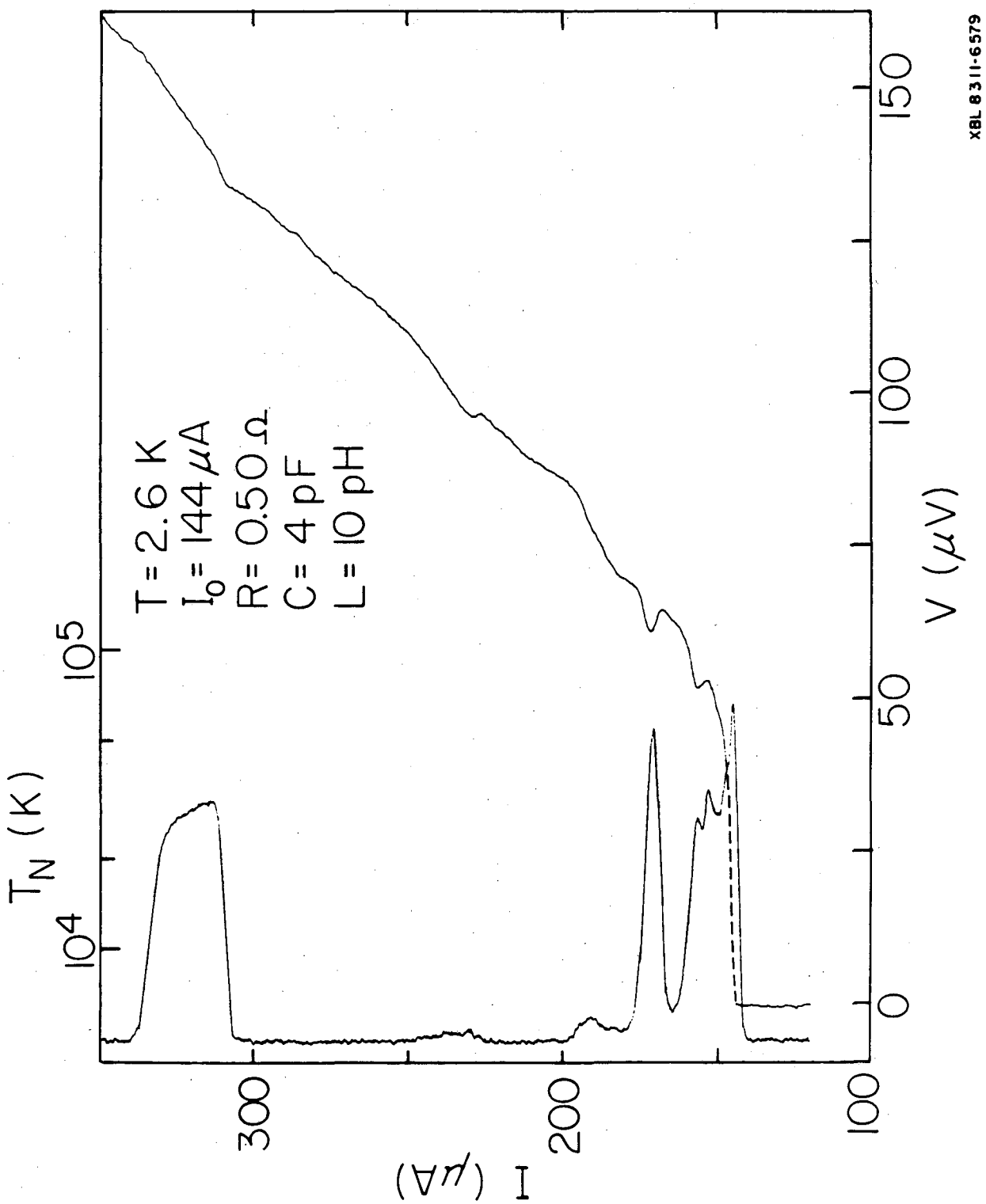

Figure 9. I-V characteristic (right) and T_N vs I (left) at 97 kHz for another small-area junction with $\beta_C \approx 0.4$, $\beta_L \approx 4$, and $\Gamma = 7.6\times10^{-4}$. T_N was measured at a reduced frequency of 4.4×10^{-7}.

cussed here, the significant structure is confined to rather high bias currents (390 μA for Fig. 8 and 320 μA for Fig. 9), and bias currents just above the critical current. For intermediate bias currents (320 μA to 330 μA in Fig. 8 and 200 μA to 300 μA in Fig. 9) there is little structure on the I-V characteristics, as well as no noise above the baseline (system) noise levels.

A general correlation between structure in the I-V characteristic and enhanced noise is evident in both Figs. 8 and 9. It seems that wherever a negative resistance appears, noisy spikes with 10^4 K $\leq T_N \leq 10^6$ K are observed at nearby bias points. In Fig. 8, the noise exceeds 4×10^6 K at 380 μA, just below a substantial negative resistance. In Fig. 9, the noise is greater than 5×10^4 K at 175 μA, near the voltage minimum (dV/dI = 0) of a prominent negative resistance region. The same is true for I ≈ 155 μA. Conversely, in both figures, wherever the noise is only "moderate" ($\leq 10^3$ K), little structure appears. This is true for I between 220 μA and 300 μA in Fig. 8 and I ≤ 200 μA in Fig. 9. However, as for the large-area junctions, there does not seem to be a unique correspondence between the excess noise and the structure of the I-V characteristic. Further interpretation of these features will be made in the discussion of analog simulation results.

On the basis of these measurements we see that some similar phenomena are observed in the small-area junctions as in the large-area ones: negative resistance; and low, moderate, and high noise levels. There is, however, one significant difference. Although the extent in bias current over which structure and noise are observed is smaller in the small-area junctions, the actual bias ranges where dV/dI < 0 are generally greater for the small-area junctions. In fact, without a large

enough series resistor added to the tank circuit, the tank circuit can spontaneously oscillate at such points. The potential for using such a negative resistance as an amplifier will be discussed in Sec. G.

E. Analog Simulations

In order to shed more light on the behavior observed experimentally, we have simulated the junction circuit of Fig. 1 using an electronic analog. (The advantages of analog simulations over digital computations are speed and economy. Analog studies allow one to delineate more quickly the general behavior possible in a multi-dimensional parameter space. Digital computations, with their greater precision, are best suited when particular parameter values warrant closer scrutiny.) To represent the bare junction we used a commercially-available circuit (the Model JA-100, manufactured by Philip Gillette and Associates of Beaverton, Oregon). A block diagram of this circuit is contained in Fig. 10. Rather than realizing the traditional phase-lock loop analog circuit, this circuit actually integrates the voltage to obtain the phase δ, then produces a terminal current approximately proportional to $\sin \delta$. The advantage of this circuit over the phase-lock loop is that an rf reference frequency (~ 100 kHz) is not needed, thus avoiding potential cross-talk problems.

It was essential to use an active circuit (constructed from operational amplifiers) to represent the inductance of Fig. 1. Since the voltage-to-frequency factor ("Φ_0") is 10^{-4} V sec for the junction analog, for $I_0 = 100$ μA and $\beta_L = 10$ an inductance $L = \beta_L \Phi_0 / 2\pi I_0 = 2$ H is needed. Such an inductance is quite difficult to obtain from a passive, room-temperature component, with a resistance low enough to maintain a reasonable β_C value (~ 0.1). The circuit used to achieve this induc-

Figure 10. Block diagram of the electronic circuit used to represent the Josephson junction in the analog simulations. The complete circuit is manufactured by Philip Gillette and Associates of Beaverton, Oregon.

$$I_J = I_0 \sin \delta$$

$$V_J = \frac{K}{2\pi} \dot{\delta}$$

$$K = 4 V_{max} \tau = 10^{-4} \text{ V sec}$$

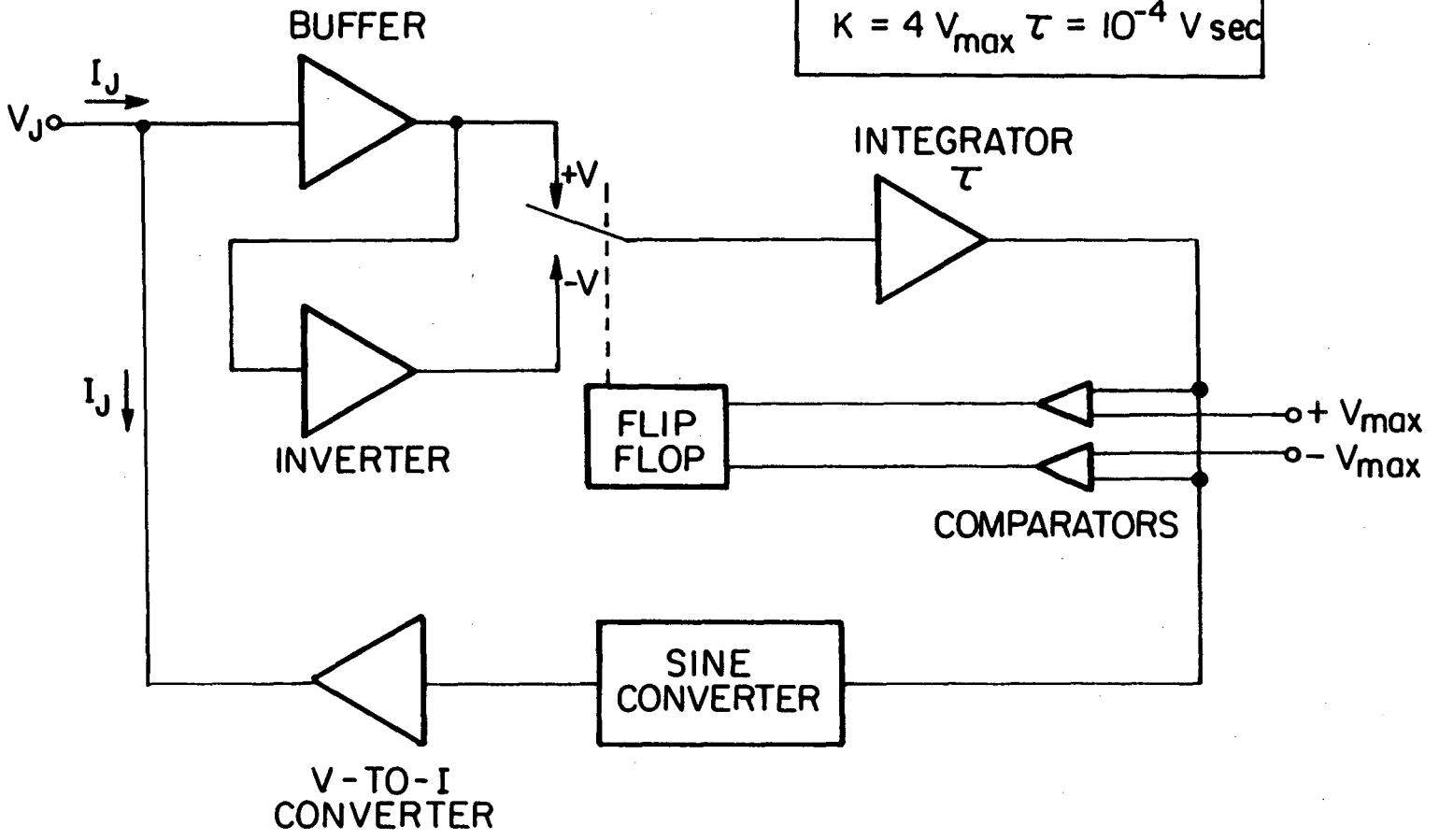

XBL842-6677

tance is an example of a "gyrator," and is illustrated in Fig. 11. Here, the terminal voltage is fed into an integrator with time constant τ, whose output drives a voltage-to-current converter. The current produced is then fed back into the input in a way which does not depend on the source impedance. The terminal impedance is then proportional to $j\omega\tau$, which is precisely the form needed to represent an inductance. A circuit so constructed could easily represent inductances ranging from 10^{-3} H to 30 H ($10^{-2} \leq \beta_L \leq 10^2$), with low losses.

We added to the junction analog and the active inductance a combination of active and passive components to represent the remaining elements of the model. A hybrid analog-digital circuit was constructed to produce a filtered, pseudo-random sequence of voltage pulses to represent the Johnson noise V_N of Eq. (2.2). The output voltage level was calibrated and made continuously variable to provide a wide range of Γ values. R and I_0 were fixed at 630 Ω and 100 μA, respectively, and different values of capacitors were interchanged to achieve a range of β_C values. Finally, a voltage-to-current converter, attached to the JA-100 unit, was biased with a battery to supply the dc-bias current.

Figure 12 is a typical set of solutions for $\beta_C = 0.25$, and $\beta_L = 8.0$. The left-hand column shows the voltage across the junction ($\dot{\delta}$) vs time for four values of bias current, while the right-hand column shows the corresponding phase portrait, $V = \Phi_0 \dot{\delta}/2\pi$ vs $I_0 \sin\delta$. In (a), the solution is the Josephson oscillation with period one, and the corresponding phase portrait is a single closed loop that repeats each time δ evolves through 2π. In (b), a bifurcation has occurred to a period two solution, and the phase portrait contains two loops. In (c), a second bifurcation has occurred to a period four solution, while in (d) the

SIMULATED INDUCTANCE (GROUNDED)

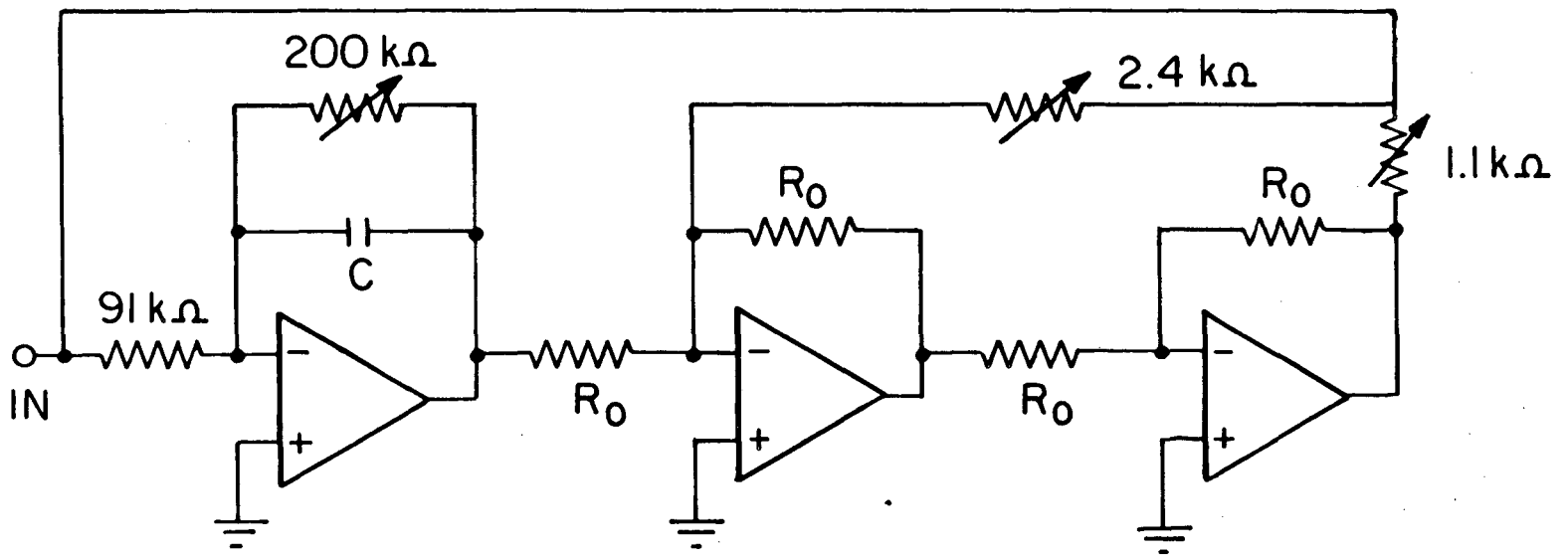

$R_0 = 3.46\ k\Omega \pm 0.1\%$

Equivalent to:

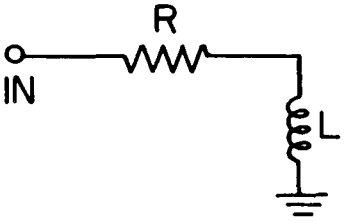

Where: $R = 500\ \Omega$, $L(H) = C(\mu F) \times 100$

Figure 11. Circuit schematic for the active grounded inductance used in the simulations of the Fig. 1 circuit.

XBL 846-7072

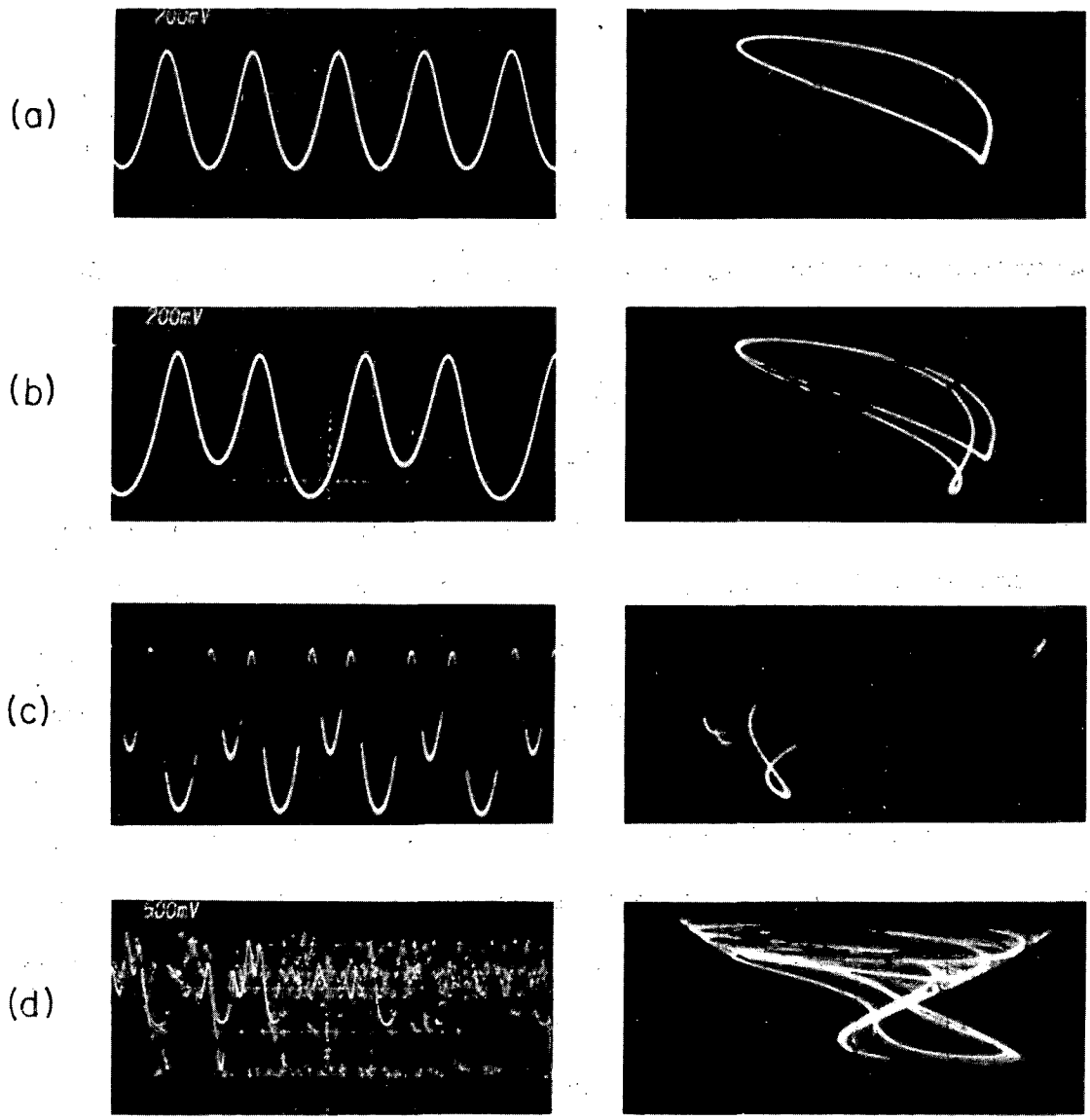

XBB 834-3499

Figure 12. Voltage ($\dot{\delta}$) vs time (left-hand column) and voltage ($\dot{\delta}$) vs junction current ($I_0 \sin\delta$, right-hand column) for the analog simulator with $\beta_C = 0.25$, $\beta_L = 8.0$, and $\Gamma = \Gamma_{sys}$: (a) period one, (b) period two, (c) period four, and (d) chaos. The bias current was reduced in going from (a) to (d).

system has become chaotic. This is an illustration of a Feigenbaum (1978, 1979) period-doubling sequence to chaos.

In Figs. 13 and 14 we show I-V characteristics and low-frequency noise measurements obtained from the simulator for two sets of parameters, chosen to approximate those of the experimental large-area junctions of Figs. 5 and 6 respectively. In so much as the same qualitative features are present in both figures, we shall discuss in detail only Fig. 13. The curve on the right is an I-V characteristic (in dimensionless units) and the one on the left is the noise temperature measured in a bandwidth of 10 to 50 Hz corresponding to frequencies between 24 and 120 MHz for the experimental junction; 117 kHz for the real junction corresponds to 0.049 Hz for the analog.

Although there is certainly not a one-to-one correspondence between the simulations and the real junction, the simulations enable us to understand the general features. The numbers associated with the I-V characteristic indicate the subharmonic numbers which were observed at the corresponding bias point; the filled circles denote bifurcation points. Notice that stable subharmonics were observed only in regions where there was no low-frequency noise. Although the first period-doubling cascade as the bias current is reduced is not apparent from the graph, the full cascade followed by chaos (as exemplified in Fig. 12) was observed to arise for these parameters. As the bias current is further reduced, the system exhibits Pomeau-Manneville intermittency (1980), followed by tangent bifurcations to limit cycles of even or odd periodicity. In the theory of one-dimensional mappings with single quadratic maxima, there is an explicit sequence in which stable limit cycles of period n should first appear as the control parameter is

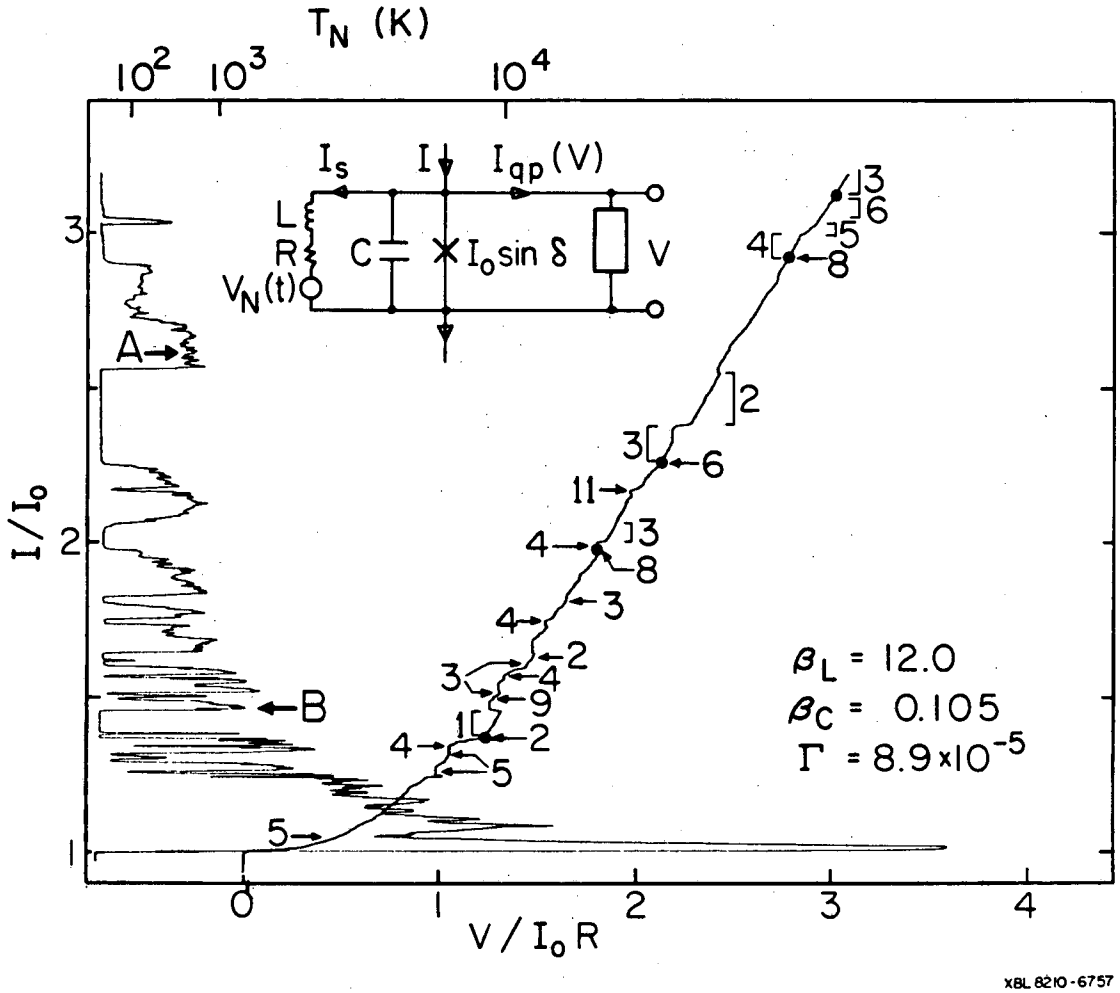

Figure 13. T_N and V/I_0R vs I/I_0 (for increasing I) for analog junction with $\beta_C = 0.105$, $\beta_L = 12.0$, and $\Gamma = 8.9 \times 10^{-5}$. Noise was measured at frequencies between 10 and 50 Hz. Solid circles indicate bifurcation points. Inset shows model of junction.

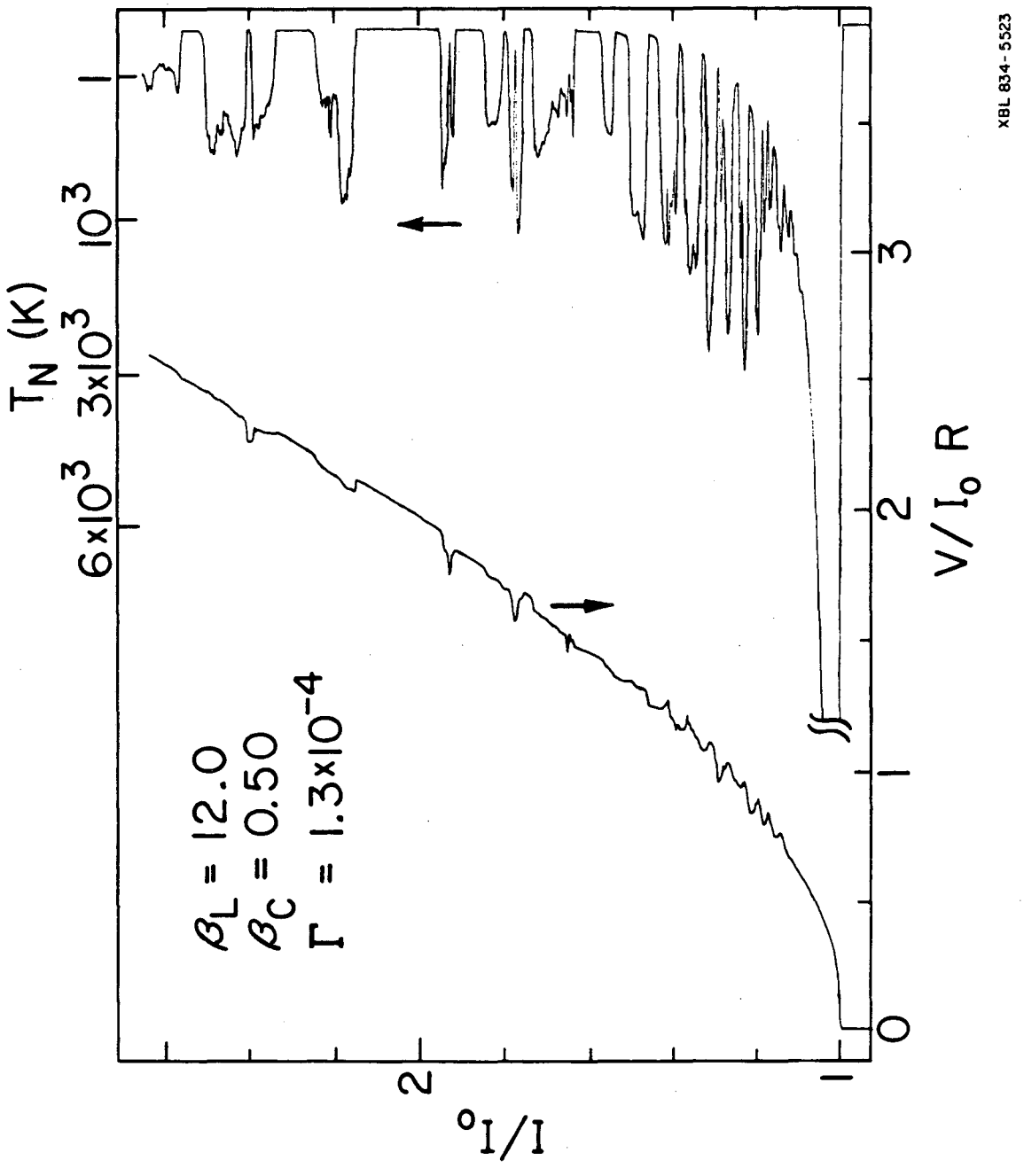

Figure 14. T_N and V/I_0R vs I/I_0 (for increasing I) for analog junction with $\beta_C = 0.05$, $\beta_L = 12.0$, and $\Gamma = 1.3\times10^{-4}$. Noise was measured at frequencies between 10 and 50 Hz.

varied monotonically (Metropolis, Stein, and Stein, 1973). The behavior we observe in our junction simulations as the bias current is reduced does not appear to fit this simple picture, suggesting that a reduction of this third-order system to a one-dimensional mapping of the type analyzed by Metropolis, Stein, and Stein (1973) may not be possible. However, numerical studies we describe in Chapter III demonstrate that a different type of one-dimensional mapping does exist near the onset of type III Pomeau-Manneville intermittency, for certain parameter values. Finally, the lack of order in the appearance of periodic windows indicates that the basins of attraction are probably quite complicated, and that the observed behavior may depend crucially on the amount of external noise present. Results from digital simulations (Koch, Miracky, and Clarke, 1984) are in excellent agreement with those from the analog.

Notice in both Figs. 5 and 6 that the very large noise temperatures ($\geq 10^5$ K) measured in the real junctions are not present in the bandwidth of the noise measurements in Figs. 13 and 14. For the real junctions, the noise measurements in Figs. 5 and 6 were performed at reduced frequencies, $f/(2\pi I_0 R/\Phi_0)$, of 1.2×10^{-5} and 2.6×10^{-5}, respectively, while for the simulations the reduced frequency of the measurements spans the range 2.5×10^{-3} to 1.3×10^{-2}. The lack of a large noise peak in this portion of the analog spectrum suggests that switching noise is greater at much lower reduced frequencies.

In both Figs. 13 and 14 the chaotic noise has a noise temperature of of typically 600 K at the higher bias currents, increasing somewhat as the bias current is lowered. In addition, we see large levels of noise, sometimes with noise temperatures as high as 10^6 K, over relatively narrow ranges of current. To illustrate the chaotic and hopping behav-

ior, in Fig. 15 we plot the spectral densities of the voltage at the points A and B of Fig. 13. In Fig. 15(a), the noise due to chaos is plotted for no injected noise and for an injected noise equivalent to 3.18 K. (The intrinsic, system noise temperature of the analog was estimated to be such that $\Gamma_{sys} \approx 3\times10^{-7}$.) The broadened peak at high frequencies is from a residual subharmonic mode. The noise at low frequencies is white with a noise temperature of about 700 K, and is relatively unaffected by the presence or absence of thermal noise. In Fig. 15(b), the noise temperature of the junction in the absence of thermal noise was below the noise temperature of the measurement system. The addition of thermal noise greatly enhanced the noise temperature at low frequencies, where T_N increases approximately as 1/f to a value of about 10^5 K at 0.1 Hz. In this particular instance, the bias point is at a metastable subharmonic mode, but is sufficiently close to a chaotic regime that transitions between tne subharmonic mode and the chaotic regime can be induced by the added thermal noise.

Analog simulations were also made for parameters approximately equal to those of the experimental small-area junction of Fig. 8; the results are contained in Fig. 16. Again, the I-V characteristic is plotted on the right, and the low-frequency noise (T_N) in the bandwidth between 2.5×10^{-3} and 1.3×10^{-2} dimensionless units appears on the left. As with the data from the real junctions, there are several significant differences between the small- and large-area junction results, such as less overall structure and fewer regions of excess noise. However, the equivalent dimensionless frequency of the noise measurements for the small-area junctions is 3.4×10^{-7}, which is inaccessible even with the

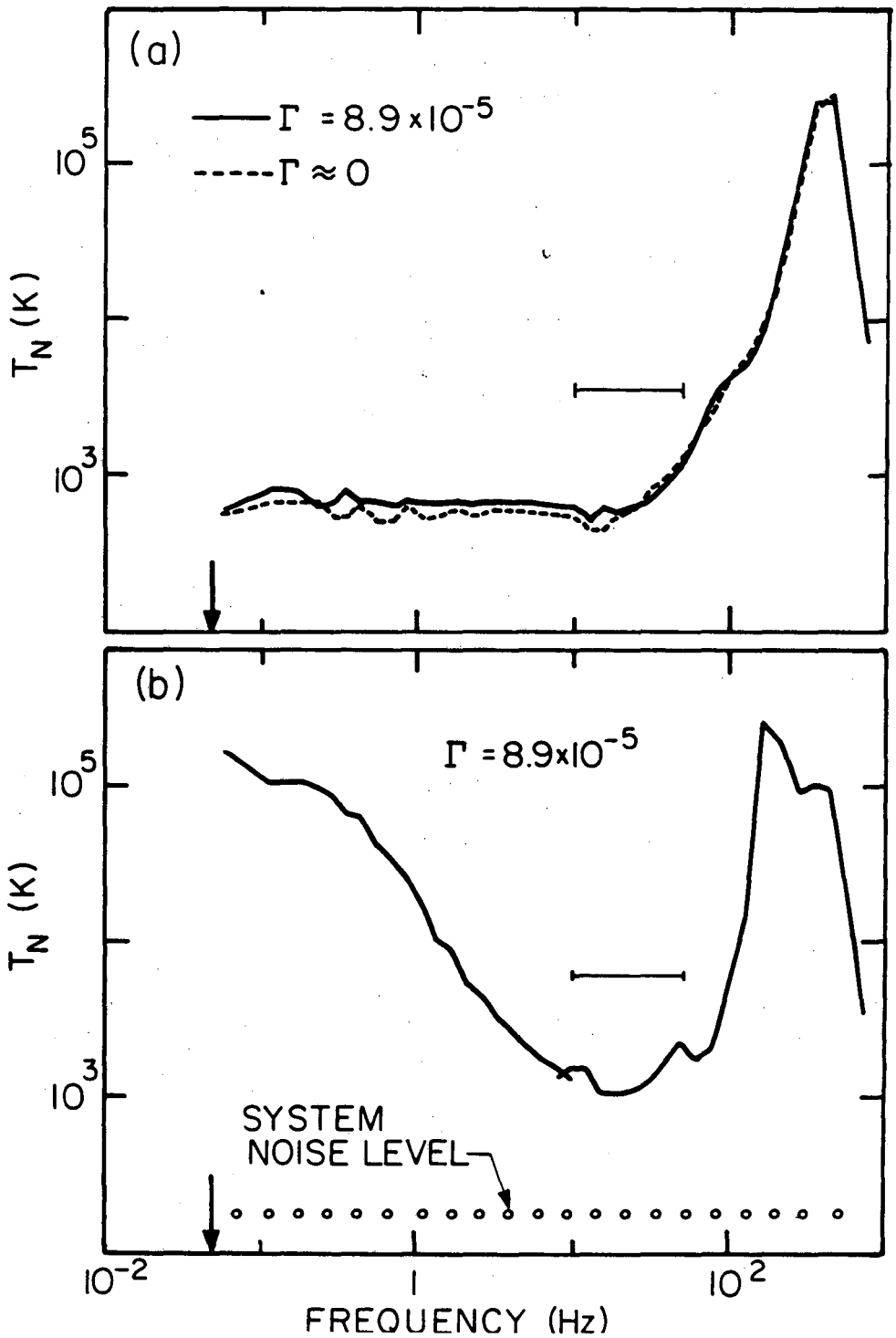

Figure 15. Analog voltage spectral density at points A (a) and B (b) of Fig. 13, with and without injected thermal noise. In (b), the junction noise was below the system noise in the absence of thermal noise. Arrows indicate frequency equivalent to 117 kHz in real junctions. Bandwidth over which noise measurements in Fig. 13 were made is indicated by bars.

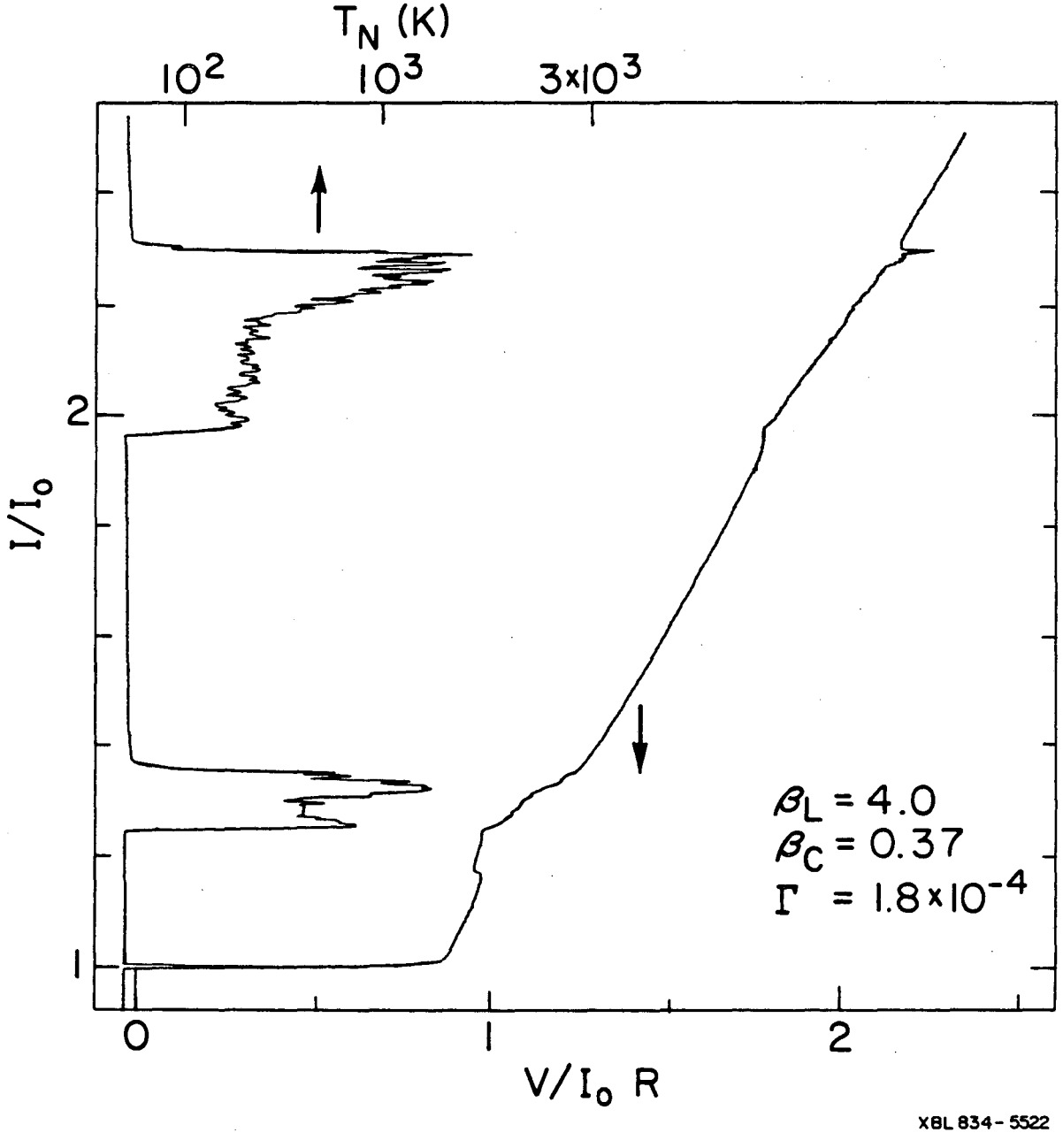

Figure 16. T_N and V/I_0R vs I/I_0 (for increasing I) for analog junction with $\beta_C = 0.37$, $\beta_L = 4.0$, and $\Gamma = 1.8\times10^{-4}$. Noise was measured at frequencies between 10 and 50 Hz.

analog simulator. The largest level of noise observed in actual junctions was 4×10^6 K (Fig. 5), while that seen in simulations was 2×10^5 K (Fig. 15). It is certain that there is a practical limit on the lowest frequency for which meaningful results can be obtained from analog simulations, below which the hopping process is destroyed or limited by other factors, such as the intrinsic 1/f noise of the electronic circuits and components comprising the analog. In the actual experiments, however, it is quite likely that this practical limit is much smaller in **dimensionless** units; the measurements described in Sec. F suggest that it is well below 3×10^{-7} (corresponding to 100 kHz). Finally, note that in the case of these small-area junctions, there is a better qualitative correspondence between the experiments and simulations, presumably due to the somewhat smaller value of β_L.

An extensive region of the (β_C,β_L)-parameter space has been mapped out using the analog simulator, with the results summarized in Fig. 17. Where several regions overlap in the figure, a distinction can be made between the different effects from the value of bias current for which those effects occur. For example, chaos could appear for one value of i, while relaxation oscillations may be more stable for another value. From this study we conclude that chaos arises for $1 \leq \beta_L \leq 25$ and for $\beta_C \leq 1$. The lower limit on β_C (0.01) arises from practical limitations of the analog: In principle, there is no apparent reason why it should not extend much lower. The region of bifurcated solutions naturally surrounds the region of chaos, and from this graph we see that the first period doubling sets in for $\beta_L \approx 0.7$ with $\beta_C = 0.1$. This is in excellent agreement with the analytic calculations described in the Appendix.

The other two types of phenomena shown, hysteretic (dual-valued for

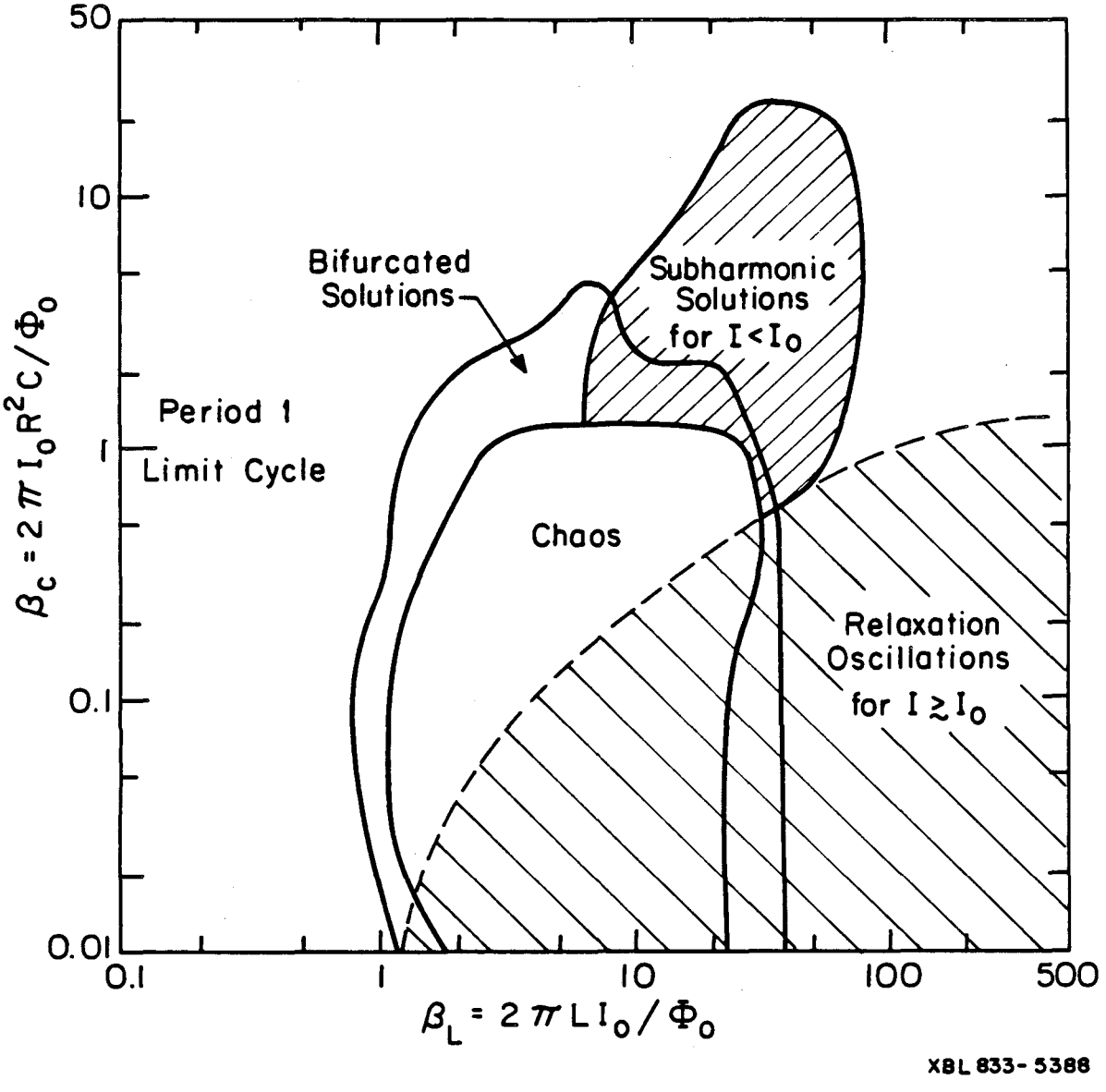

Figure 17. Detailed map of the behavior observable within the (β_C, β_L)-parameter space for the circuit of Fig. 1. The phenomena indicated occur for some value of the bias current: Overlapping regions of different effects occur for different values of bias current.

$I<I_0$) subharmonic solutions and relaxation oscillations, are distinct from chaos yet are intimately related to the complicated nonlinear dynamics of this system. Hysteretic solutions have for a long time been known to occur for $\beta_L = 0$ and $\beta_C \geq 1$. For $5 < \beta_L < 70$ subharmonic solutions are apparently allowed for $\beta_C > 1$. It is not clear why this is the case. As for the relaxation oscillations, all we can conclude at this point is that there **is** a connection between them and chaos, albeit a rather fuzzy one. (The boundary of the relaxation oscillation region in Fig. 17 is somewhat arbitrary.) "Dephased relaxation oscillations" (by which we mean aperiodic solutions which arise when the damping is not sufficient to weaken the plasma oscillations between relaxation cycles, resulting in a loss of phase stability) are perhaps a form of chaos. Further analytic and/or numerical work is needed to clarify this connection. Clearly, in the regime $\beta_L \geq 1$ when the period of the relaxation oscillations is very low, the familiar period doubling transitions to chaos are often observable, as in Fig. 12.

Another way to analyze a nonlinear system is to construct a stroboscopic picture of the dynamical flow within the multi-dimensional phase space. An example of this is the Poincaré map, or surface of section (Guckenheimer and Holmes, 1983). For the three-dimensional system described by Eq. (2.6), this could be constructed by graphing, say, $\ddot{\delta}(t)$ vs $\dot{\delta}(t)$ for fixed values of $\delta(t)$. Limit cycles would appear as discrete sets of points, a total of n for an nth-order subharmonic oscillation. Strange attractors, on the other hand, consist of a Cantor set of points, and thus would occupy an irregular and seemingly arbitrary curve. In the system of Fig. 1, the variables I_S and V are more readily accessible than δ or its derivatives, and so are more convenient to use

to construct mappings. The choice may seem more natural in the pendulum analog of Fig. 2, where the corresponding variables are $\dot{\phi}$ and $\dot{\theta}$. In terms of dimensionless variables, they are related to δ as follows:

$$i_S = i - \sin \delta - \beta_C \ddot{\delta} - i_{qp} \tag{2.14a}$$

and

$$v = \dot{\delta}. \tag{2.14b}$$

Figure 18 is an example of a Poincaré map of i_S vs v for the analog constructed from several thousand points sampled at $\delta = \pi$ for the parameter values $\beta_L = 2.25$, $\beta_C = 0.15$, $\Gamma = \Gamma_{sys}$, and $i = 3.85$. This bias point lies within a chaotic regime which is near an unstable period two limit cycle. The two darkened regions at the right are the "ghosts" of this unstable solution. The horn-shaped curve brings to mind the strange attractors found in other systems, such as the Lorenz equations. Note that in the vicinity of the lower-right darkened region that the attractor actually consists of several distinct layers, or "leaves." This feature is characteristic of self-similar structures, of which many strange attractors are examples.

Figures 19 and 20 are the Poincaré maps for the parameters of Fig. 13 (with $\Gamma = \Gamma_{sys}$), at point A and near point B, respectively. In each case the bias point lies within a chaotic regime, which accounts for the similarity of the two Poincaré mappings. (Recall that the spectra of Fig. 15 were obtained by adding external noise.) If the sytem were biased exactly at point B **with noise**, the resulting Poincaré mapping would be a composite of Fig. 20 and a stable period two limit cycle. Clearly, the structure seen in Figs. 19 and 20 is chaotic. Moreover, by comparing Figs. 18 and 19 one can conclude that larger β_L values lead to more complicated structure.

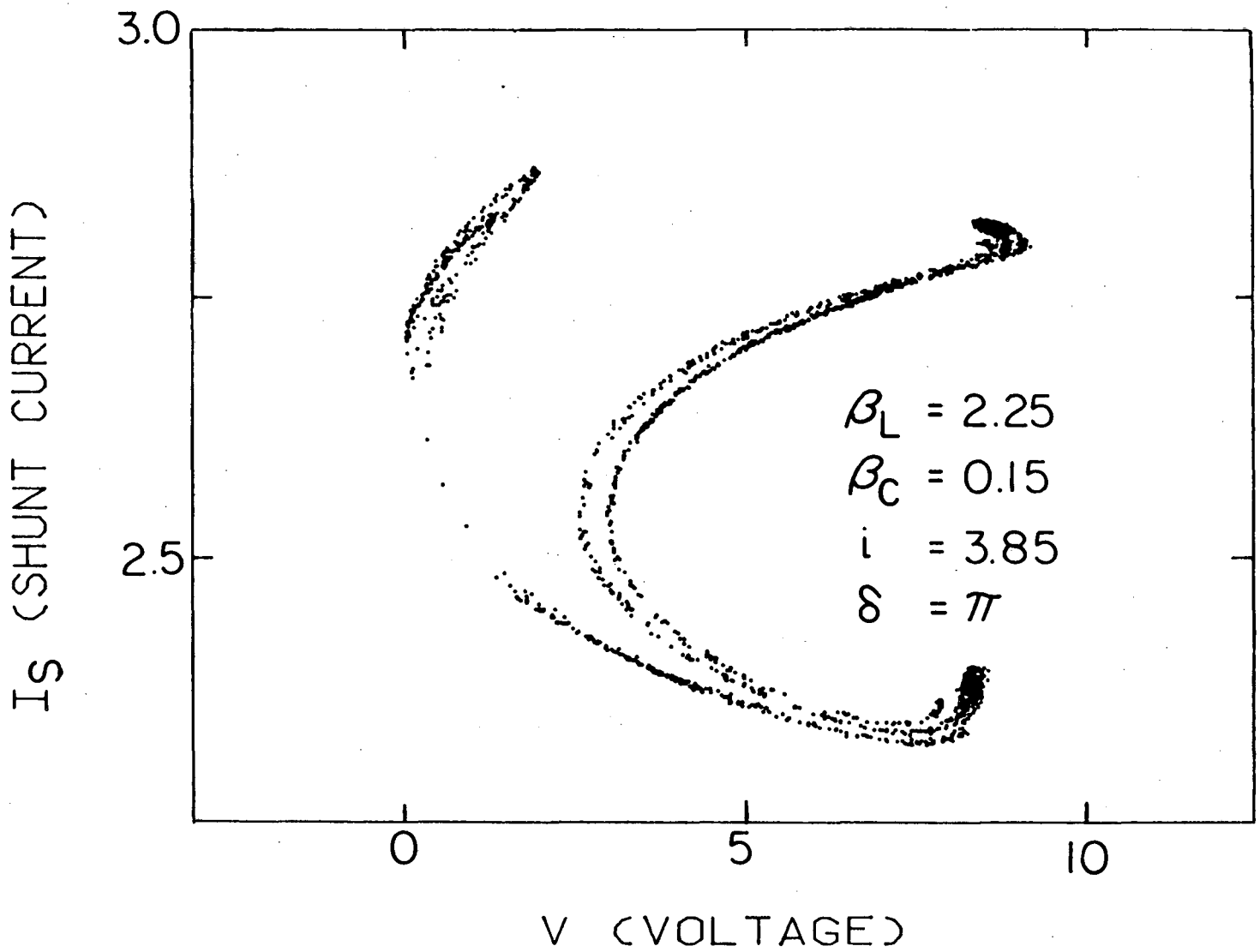

Figure 18. Poincaré map of the shunt current I_S vs voltage V for the analog at $\delta = \pi$, with $\beta_C = 0.15$, $\beta_L = 2.25$, $\Gamma = \Gamma_{sys}$, and $i = 3.85$.

XBL 842-6681

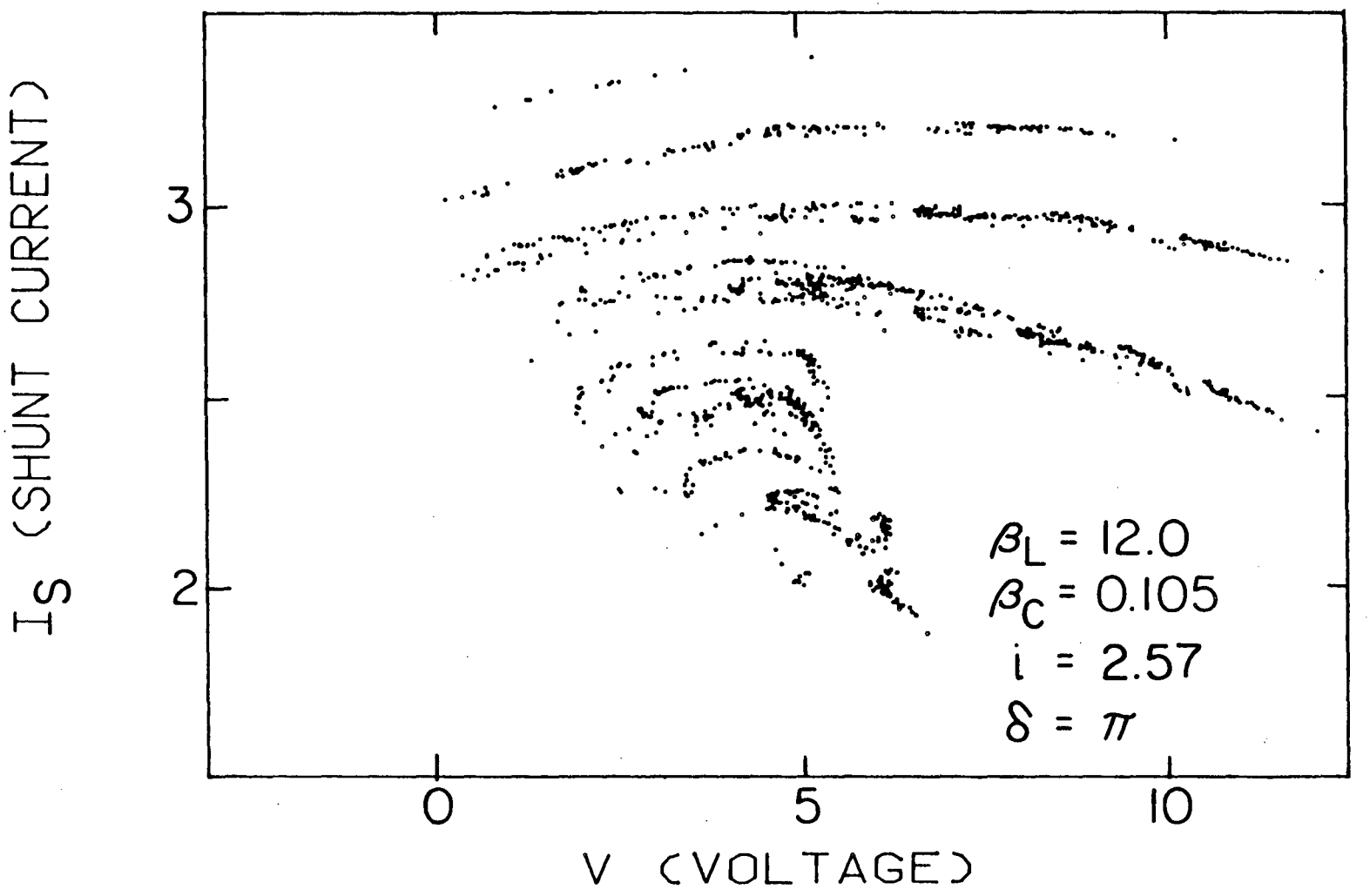

Figure 19. Poincaré map of the shunt current I_S vs voltage V for the analog at $\delta = \pi$, with $\beta_C = 0.105$, $\beta_L = 12.0$, $\Gamma = \Gamma_{sys}$, and $i = 2.57$ (point A of Fig. 13).

XBL 842-6682

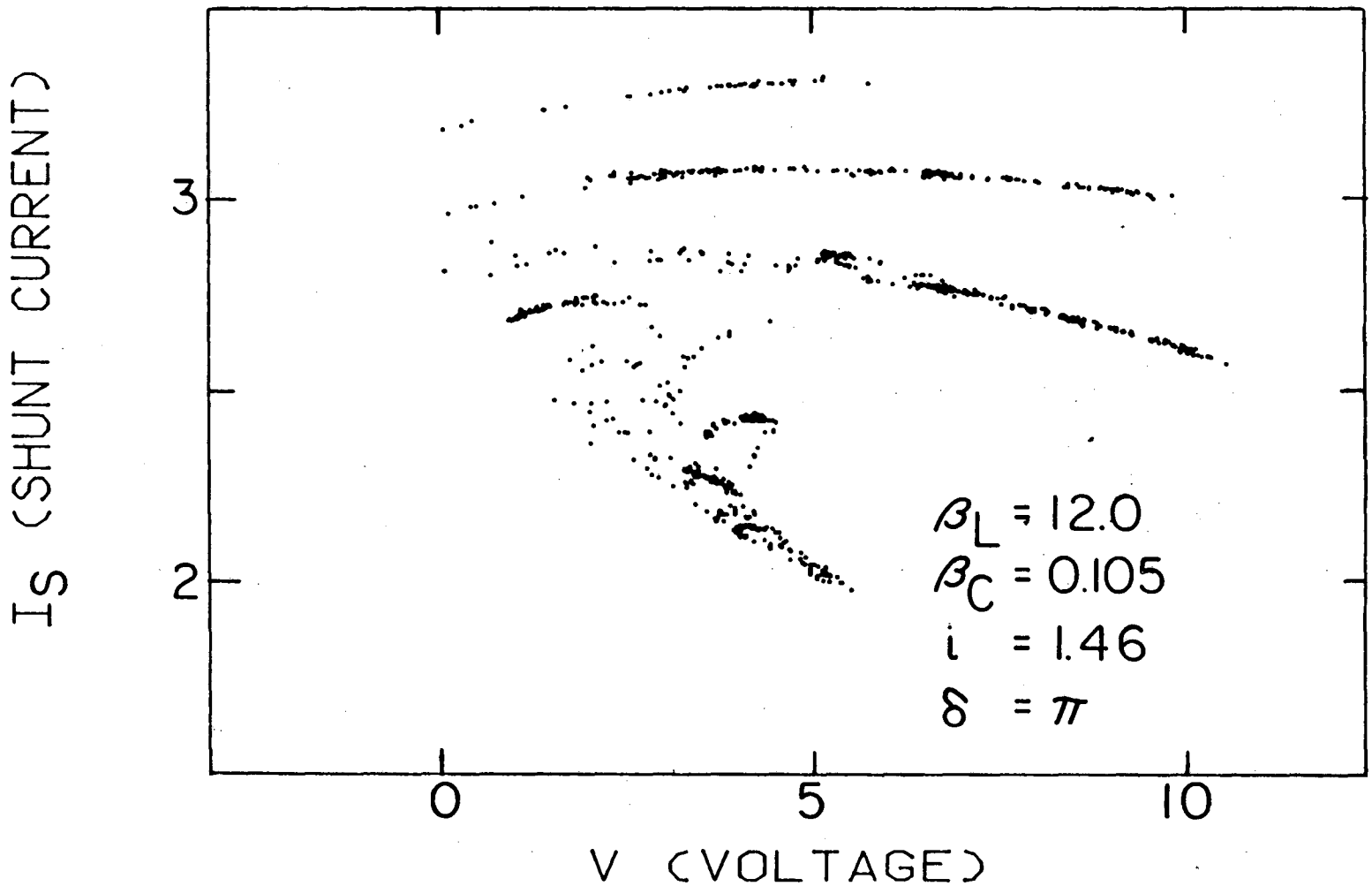

Figure 20. Poincaré map of the shunt current I_S vs voltage V for the analog at $\delta = \pi$, with $\beta_C = 0.105$, $\beta_L = 12.0$, $\Gamma = \Gamma_{sys}$, and $i = 1.46$ (near point B of Fig. 13).

XBL842-6683

F. Noise Spectra

An interesting related question is: What is the dependence on frequency of the spectrum of the hopping noise at low frequencies? Several theories have been proposed recently which address the origin of excess low-frequency noise in nonlinear dynamical systems (Manneville, 1980; Ben-Jacob et al., 1982; Geisel and Nierwetberg, 1984). All of these theories predict the shape of the power spectrum at low frequencies. However, considering the simplicity of the models used, it is not clear how such results can be applied to real physical systems, such as the one studied here. Therefore, in order to test the relevance of these models to the system of Fig. 1, we have measured directly the low-frequency hopping noise spectrum in an actual junction.

We used a small-area junction [Fig. 3(a)] because its impedance is better matched to the preamplifier. Figure 21 shows an I-V characteristic of a small-area junction with a resistance of 0.48 Ω and critical current of 190 μA, at 4.2 K.

The excess low-frequency noise was greatest for bias points near the large NDR at 310 μA of Fig. 21, so careful measurements were made there. The noise levels at frequencies below 100 kHz were large enough so that extra tank circuits were used only to obtain the data points at 98 kHz and 780 kHz. Figure 22 is a graph of the noise power spectra, expressed as a noise temperature, which is defined as:

$$T_N(f) = S_V(f)/4k_BR. \qquad (2.15)$$

$S_V(f)$ is the voltage spectral density read from the HP 3585A spectrum analyzer, which followed the preamplifier. The several curves are data taken for different values of bias current. Notice that all of the curves have a characteristic shape: a plateau at asymptotically low

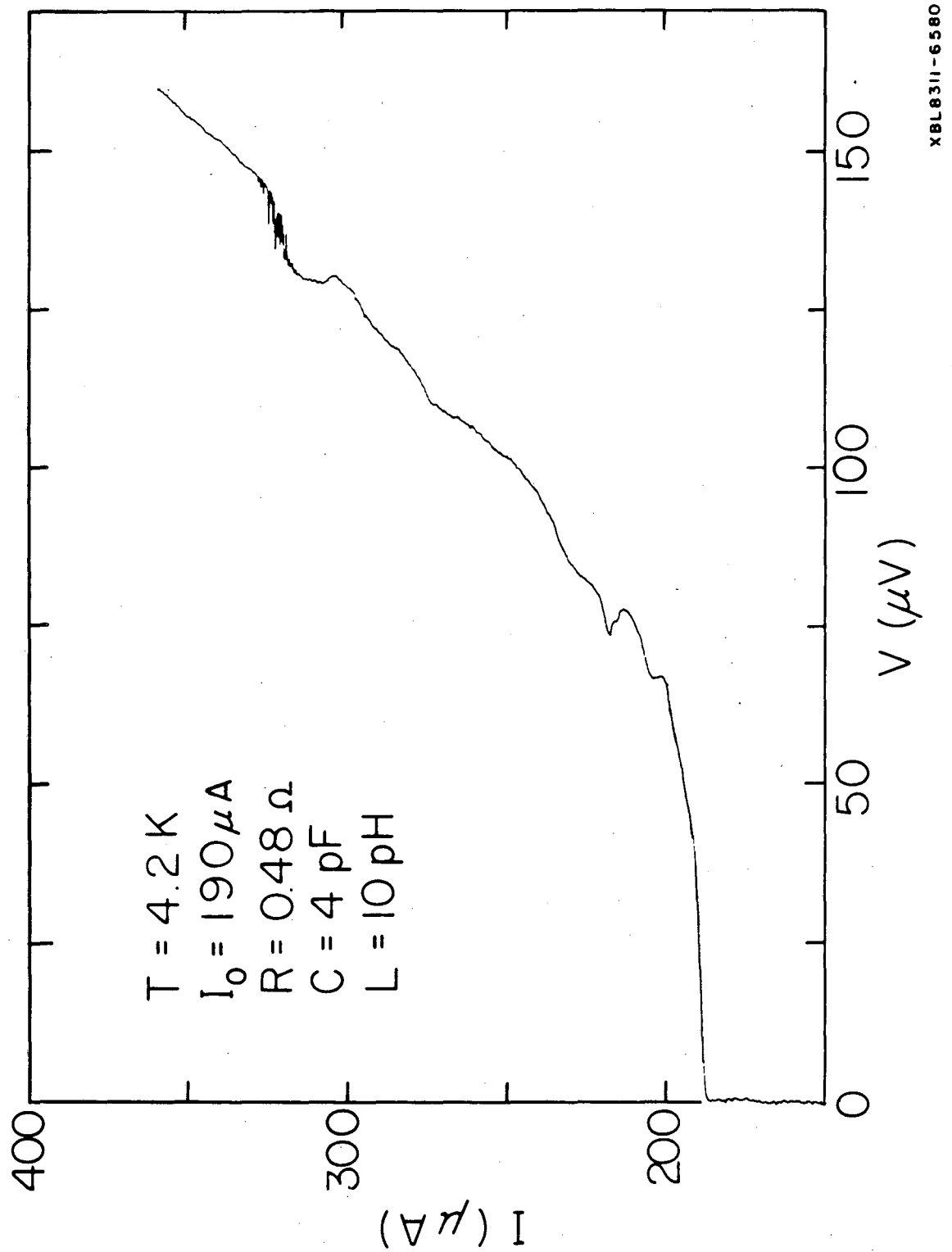

Figure 21. I-V characteristic of the same junction as for Fig. 9, at 4.2 K with I_0 = 190 μA and R = 0.48 Ω. This junction was used in subsequent measurements of the low-frequency noise spectrum.

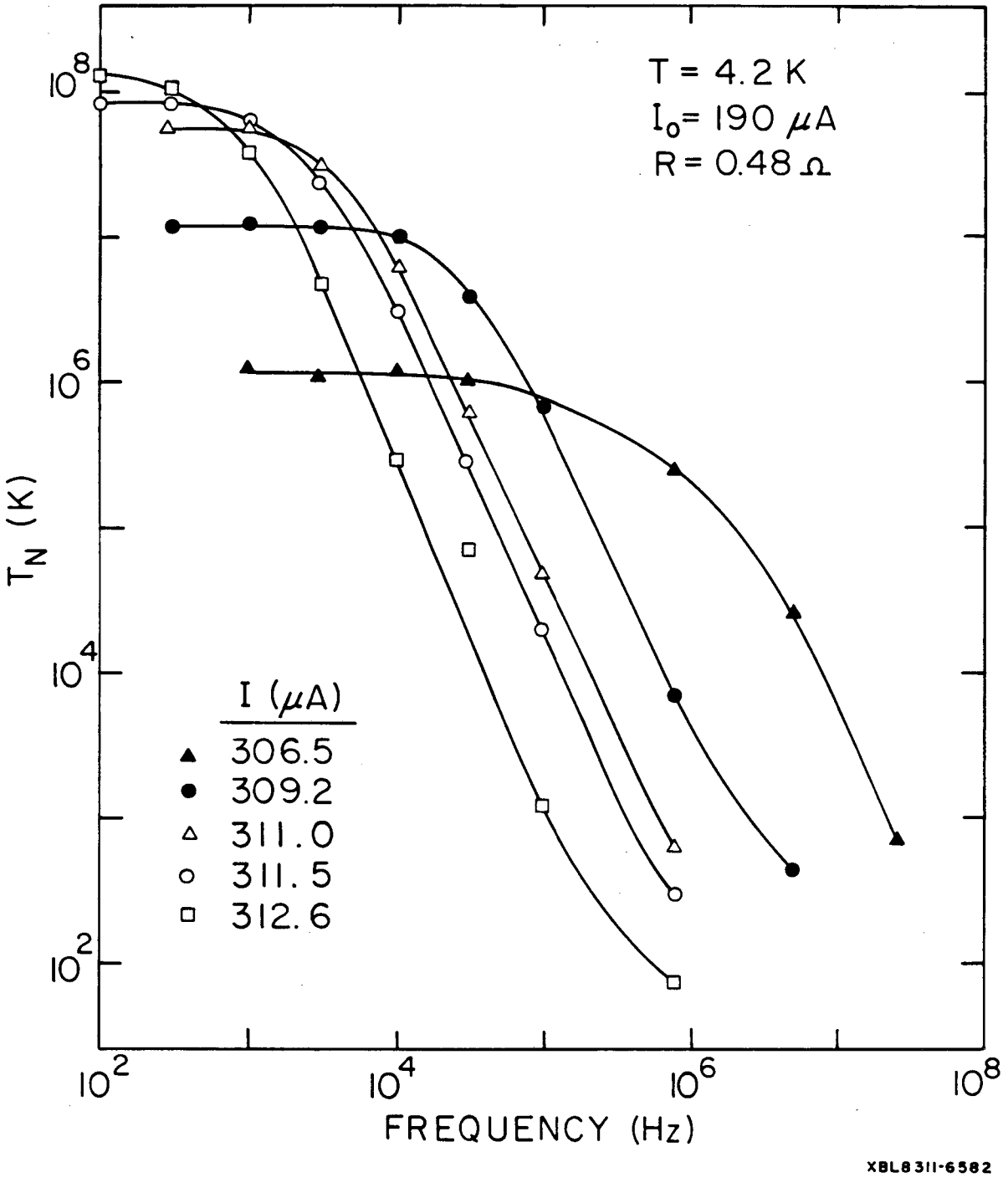

Figure 22. T_N vs frequency for the junction of Fig. 21. The several curves are data taken at different values of the bias current.

frequencies, and an approximate $1/f^2$ fall-off at higher frequencies. A least-squares fit of the points on the linear portion of the curve for I = 3.110 μA gives $S_V \sim 1/f^{2.1}$.

The same junction was also measured at the lower temperature of 2.6 K, and the results are plotted in Fig. 23. Although the critical current and resistance both increased somewhat as the temperature was lowered, to values of 196 μA and 0.50 Ω, respectively, the same basic results were obtained: The measured power spectra went as $1/f^2$, with plateaus at zero frequency.

Two basic questions come up in attempting to interpret these data. First, is this a noise-induced or deterministic hopping process? Unfortunately, the results presented here cannot answer that question. On the one hand, it is well known that Poisson switching between two states, characterized only by a constant average switching rate, generates a $1/f^2$ spectrum. Thermally activated processes can sometimes fall into this category. On the other hand, for dynamical systems such as this one, in which the effective potential barrier separating the two states is very sensitive to the value of the parameters, measurements of the temperature dependence of the noise spectra may not isolate the source of the hopping. We are unable to conclude which of the parameters changing with temperature (critical current, resistance, Johnson noise, etc.) is the variable controlling the response. Secondly, if the the spectrum is $1/f^2$, what sort of theoretical explanation can best account for our results? The theories of both Ben-Jacob et al. (1982), and Geisel and Nierwetberg (1984) both predict $1/f^2$ shapes, starting from different models: Which (if either) is correct? In short, merely measuring the power spectrum of a hopping process does **not** necessarily

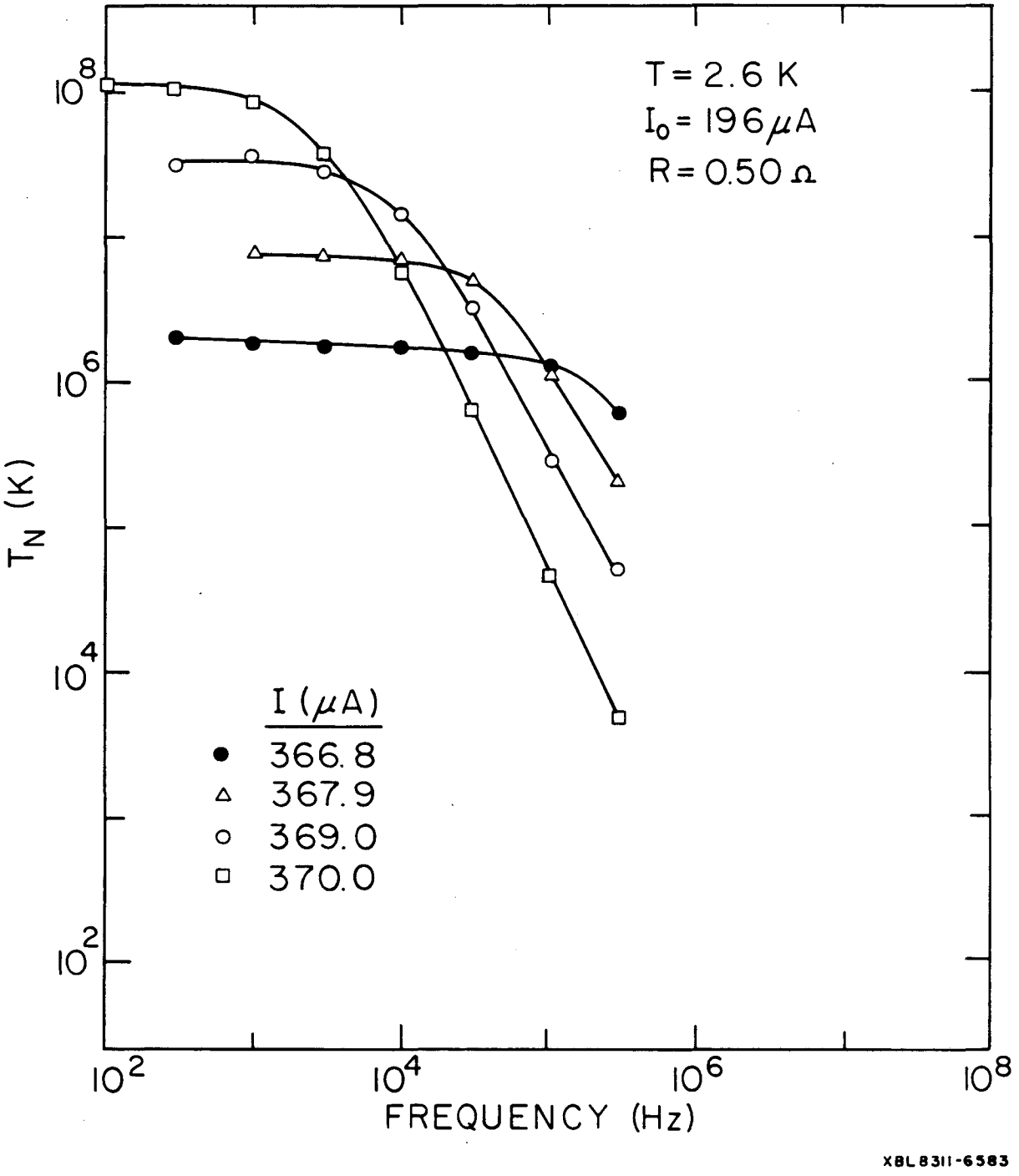

Figure 23. T_N vs frequency for the junction of Fig. 21, at 2.6 K. The junction critical current and shunt resistance were 196 μA and 0.50 Ω, respectively, at this temperature. The several curves are data taken at different values of the bias current.

provide sufficient information to be able to distinguish between competing theories.

G. Negative Resistance Amplifier

A negative differential resistance (NDR) is potentially a very useful feature for achieving amplification of oscillatory signals. For example, by placing a circuit element possessing a NDR into a series resonant circuit and biasing it appropriately, the circuit will oscillate spontaneously at the resonance frequency, thus achieving "infinite gain." More generally, the ability to compensate for other circuit losses can have beneficial applications. As has been discussed above, self-resonant Josephson junctions exhibit stable NDR's, so it would be interesting to explore the amplification properties of devices. This section describes experiments to do just this.

Figure 24 shows the I-V characteristic of a small-area junction. Its rather large NDR at a bias of roughly 170 μA makes it suitable for amplifier measurements. An amplifier was formed by connecting the junction in parallel with two tank circuits, whose resonant frequencies were 98 kHz and 780 kHz. Figure 25 shows an equivalent circuit of the amplifier configuration for one of the tank circuits. The series resistance R_T (about 1 Ω) was added to maintain the total circuit resistance, including the junction dynamic resistance when biased on the NDR, positive. Otherwise, gain measurements would not be meaningful. A weak signal near the tank circuit resonant frequency f_0 was injected into the tank circuit by sinusoidally driving a coil formed by several turns of wire wound around the cryostat containing the junction. The voltage V_T across the capacitor was measured by a low-noise preamplifier followed by a Hewlett-Packard 3585A Spectrum Analyzer. The power gain is defined

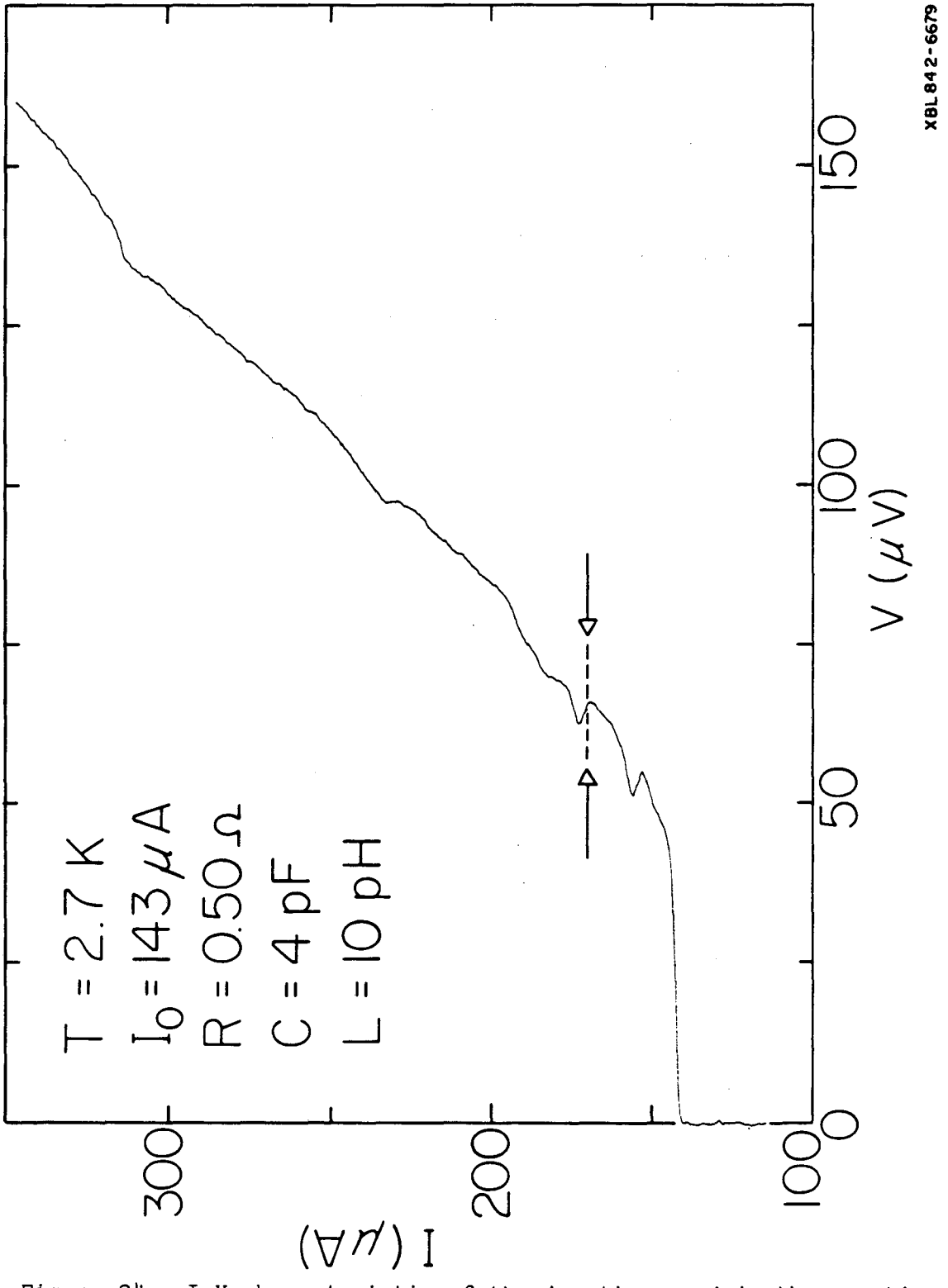

Figure 24. I-V characteristic of the junction used in the negative resistance amplification experiments. Arrows indicate the bias point where the measurements were made.

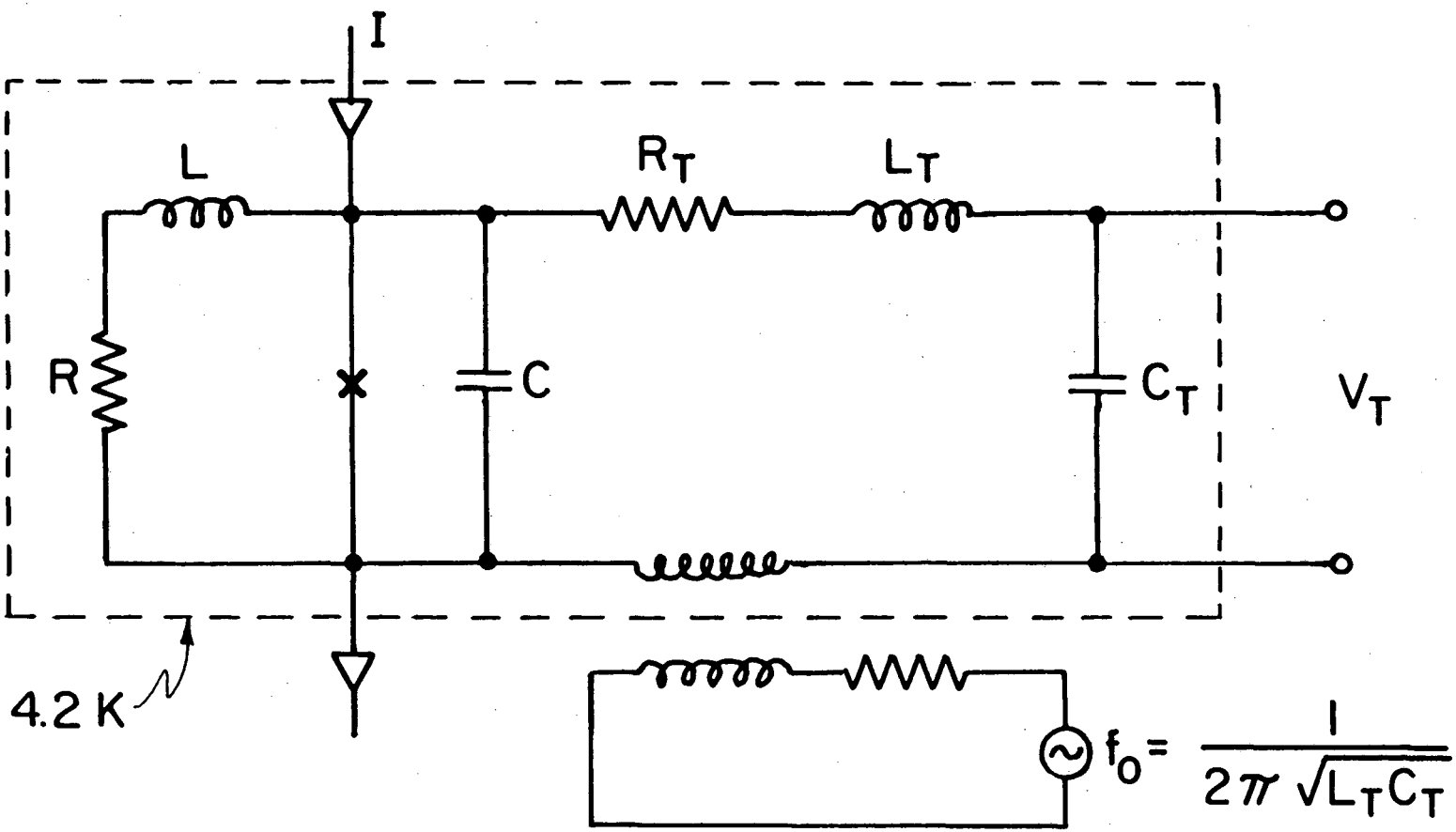

Figure 25. Circuit diagram of the experiment to measure low-frequency negative resistance amplification in the junction of Fig. 24. The precise magnitude of the inductive coupling between the input signal and the tank circuit was unknown.

XBL842-6676

for this circuit as:

$$G = \left(\frac{R_T}{R_T + R_D}\right)^2. \qquad (2.16)$$

where $R_D = dV/dI$ at $I = I_B$ for the bias current I_B in the NDR, indicated by the arrows in Fig. 24.

Figures 26 and 27 show the power spectra of the voltage V_T for bias currents $I = 0$ (bottom curve in each figure) and $I = I_B$ (top curve), at 98 kHz and 780 KHz, respectively. In Fig. 26, although the peak of the input signal is obscured by the top curve, there was, as indicated, a gain of 5.7 dB when the junction was biased on the NDR, a number in agreement with what one would expect from estimates of R_T and R_D. Notice, however, that the noise in the vicinity of f_0 has been amplified much more, by roughly 30 dB. Similarly, in Fig. 27, the signal gain was measured to be 1.2 dB, while the noise gain was about 20 dB. The fact that the gain is lower at the higher frequency suggests that the differential resistance is a function of frequency, being somewhat less negative at 780 kHz. This is entirely plausible, considering that the I-V characteristic is an average of oscillations of much higher frequencies. Obviously, for high enough frequencies, this quasi-static I-V approximation ceases to be valid.

The most important conclusion to be drawn from these results is that a type of "noise rise" ensues when the NDR is utilized in a low-frequency amplifier. By this we mean that the amplification of narrow-band signals does not increase as fast as that for nearby broad-band noise, as some parameter is varied. We speak of a "noise rise" here in the

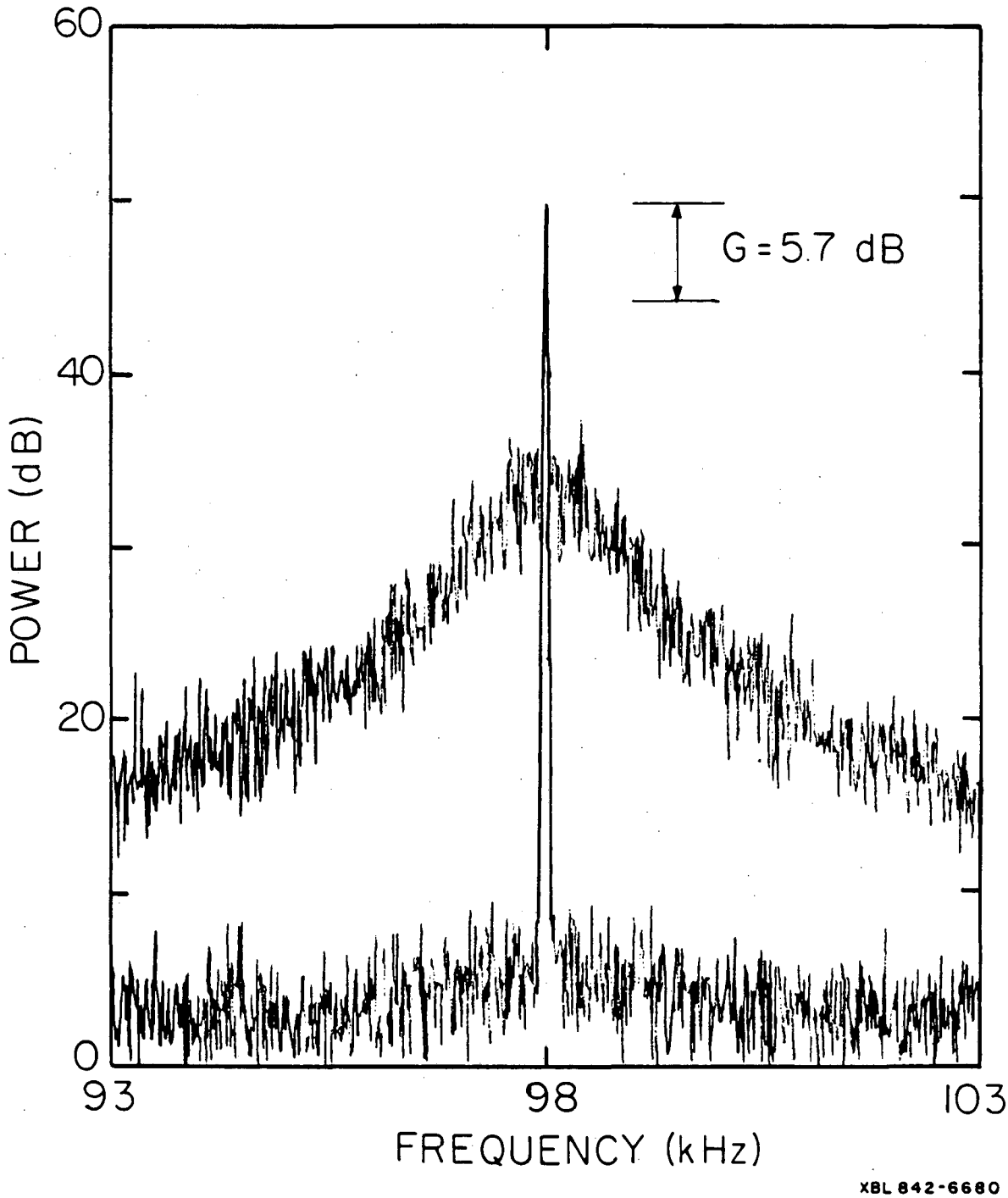

Figure 26. Power spectrum near 98 kHz ($=1/2\pi\sqrt{L_T C_T}$) of both the input signal (lower curve) and the output response (upper curve) of the negative resistance amplifier. A gain of 5.7 dB was achieved.

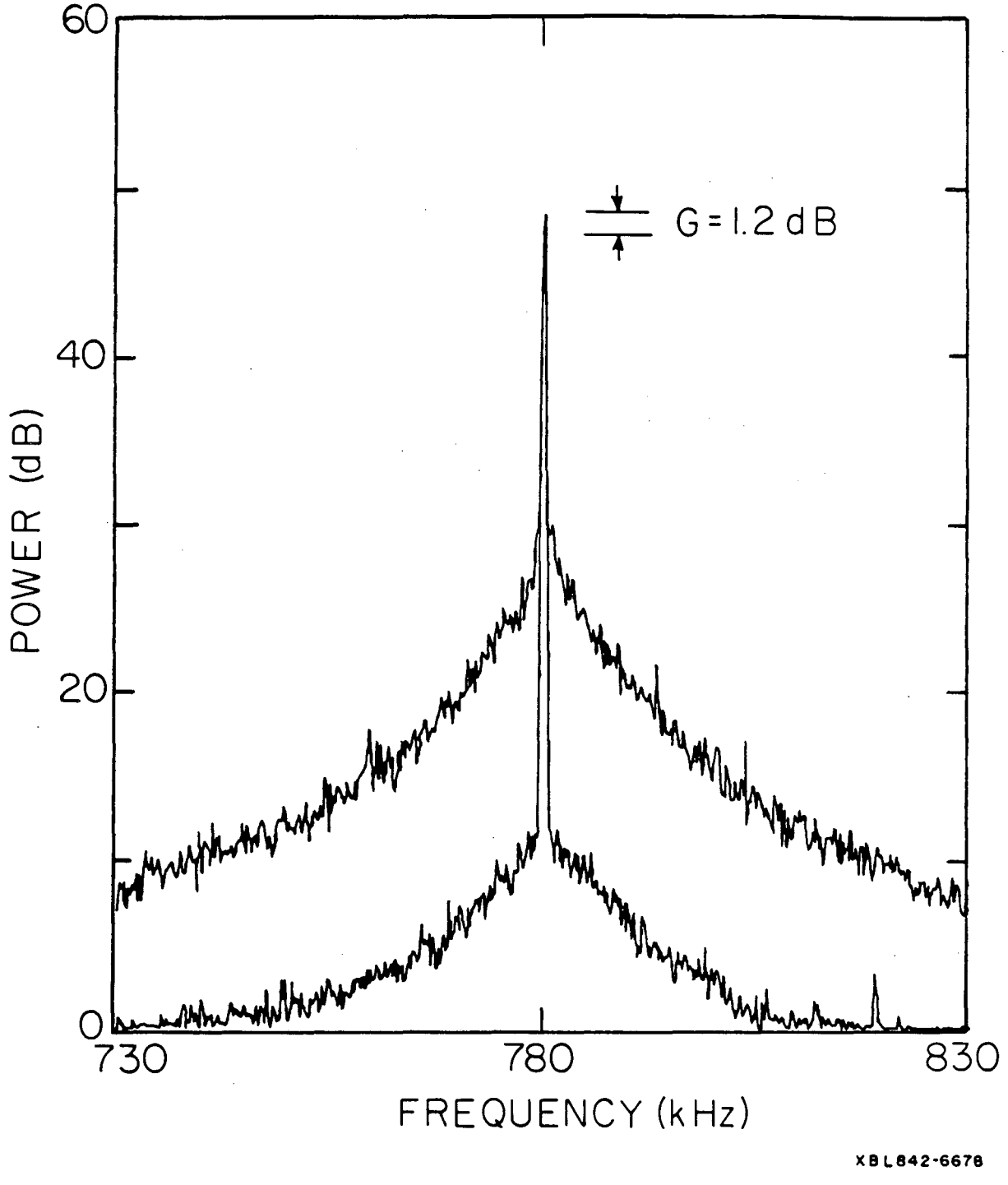

Figure 27. Power spectrum near 780 kHz ($=1/2\pi\sqrt{L_T C_T}$) of both the input signal (lower curve) and the output response (upper curve) of the negative resistance amplifier. A gain of 1.2 dB was achieved.

same sense as for Josephson parametric amplifiers (Feldman, Parrish, and Chiao, 1975), which are discussed in more detail in Chapter IV. We should point out that it is unlikely that the noise rise can be explained by a saturation of the input signal, considering the good agreement between the measured and estimated gains at 98 kHz.

In order to explain these results a model is needed of the underlying dynamics. On the basis of analog simulations of this system, we suggest the following picture. Imagine that at some value of the bias current there is a bifurcation of the junction system to a substantively different solution. Assume furthermore that the solutions on either side of this bifurcation point are characterized by different mean voltages: There is a discontinuity in the I-V characteristic as the bias current is varied. Now include thermal noise. The system now samples alternately, or hops between, the two solutions, resulting in a rounding of the abrupt discontinuity in the I-V characteristic. This hopping process, as has been discussed at length above, would generate excessive low-frequency noise when it is triggered by even a small anount of broad-band noise. Thus, although one achieves gain at the signal frequency due to the NDR, there is a great amount of broad-band noise present in the vicinity of the signal frequency due to the hopping process--hence, a noise gain. Furthermore, the fact that the gain of the amplifier decreases as the operating frequency is increased (compare Figs. 26 and 27) is consistent with this interpretation of the origin of the NDR's: One would expect less signal coherence at higher frequencies.

In conclusion, we have examined the usefulness of NDR's in self-resonant Josephson tunnel junctions as low-frequency amplifiers. Their performance is not very satisfactory from a practical perspective: They

exhibit a noise rise. On the positive side, the interpretation of this noise rise in terms of the underlying noise-induced hopping dynamics underlines the relevance of these effects in general to nonlinear systems.

H. Concluding Remarks

We conclude this chapter by supplying answers to the questions posed in Chapter I. First, chaos **is** observable in this Josephson junction system; it manifests itself as a noise temperature $T_N \sim 10^3$ K. Furthermore, we know from simulations that both the Feigenbaum and Pomeau-Manneville transitions to chaos are possible in this system. Although no new "paths to turbulence" were uncovered in the course of these studies, a new phenomenon of noise-induced switching, or hopping, was observed experimentally, with $T_N \sim 10^5$ K at low frequencies. This process seems to be correlated with the appearance of negative differential resistance regions in the I-V characteristics. In summary, we have succeeded in understanding most of the key results of these experiments by means of analog simulations of the lumped circuit equations, reaffirming once again our faith in the RSJ model.

One question remains unanswered though: Why should the switching noise discussed in Sec. F possess a $1/f^2$ spectrum, down to such extremely low frequencies? Such a result is very difficult to simulate, even using analog methods. Perhaps the only way to understand this result would be to reduce the governing differential equation to a nonlinear mapping, and then study the behavior as one iterates it.

CHAPTER III

DETERMINISTIC HOPPING IN A JOSEPHSON CIRCUIT DESCRIBED BY A ONE-DIMENSIONAL MAPPING

A. Introduction

"Hopping", the seemingly random transition of a dynamical variable among several distinct states, is a phenomenon found in a variety of nonlinear physical systems, including optical devices (Gibbs et al., 1981), semiconductor devices (Teitsworth, Westervelt, and Haller, 1983), and Josephson junctions (Ben-Jacob et al., 1982; Goldhirsch et al., 1984). For many of the same reasons that chaos in systems with only a few degrees of freedom has been used as a paradigm of chaos in more complicated systems, it is worthwhile to study hopping in simple systems. A number of questions present themselves immediately: Can hopping be a deterministic process? If so, what relationship does hopping have to chaos? What is the effect of external noise? What is the power spectrum of the low-frequency noise produced by the hopping process? Can one go from a phenomenological characterization of hopping to the mechanism producing it?

Some of these questions have already been clarified in a limiting case where the system hops back and forth between a noise-free state and a noisy state. This occurrence of noise in bursts, called intermittency, has been known for quite some time in hydrodynamical systems (Tritton, 1977). More recently, Mandelbrot (1977), studying the noise in transmission lines, realized the importance of a phenomenological property displayed by this kind of noise, namely self-similarity. The noise he was studying could be modeled by a signal consisting of noisy bursts of equal duration separated by intervals of random length u whose

probability distribution obeyed the equation

$$\text{Probability}(u > t) = t^{-D},$$

where D is a constant. The pattern in time formed by the noise-free phases is invariant respect to the choice of time scale and was an early example of a fractal, i.e. an object lacking any characteristic scale. D is known as the fractal dimension.

Manneville (1980) showed that noise with this scaling property could be produced by a deterministic mechanism involving the iteration of a one-dimensional mapping with a marginally unstable fixed point. The analytical behavior of the map near its fixed point provides the basis for self-similarity. Manneville studied the particular case of the map $X_{n+1} = X_n(1 + \varepsilon + X_n) \bmod 1$ that appears as a special case of the destabilization of a limit cycle of a dissipative dynamical system. He found numerically that iterates of this mapping produce a signal with a power spectrum behaving as $1/\omega|\ln \omega|^2$ (ω is the frequency in rad/s), and justified this result with a scaling argument. Procaccia and Schuster (1983) generalized Manneville's results to a more general class of mappings and obtained expressions for the frequency dependence of the power spectrum in terms of the parameters of the mapping.

The particular mapping studied by Manneville belongs to an important class of intermittent phenomena known as the Pomeau-Manneville (1980) intermittency. This type of intermittency, which is generic, occurs when a dissipative system has a limit cycle that loses stability to a chaotic attractor. Pomeau and Manneville have distinguished three subclasses for this kind of intermittency according to the way in which the complex number known as the Floquet Multiplier (FM) leaves the unit circle, signalling that the limit cycle has lost stability. In type I

intermittency the FM is real and crosses the unit circle at +1. This is called a tangent bifurcation for a one-dimensional mapping. In this case, there is an upper limit to the distribution of times in the noise-free or laminar phase. For type III intermittency, the FM is real and negative and crosses the unit circle at -1, signalling a period-doubling bifurcation to an unstable mode. In this case there is no long time cut-off. Type II intermittency is similar in that respect to type III and occurs when the FM is an arbitrary complex number crossing the unit circle at a phase different from 0 or π. Type II and type III intermittencies thus produce excess noise at low frequencies, and at the onset of intermittency the power spectrum scales as $1/\omega|\ell n\ \omega|^2$ for type II (this case corresponds to the Manneville map given above) and as $\omega^{-1/2}$ for type III. Type I and type III intermittencies have been shown to occur in several physical systems (Manneville and Pomeau, 1979, 1980; Berge et al., 1980; Dubois, Rubio, and Berge, 1983).

It is thus tempting to explain the excess low frequency, or "1/f" (where $f = \omega/2\pi$), noise found in many complex systems (Dutta and Horn, 1981) by this Pomeau-Manneville intermittency. Manneville (1980) has suggested that type II intermittency might be a universal explanation. However, it is not clear that these systems can be reduced to an equivlent dissipative dynamical system with only a few degrees of freedom. Moreover, as was shown by Manneville (1980), and Procaccia and Schuster (1983), the spectrum behaves as $\omega^{-\nu}$ (ν a constant) down to arbitrarily low frequencies only for very precisely adjusted values of the parameters, and it is unclear at the present how these values could be obtained in a wide variety of many-body systems under a broad range of circumstances.

On the other hand, assuming one is indeed dealing with a system possessing few degrees of freedom, the Pomeau-Manneville mechanism, although "generic" (used in the mathematical sense meaning "most likely scenario"), is not the only one which can produce low-frequency noise, or involve the reduction of a differential equation to a one-dimensional mapping. More complicated situations can occur, as for example in an electronic circuit (Arecchi and Lisi, 1982; Beasley, D'Humieres, and Huberman, 1983; Voss, 1983) or in the Rikitake dynamo (Ito, 1980). Both of these systems exhibit hopping between two equivalent states deduced from one another by a symmetry operation.

An example of a physical system in which various kinds of hopping processes are known to occur is the Josephson junction. In particular, hopping between metastable states in the ac-driven junction, Eq. (1.1), has been observed in simulations (Ben-Jacob et al., 1982; D'Humieres et al., 1982; Goldhirsch et al., 1984) and also recently experimentally (Octavio and Readi Nasser, 1984). Ben-Jacob et al. (1982) analyzed Eq. (1.1) for parameter values for which there is hopping between two unstable phase-locked states. Their analytical calculation of a simplified model of Eq. (1.1) produces power spectra that decay as $1/f^2$ or $1/f^4$ (depending on parameter values) at relatively high frequencies. Their numerical computations are in good agreement with their analysis. In a similar vein, Geisel and Nierwetberg (1984) have also analyzed Eq. (1.1), together with a related one-dimensional mapping, and have found a $1/f^2$ dependence above some characteristic frequency. In neither of these works is the possibility of 1/f noise addressed. Very recently, Gwinn and Westervelt (1984) presented numerical simulations of Eq. (1.1) showing 1/f noise over a limited range, but found that this noise is

easily destroyed by a small amount of computational noise.

We have chosen to study an alternative system, that shown in Fig. 1 and discussed in great detail in Chapter II. The relationship between that noise-induced hopping process, identified as the source of the observed excess low-frequency noise, and the deterministic nonlinear dynamics was not addressed at the time. We merely pointed out that when the added white noise was reduced to a very low level in the simulations, the hopping process ceased, and the excess (1/f-like) noise spectrum vanished. However, in the course of related simulations, a relatively rare situation was observed in which a low-frequency 1/f power spectrum (over a limited range) was produced by hopping that arose in the **absence** of thermal noise. This process, which we refer to as **deterministic hopping**, occurred only at very precisely chosen values of the bias current, and was **destroyed** by the application of a modest level of Nyquist noise.

The aim of this Chapter (Miracky, Devoret, and Clarke, 1984) is to demonstrate that the underlying dynamics leading to this deterministic hopping process can be represented by a one-dimensional mapping of one of the dynamical variables of the junction (the voltage). In particular, we establish a connection between a mapping which, in Sec. B, we show analytically to lead to 1/f noise under appropriate conditions, and the differential equation for the Josephson junction circuit of Fig. 1, which we summarize in Sec. C. The results of the analog and digital simulations that exhibit the excess low-frequency noise (over a limited range) and the one-dimensional map are presented in Sec. D. Section E contains a concluding summary.

B. Deterministic Model Producing Switching Noise With a $\omega^{-\nu}$ Spectral Density

In this section we describe a calculation carried out by M.H. Devoret (Miracky, Devoret, and Clarke, 1984) of the spectral density of a simple two-state switching process as a function of the probability distribution of the time intervals between switching events. We obtain sufficient conditions for the observation of a $\omega^{-\nu}$ power spectrum and describe a mathematical deterministic model based on the iteration of a one-dimensional mapping that satisfies these criteria.

1. Simple Model For Switching Noise

We consider a physical process in which a variable switches between two states of the system as indicated in Fig. 28(a). Each state represents some dynamical process, for example, a limit cycle, a relaxation oscillation or a chaotic regime. We assume that the characteristic frequencies of these dynamical processes are much higher than typical switching frequencies between the two states, so that each state may be represented by a time-averaged value as shown in Fig. 28(b). Thus, we need consider only a signal $x(t)$ that takes the values 0 and 1 during successive random intervals τ_0 and τ_1. We assume that all the intervals are statistically independent of one another. The random process is thus described entirely by the probability distributions

$$\pi_0(t) = \text{probability} \quad (\tau_0 > t) \tag{3.1a}$$

$$\pi_1(t) = \text{probability} \quad (\tau_1 > t). \tag{3.1b}$$

The interesting property of our model, as we shall see, is that the spectral density $S_x(\omega)$ of the process $x(t)$ can be calculated in closed form in terms of $\pi_0(t)$ and $\pi_1(t)$. When $\pi_0 = \pi_1$, the process is completely described by its power spectrum (as is the case, for example,

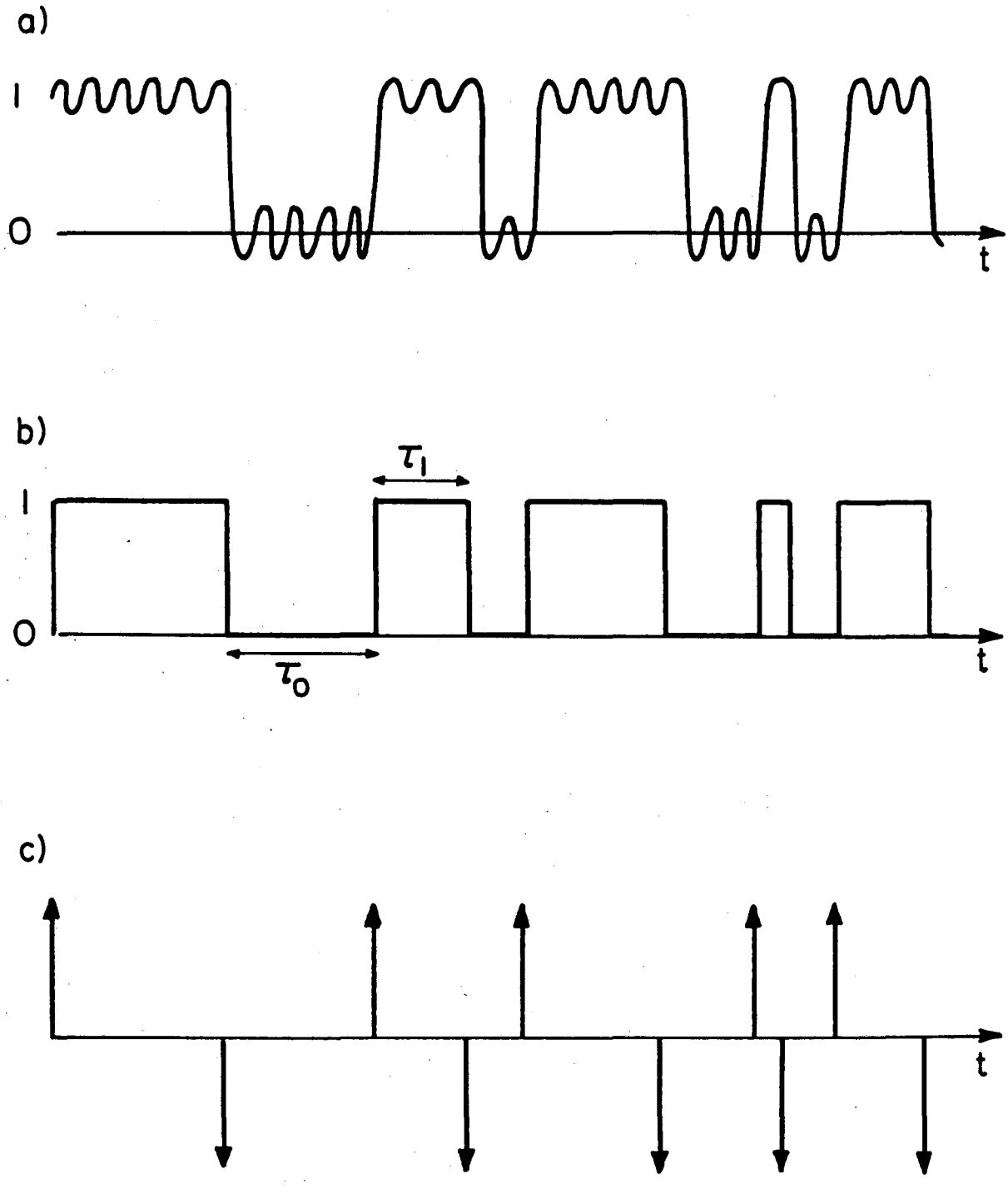

XBL846-7021

Figure 28. (a) Time sequence of a signal showing switching between two distinct oscillatory modes; (b) time sequence obtained from (a) by retaining only the zero-frequency component of each mode; (c) derivative of the time sequence in (b): The arrows represent delta functions.

for Gaussian noise).

2. Calculation of Spectral Density

Our procedure is to compute the correlation function G(t) of the time derivative $y(t) = dx(t)/dt$, and to Fourier transform this correlation function to obtain the spectral density $S_y(\omega)$. We then use the result

$$S_x(\omega) = S_y(\omega)/\omega^2. \tag{3.2}$$

We chose this method because the calculation of the correlation function of y(t), which consists of delta functions of alternating sign [Fig. 28(c)], is particularly simple.

It can easily be shown that

$$G(t) = \langle y(0)y(t)\rangle = \langle|y(0)|\rangle\{\delta(t) + \frac{1}{2}[\langle y(t)\rangle_+ - \langle y(t)\rangle_-]\}$$

$$= [2/(\langle\tau_0\rangle + \langle\tau_1\rangle)]g(t), \tag{3.3}$$

where, assuming y(t) is stationary, $\langle y(t)\rangle_\pm$ is the ensemble average value of y(t) at time t when there is a spike of sign $\pm$ at t = 0. The quantity $\langle|y(0)|\rangle$ is simply the average rate of spikes at t = 0. If necessary, stationarity can be imposed by introducing a cut-off at long times in $\pi_0(t)$ and $\pi_1(t)$.

We define the probability densities $p_0(t - t')$ and $p_1(t - t')$ of finding a positive and negative delta function, respectively, at time t when there is a negative and positive delta function at time t':

$$p_0(t) = \frac{d}{dt}[1 - \pi_0(t)], \tag{3.4a}$$

and

$$p_1(t) = \frac{d}{dt}[1 - \pi_1(t)]. \tag{3.4b}$$

One then finds

$$\langle y(t)\rangle_+ = - p_1(t) + \int_0^t dt' p_0(t - t') p_1(t') - \int_0^t dt' p_1(t - t') \int_0^{t'} dt'' p_0(t' - t'') p_1(t'') + \ldots , \tag{3.5}$$

together with an analogous expression for $\langle y(t)\rangle_-$ by interchanging 0 and 1 and + and - in Eq. (3.5). The nth term in this infinite series corresponds to the situation in which there are n delta functions between 0 and t.

We can resum these series expansions using Laplace transforms

$$\text{L.T.}\{f(t)\} = \tilde{f}(z) = \int_0^\infty e^{-zt} f(t) dt, \tag{3.6}$$

and making use of the property

$$\text{L.T.}\left\{ \int_0^t dt' f(t - t') \int_0^{t'} dt'' g(t' - t'') \right\} = \tilde{f}(z)\tilde{g}(z). \tag{3.7}$$

We obtain

$$\begin{aligned} \text{L.T.}\{\langle y(t)\rangle_+\} &= - \tilde{p}_1(z) + \tilde{p}_0(z)\tilde{p}_1(z) - \tilde{p}_1(z)\tilde{p}_0(z)\tilde{p}_1(z) + \ldots \\ &= \frac{- \tilde{p}_1 + \tilde{p}_0\tilde{p}_1}{1 - \tilde{p}_0\tilde{p}_1} , \end{aligned} \tag{3.8}$$

and a similar expression for $\langle y(t)\rangle_-$. Subtracting the two expressions and rewriting the result in terms of $\tilde{\pi}_0(z)$ and $\tilde{\pi}_1(z)$, we obtain

$$\tilde{g}(z) = 1/2\left[z^{-1}\left[\tilde{\pi}_0^{-1}(z) + \tilde{\pi}_1^{-1}(z)\right] - 1\right\}^{-1} . \tag{3.9}$$

We can easily compute the Fourier transform $\tilde{g}(\omega)$ of g(t) from the result

$$\tilde{g}(\omega) = \int_{-\infty}^{\infty} e^{-i\omega t} g(t)dt = \lim_{z \to i\omega} [\tilde{g}(z) + \tilde{g}(\bar{z})], \qquad (3.10)$$

where $\bar{z}$ is the complex conjugate of z. Finally, we obtain the required spectral density of x(t)

$$S_x(\omega) = \frac{2}{\langle\tau_0\rangle + \langle\tau_1\rangle} \frac{\tilde{g}(\omega)}{\omega^2} . \qquad (3.11)$$

3. Self-Similar Power Spectra

We are now in a position to determine the conditions that must be satisfied by $\pi_0(t)$ and $\pi_1(t)$ so that the power spectrum $S_x(\omega)$ diverges in the limit $\omega \to 0$ as $A\omega^{-\nu}$, where A and ν are positive constants. We restrict ourselves to distributions that have a well-defined power law behavior as $t \to \infty$. To leading order, we take

$$\pi_0(t) \underset{t \to \infty}{=} a_0 t^{-\beta_0} \qquad (\beta_0 > 0) \qquad (3.12a)$$

$$\pi_1(t) \underset{t \to \infty}{=} a_1 t^{-\beta_1} \qquad (\beta_1 > 0). \qquad (3.12b)$$

Exponentially decreasing distributions can be treated by letting $\beta \to \infty$. Using Eq. (3.9) and tables of Laplace transforms (Abramowitz and Stegun, 1964), we obtain the values of ν as a function of β_0 and β_1 listed in Table 3.1. A plot of ν versus β_0 and β_1 is given in Fig. 29.

4. One-Dimensional Mappings

We turn now to a discussion of how one can obtain probability distributions corresponding to Eq. (3.4) from a physically realizable mechanism. From the work of Manneville (1980) we know that a one-dimensional mapping can generate a signal consisting of a seemingly random alternation between long quiescent intervals and short irregular bursts.

We can apply Manneville's ideas to generate a signal consisting of

TABLE 3.1. Dependence of ν or $S_x(\omega)$ on β_0 and β_1

β_0,β_1	ν or $S_x(\omega)$
$\min(\beta_0,\beta_1) > 2$	$\nu = 0$
$\min(\beta_0,\beta_1) = 2$	$S_x(\omega) \sim \lvert \ell n\omega \rvert$
$1 < \min(\beta_0,\beta_1) < 2$	$\nu = 2 - \min(\beta_0,\beta_1)$
$\min(\beta_0,\beta_1) = 1,\ \max(\beta_0,\beta_1) > 1$	$S_x(\omega) \sim 1/\omega \lvert \ell n\omega \rvert^2$
$\beta_0 + \beta_1 > 2,\ \min(\beta_0,\beta_1) < 1$	$\nu = \min(\beta_0,\beta_1)$
$\beta_0 + \beta_1 \leq 2$	$\nu = 2 - \max(\beta_0,\beta_1)$

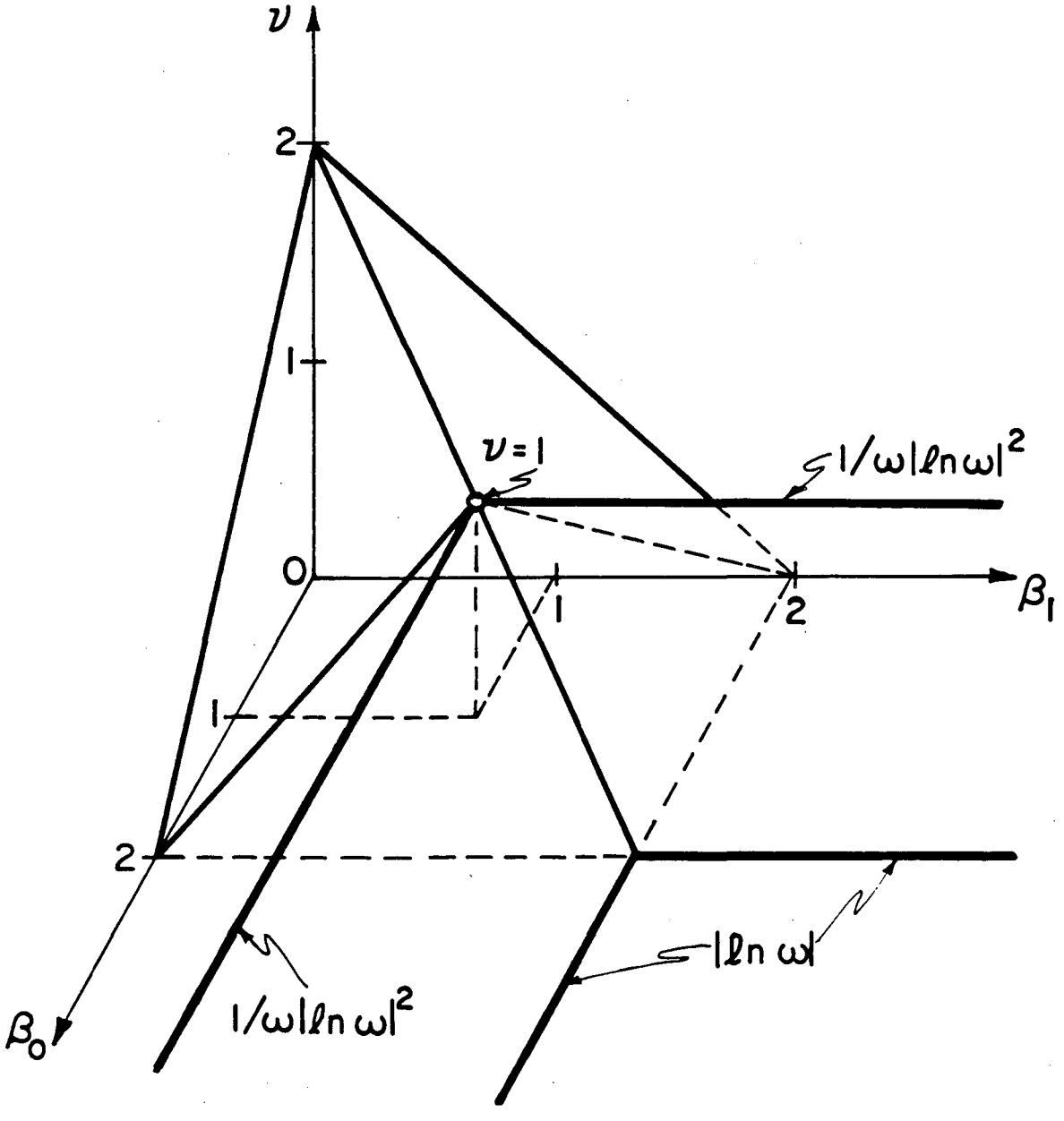

XBL 846-7111

Figure 29. Variation of ν, where $S(\omega) \sim \omega^{-\nu}$, as a function of β_0 and β_1. The heavy lines indicate singular regions of the function, where the frequency dependence of $S(\omega)$ contains logarithmic corrections as indicated.

switching events such that the time interval between two events obeys a scaling law. Consider the map in Fig. 30 that has two marginally unstable fixed points at $x = 0$ and $x = 1$, instead of only one unstable fixed point as in Manneville's map. Near each fixed point, the map can be expanded as

$$\Delta x_{n+1} = \Delta x_n[1 + \lambda(\Delta x_n)^{\alpha}], \tag{3.13}$$

where Δx is the distance to the fixed point. (The figure has been drawn for the particular case $\lambda = 2$, $\alpha = 1$.) The exponents α and coefficients λ in general differ for the two fixed points, and will be denoted by α_0 and λ_0 for $x = 0$ and α_1 and λ_1 for $x = 1$. We take as our switching process the signal obtained when we iterate the map $x_n \to x_{n+1}$, assigning the value 0 or 1 to x when x_n is on the branch corresponding to the fixed point $x = 0$ or $x = 1$, respectively.

Manneville (1980) showed that the probability distribution of the times spent on a branch behaves for long times as

$$\pi(t) = (1 + \alpha\lambda t)^{1/\alpha}, \qquad (t \to \infty) \tag{3.14}$$

where the time is in units of the duration of one iteration. We note that a Poisson switching process, that is $\pi(t) = e^{-mt}$, corresponds to $\alpha \to 0$.

Combining Eqs. (3.13) and (3.14) with the results for $\nu(\beta_0,\beta_1)$ shown in Table 3.1, one obtains the exponent ν of the power spectrum in the limit $\omega \to 0$ which is a universal quantity depending only on the exponents α_0 and α_1 of the map. The variation of ν with α_0 and α_1 is shown in Table 3.2. In the limit $\alpha_1 \to 0$ where the switching signal degenerates to a random succession of bursts of characteristic duration λ_1^{-1},

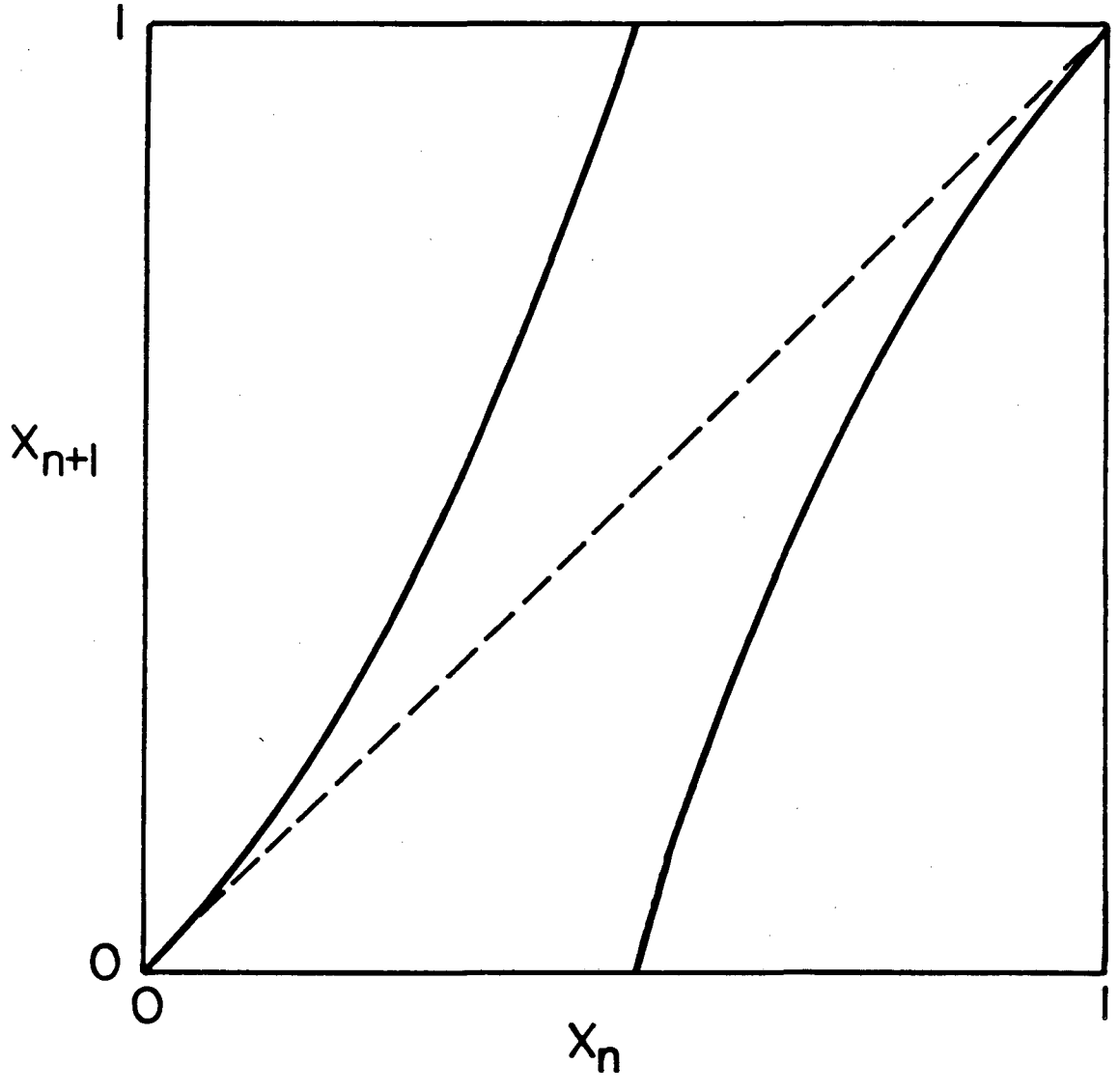

Figure 30. One-dimensional mapping of the interval [0,1], given by: $\Delta X_{n+1} = \Delta X_n(1 + 2\Delta X_n)$, where $\Delta X_n = X_n$ for $0 \leq X_n < 1/2$, or $\Delta X_n = 1 - X_n$ for $1/2 < X_n \leq 1$.

TABLE 3.2. Dependence of ν or $S_x(\omega)$ on α_0 or α_1

α_0,α_1	ν
$\max(\alpha_0,\alpha_1) < 1/2$	0
$\max(\alpha_0,\alpha_1) = 1/2,\ \min(\alpha_0,\alpha_1) \leq 1/2$	$S_x(\omega) \sim \lvert \ell n\omega \rvert$
$1 > \max(\alpha_0,\alpha_1) > 1/2$	$2 - [\max(\alpha_0,\alpha_1)]^{-1}$
$\max(\alpha_0,\alpha_1) = 1,\ \min(\alpha_0,\alpha_1) < 1$	$S_x(\omega) \sim 1/\omega \lvert \ell n\omega \rvert^2$
$\max(\alpha_0,\alpha_1) > 1,\ 1/\alpha_0 + 1/\alpha_1 > 2$	$[\max(\alpha_0,\alpha_1)]^{-1}$
$1/\alpha_0 + 1/\alpha_1 \leq 2$	$2 - [\min(\alpha_0,\alpha_1)]^{-1}$

we recover the results of Procaccia and Schuster (1983).

We have carried out a numerical test of our predictions for the case $\alpha_0 = \alpha_1 = 1$ which gives an exact $1/\omega$ power spectrum without the logarithmic corrections that one obtains for the Manneville mapping. We iterated the map shown in Fig. 30 on a computer 3×10^6 times for one set of initial conditions and obtained the power spectrum shown in Fig. 31. The sequence of iterates was Fourier transformed in two different ways to obtain the overlapping sets of spectral estimates shown in the figure. The squares are the averaged results of about 700 individual records of 4096 points each, while the triangles are the averages of about 50 records of 4096 points each, obtained after a tenth-order decimation of the original sequence of iterates. At low frequencies the power spectrum scales as $1/\omega$, down to the lowest frequency data point.

C. Equations of Motion

The application of Kirchoff's laws to the circuit shown in Fig. 1 yields the equations

$$I = I_0 \sin\delta + (\Phi_0/2\pi)C\,\ddot{\delta} + I_S + I_{qp} \tag{3.15}$$

and

$$(\Phi_0/2\pi)\dot{\delta} = RI_S + L\dot{I}_S + V_N, \tag{3.16}$$

where $V_N(t)$ is the thermal voltage noise generated by the resistance R; since $R \ll 1/\sigma_{qp}$ for situations of practical interest, we neglect the thermal noise voltage associated with σ_{qp}. To simplify the situation, we assume that σ_{qp} is linear over the voltage range of interest with the dimensionless value $\sigma = R\sigma_{qp}$. It is more convenient to write Eqs. (3.15) and (3.16) in dimensionless form. If we introduce a dimensionless time $\tau = (2\pi I_0 R/\Phi_0)t$, Eqs. (3.15) and (3.16) become:

$$i = \sin\delta + \beta_C\,\ddot{\delta} + i_S + \sigma\dot{\delta} \tag{3.17}$$

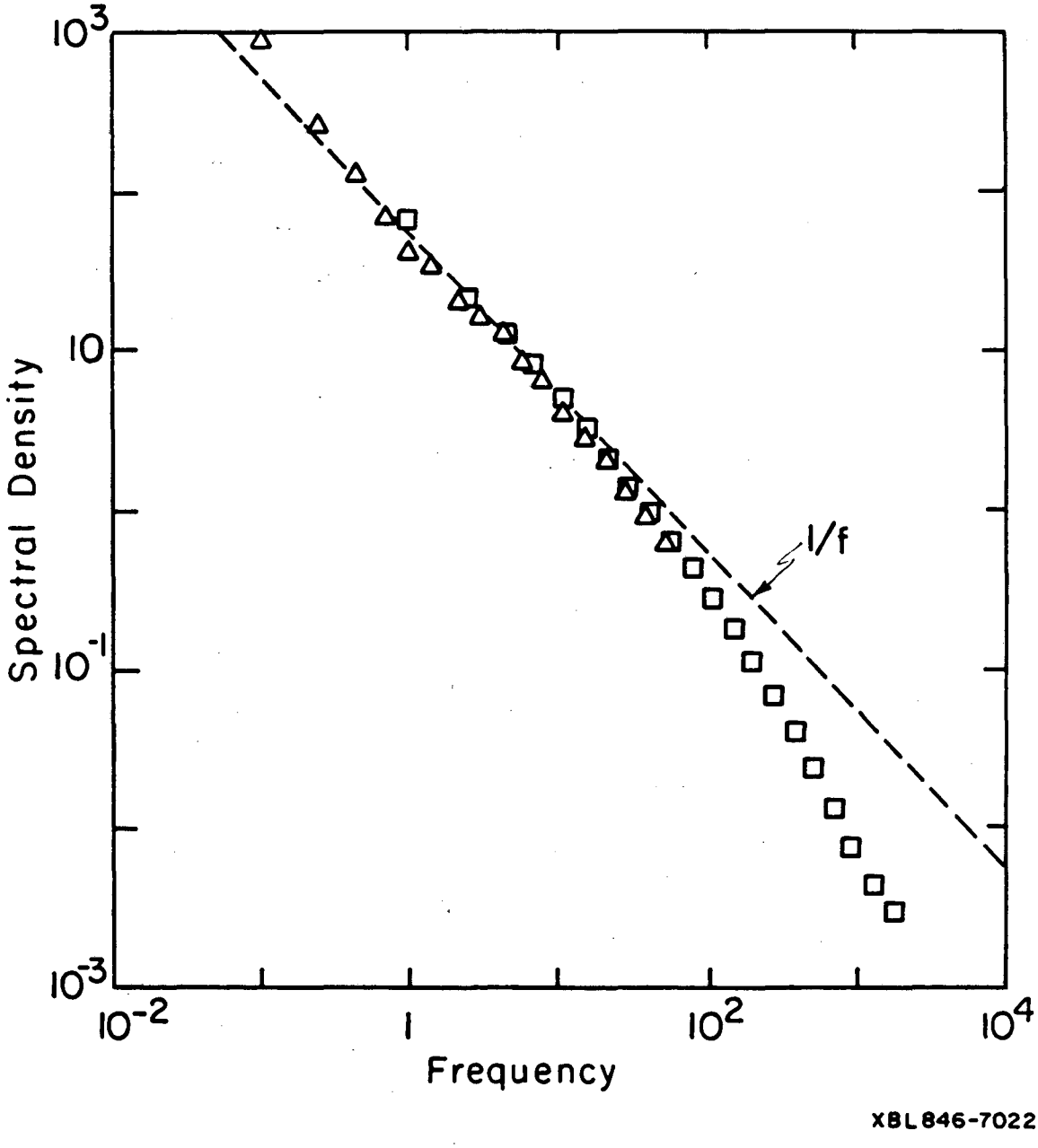

Figure 31. Power spectrum of the iterates of the mapping of Fig. 30. Different symbols denote different frequency bands for the 4096-point fast Fourier transform.

and

$$\dot{\delta} = i_S + \beta_L \dot{i}_S + v_N, \tag{3.18}$$

with $i = I/I_0$, $i_S = I_S/I_0$, $v_N = V_N/I_0R$, $\beta_C = 2\pi I_0 R^2 C/\Phi_0$, and $\beta_L = 2\pi L I_0/\Phi_0$. The dots now denote differentiation with respect to τ. The magnitude of the voltage noise is characterized by $\Gamma = 2\pi k_B T/ I_0\Phi_0$, the ratio of thermal noise to the junction coupling energy.

Although there has been some analytical work on the dynamics of this system -- Wiesenfeld et al. (1984) have calculated to good accuracy the threshold for the first period-doubling bifurcation as the bias current i is reduced from some large value -- most of the insight into the complicated dynamics of the system has been achieved with both analog and digital simulations (Miracky, Clarke, and Koch, 1983; Koch, Miracky, and Clarke, 1984). The next section is devoted to simulations associated with the deterministic hopping process.

D. Simulations

1. Analog Simulations

One signature of an intrinsic hopping process is excess low frequency noise in a power spectrum. Figure 32 shows a voltage power spectrum obtained from an electronic analog (commercially manufactured by Philip Gillette and Associates, Beaverton, Oregon) of the circuit shown in Fig. 1 for one set of parameter values ($\beta_L = 4.0$, $\beta_C = 0.37$, $i = 2.36$, $\sigma = 0.004$) where this excess low-frequency noise was observed. There was no added voltage noise, and the intrinsic, system noise of the analog was estimated to be such that $\Gamma_{sys} = 3\times10^{-7}$. The spectrum scales approximately as 1/f between normalized frequencies 10^{-4} and 10^{-2}, and is seen to flatten out below 10^{-4}. The large peak near 10^{-1} and the one slightly lower in frequency correspond to residual subharmonic modes.

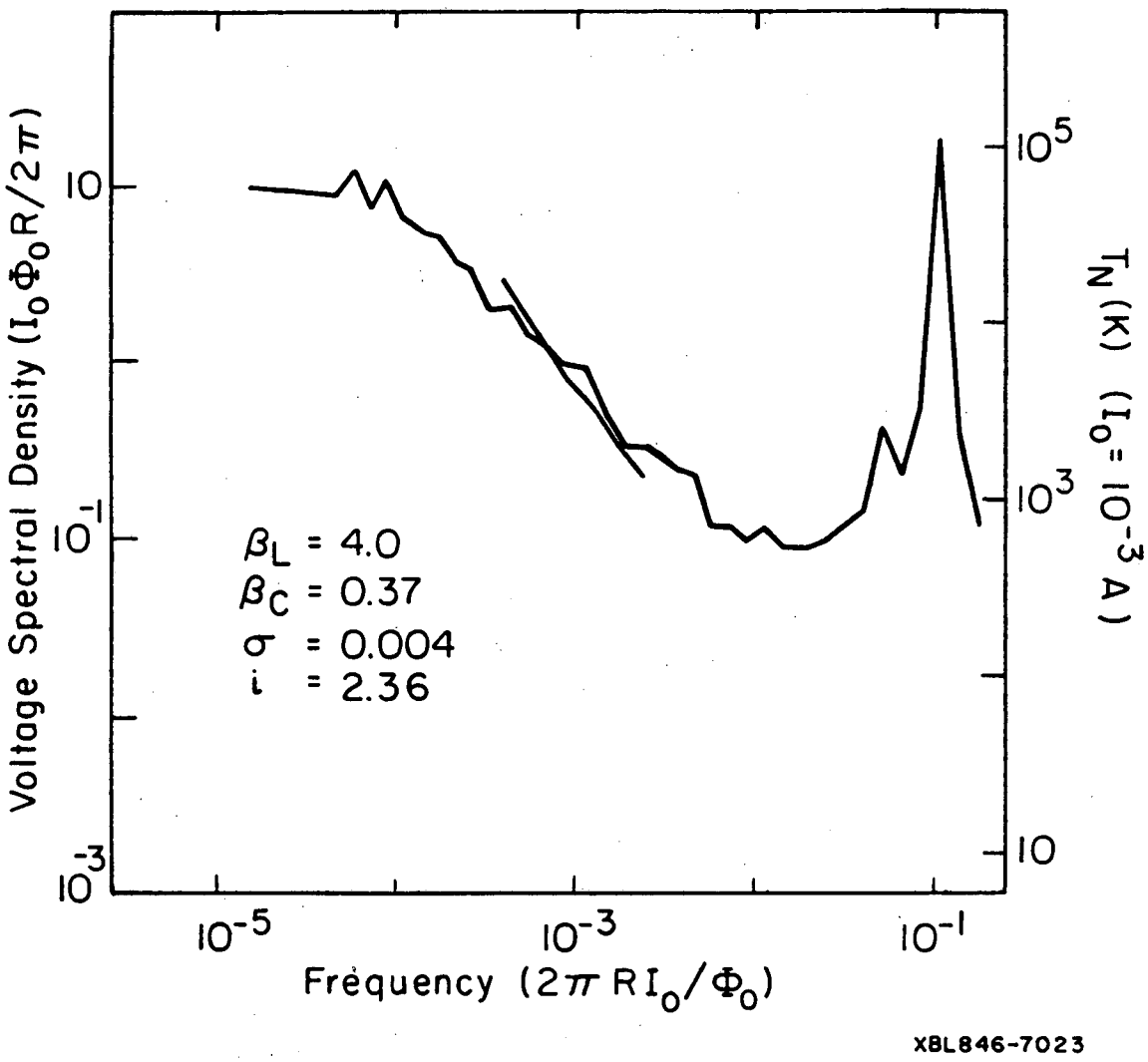

Figure 32. Voltage power spectrum for an electronic analog of the circuit shown in Fig. 1, with parameters chosen to maximize the region over which excess low-frequency noise is observed: $\beta_L = 4.0$, $\beta_C = 0.37$, $o = 0.004$, $i = 2.36$, and $\Gamma = \Gamma_{sys}$. (The spectrum was computed over two overlapping frequency intervals.)

Their linewidths are in fact narrower than is apparent: The broadening is an artifact of an averaging of adjacent Fourier harmonics.

By monitoring the time sequency of the voltage, we conclude that this low frequency noise originates in a two-mode hopping process, rather than in some other process. The steady-state waveform spends random time intervals in one of two distinct nearly-periodic modes that differ in one important aspect. While in one mode δ increases monotonically with time (i.e. $\dot{\delta} > 0$), in the other $\dot{\delta}$ is periodically negative. Although the latter behavior is impossible for $\beta_L = 0$, it occurs commonly for $\beta_L \geq 1$ and represents a "relaxation oscillation" (Dempsey, Levinsen, and Ulrich, 1975). In this mode, the junction oscillates for a while at the Josephson frequency (determined by the voltage across the junction), and then relaxes to a state with zero average voltage in which the junction undergoes damped oscillations at the plasma frequency, $\omega_0 = (2\pi I_0 \cos\delta/\Phi_0 C)^{1/2}$. The junction subsequently returns to the non-zero voltage regime, and the cycle repeats. Bearing in mind the pendulum analog of the Josephson junction (Fig. 2), which we introduced in Chapter II, we label the mode for which $\dot{\delta}$ is always positive as the "grabbing mode" and that in which relaxation oscillations occur as the "slipping mode".

It is clear that neither mode is stable, so that the system satisfies the requirement of two unstable fixed points described in Sec. B. Moreover, the two modes are characterized by two different average voltages, so that we can represent the long-time behavior as a switching process between two constant voltages, as in the telegraph signal of Fig. 28(b). However, these requirements are not sufficient to produce 1/f noise, since the power spectrum depends critically on the nature of

the mapping in the vicinity of the fixed points.

An important aspect of this hopping process is that, unlike the situation described by Miracky, Clarke, and Koch (1983), it occurs in the absence of added white (Nyquist) noise. Although the residual white noise in the electronic analog ($\Gamma_{sys} = 3 \times 10^{-7}$) cannot be entirely ruled out as a source of the hopping, we found that the low-frequency power spectrum was not significantly affected until we added a noise equivalent to several hundred milliKelvin. Furthermore, we found that the power spectrum was much more sensitive to the value of the bias current than is the case for the noise-induced hopping. Both of these results suggest that the switching arises deterministically from the governing equations. We note that for the deterministic hopping, the 1/f noise was relatively insensitive to the values of β_C and β_L, either of which could be varied over a range of perhaps 10 to 20% before the hopping ceased.

2. Digital Simulations

To eliminate the possibility that the residual noise of the analog induced the hopping and to study the dynamical processes in greater detail, we performed extensive double-precision digital computations for a similar set of parameters to those we studied on the analog simulator. We integrated Eqs. (3.17) and (3.18) numerically, using a fourth-order Adams-Bashford-Moulton predictor-corrector method (Lambert, 1973), with typical time steps of 10^{-2} yielding local truncation errors estimated to be $\leq 10^{-9}$. For each set of parameters, starting from an arbitrary set of initial conditions, we computed typically 320 Josephson cycles to allow any start-up transients to die out before including the data in power spectra or maps. Figure 33 shows a typical time sequence computed

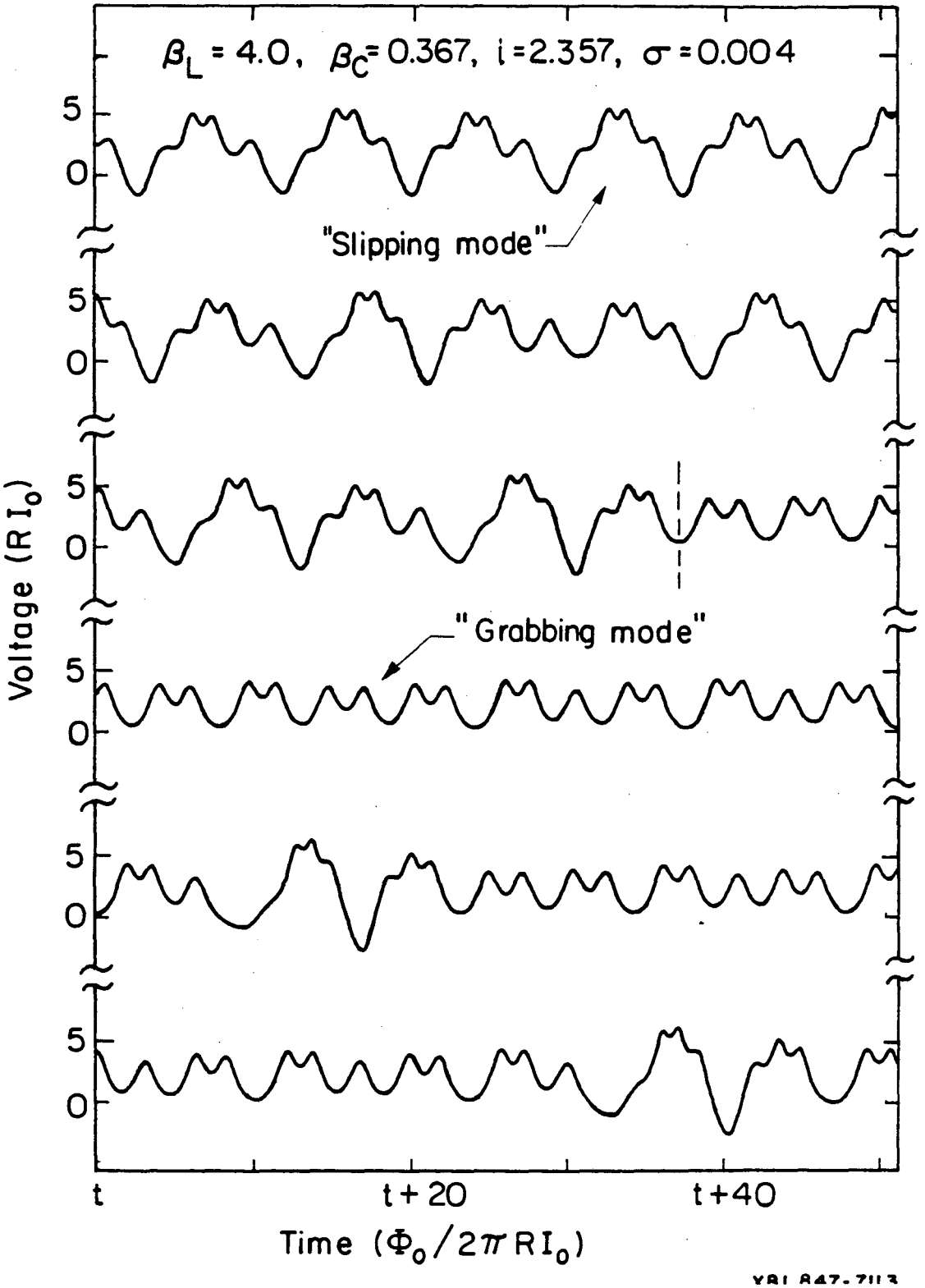

Figure 33. Representative time sequence (time increasing from left to right and from top to bottom) obtained by numerical integration of the the equations governing the circuit of Fig. 1 for β_L = 4.0, β_C = 0.367, σ = 0.004, i = 2.357, and Γ = 0. An example of a switching event is indicated by the dashed line separating the two modes labelled "Slipping" and "Grabbing."

in this way, for the parameter values $\beta_L = 4.0$, $\beta_C = 0.367$, $i = 2.357$, $\sigma = 0.004$ and $\Gamma = 0$. An example of a switching event is indicated by the dashed line, where the system undergoes a transition from the slipping mode to the grabbing one.

The results are presented in three ways that we now describe in detail: Voltage spectral densities, Poincaré maps, and return maps. The voltage spectral densities were computed from the time sequences using a 4096-point Fast Fourier Transform algorithm. However, because we are interested only in extremely low frequency behavior resulting from high frequency processes computed with small time steps, the time sequences were first passed through a digital low-pass filter prior to a high-order (typically 100-500) decimation. These filtered time sequences were Fourier transformed and the 2048 harmonics were averaged into 25 frequency windows equally spaced on a logarithmic scale. The results for several such records (typically five) were averaged together. The effects of thermal noise were simulated by introducing pseudorandom voltage impulses [to represent the v_N of Eq. (3.18)] at each time step; the magnitude of the Fourier transform of these impulses is a constant proportional to $\Gamma^{1/2}$.

Typical power spectra are shown in Fig. 34 for parameters β_L, β_C, i, and σ close to those used in Fig. 32. The top curve is for $\Gamma = 0$, and is the one referenced by the axes. The lower curves are for non-zero Γ, expressed in terms of an equivalent ambient temperature for a junction critical current of 1 mA: $T = \Phi_o(1\ \text{mA})\Gamma/2\pi k_B$. The lower curves have been successively displaced by 10 dB for clarity. The power spectra at the lowest two temperatures are approximately 1/f over rather more than one decade, and flat at low frequencies. On the other hand, we see that

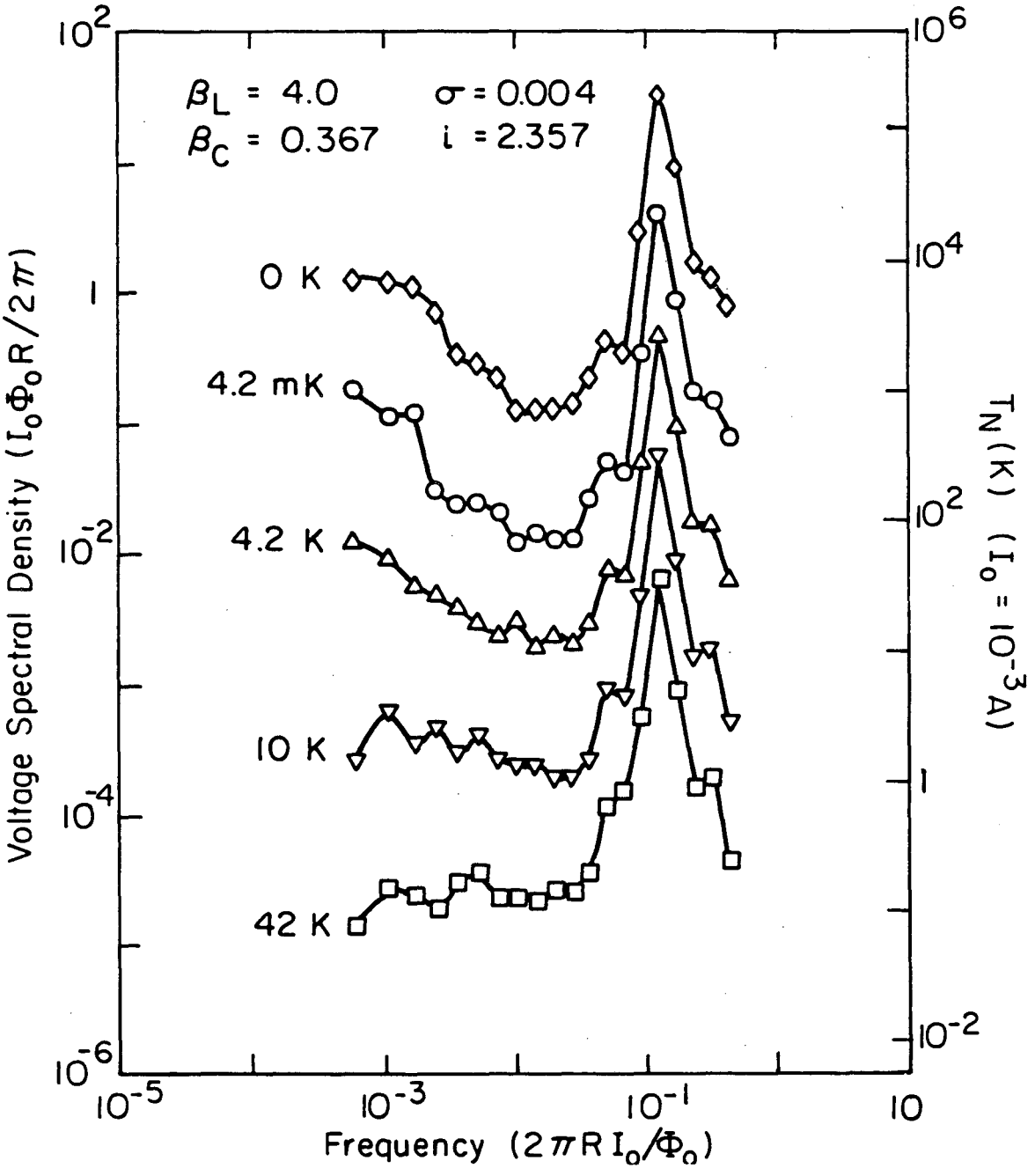

Figure 34. Power spectra of the voltage for β_L = 4.0, β_C = 0.367, σ = 0.004, i = 2.357, and for five levels of injected noise. The temperature T associated with each curve is the level of injected noise, defined as:

$$T = \Gamma\Phi_0(1\ \text{mA})/2\pi k_B.$$

The spectral density and noise temperature scales refer to the top curve; the lower curves have been offset by factors of ten in power for clarity.

for T = 4.2K the spectrum has already been modified by the external noise, and that for T $\geq$ 42K, the spectrum is nearly white below 10^{-2}. We can conclude that this level of thermal noise is sufficient to destroy the long-term correlations necessary for 1/f noise.

The very strong dependence of the low-frequency noise on the value of the bias current (in the absence of added thermal noise) is illustrated in Fig. 35. For i = 2.365 (solid curve with open circles) the motion consists of a stable subharmonic limit cycle. A slight decrease in the bias current, to 2.361 (solid circles), has little effect on the subharmonic mode, but produces a low frequency tail that probably indicates the onset of intermittency. When the current is decreased to 2.358 (solid curve), the low frequency power spectrum is at a maximum, with a 1/f region. The decrease in bias current from 2.365 to 2.358 (0.3%) has increased the level of noise by over five orders of magnitude. A further small decrease in the current (dashed curve) produces a low frequency noise that is white, indicating that the system has become fully chaotic.

To obtain more information on the modes between which the system hops, particularly with regard to the presence of any strange attractors, in Fig. 36 we show a Poincaré section at $\delta = \pi$ for the parameter values used in Figs. 33 and 34. The points lie on a smooth curve that is highly contracted, and thus nearly one-dimensional over much of the phase space. When one monitors the time sequences of the iterates, one sees the same behavior as with the analog simulator: The system spends varying amounts of time, that occasionally become very long, in one of two modes. One is the slipping mode, near an unstable period three limit cycle for which the iterates lie within the encircled regions.

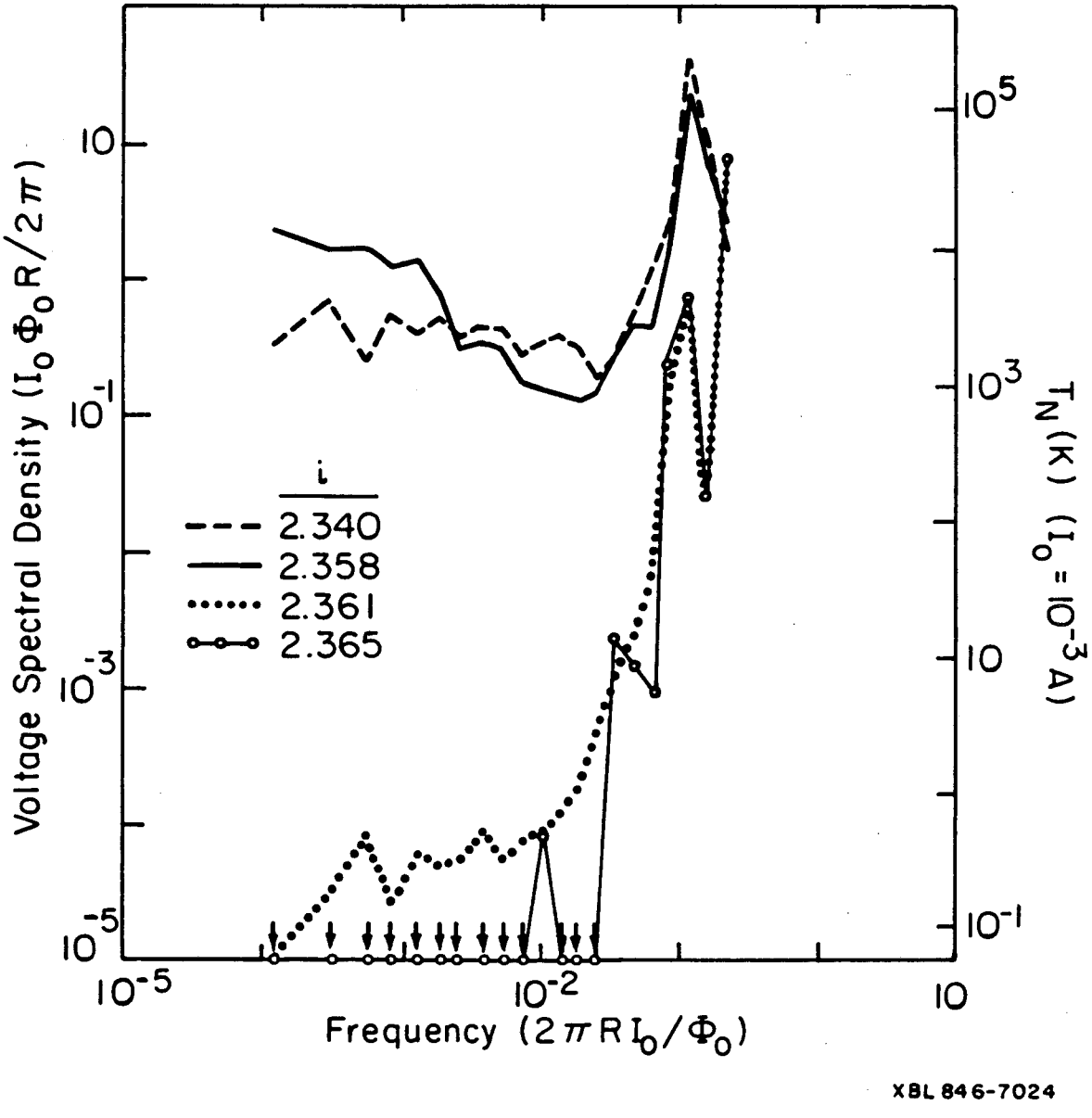

Figure 35. Power spectra of the voltage for β_L = 4.0, β_C = 0.367, σ =0.004, Γ = 0, and for several values of i. The downward pointing arrows indicate that the noise is less than 10^{-5}.

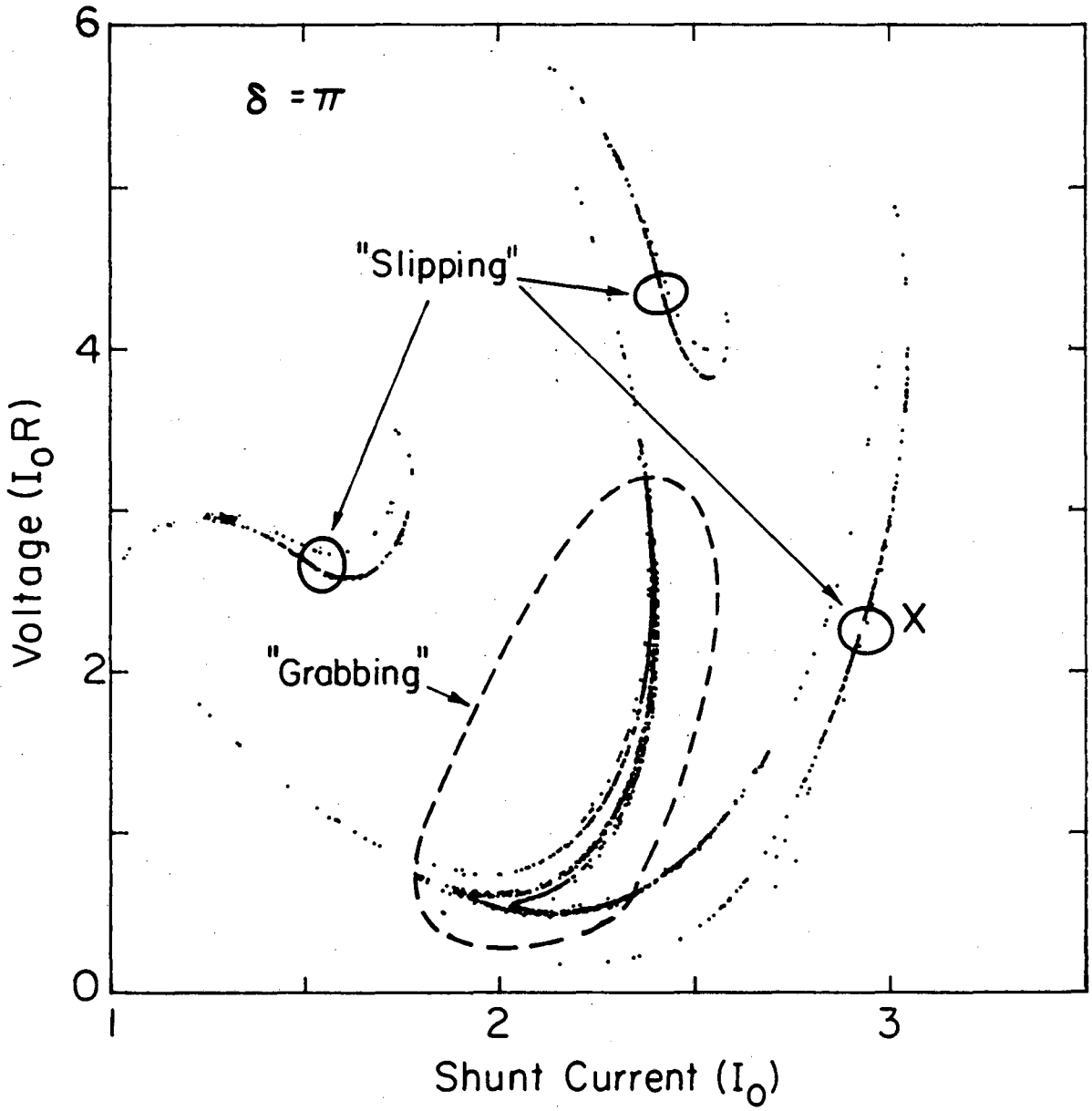

Figure 36. Poincaré map of the voltage vs shunt current for $\delta = \pi$, $\beta_L = 4.0$, $\beta_C = 0.367$, $\sigma = 0.004$, $i = 2.357$, and $\Gamma = 0$. The grabbing (unstable period one) and slipping (unstable period three) modes are identified.

Iterates that land near to the fixed points slowly evolve away, as is apparent from the darkened portions of the attractor near the fixed points. The other, grabbing mode consists of a chaotic motion along a subsurface of the entire attractor, in the region enclosed approximately by the dashed curve. The points that lie outside these two regions represent transition points between the two modes. (Note that these points, although "transient" in the sense of not belonging to either mode, are still points on the attractor -- they do not represent "start-up" transients.) In that the long time behavior is determined by the nature of the mapping in the immediate vicinity of the fixed point (the limit cycle of the motion), these transition points can be ignored provided that the mechanism that controls the reinjection into either mode is nearly random.

The precise character of the mapping must be determined from a return map of one variable. In order for the mapping to correspond to the theory described in Sec. B, it must both be one-dimensional and have a power law departure from linearity. The return map constructed from points near the fixed point X of Fig. 36 is illustrated in Fig. 37(a). Here we plot the third-iterate mapping, v_{n+3} vs. v_n, in order to analyze the stability of the period three relaxing mode. As the points are generated, they appear alternately on either side of the 45° line. We notice that the map is very nearly one-dimensional, particularly near the fixed point where the mapping intersects the dashed 45° line. The fact that the mapping is very nearly tangential to a -45° line drawn through the fixed point indicates that the loss of stability of this period three limit cycle occurs via a bifurcation with a FM equal to -1. Hence, the ensuing intermittency is type III (Pomeau-Manneville). The

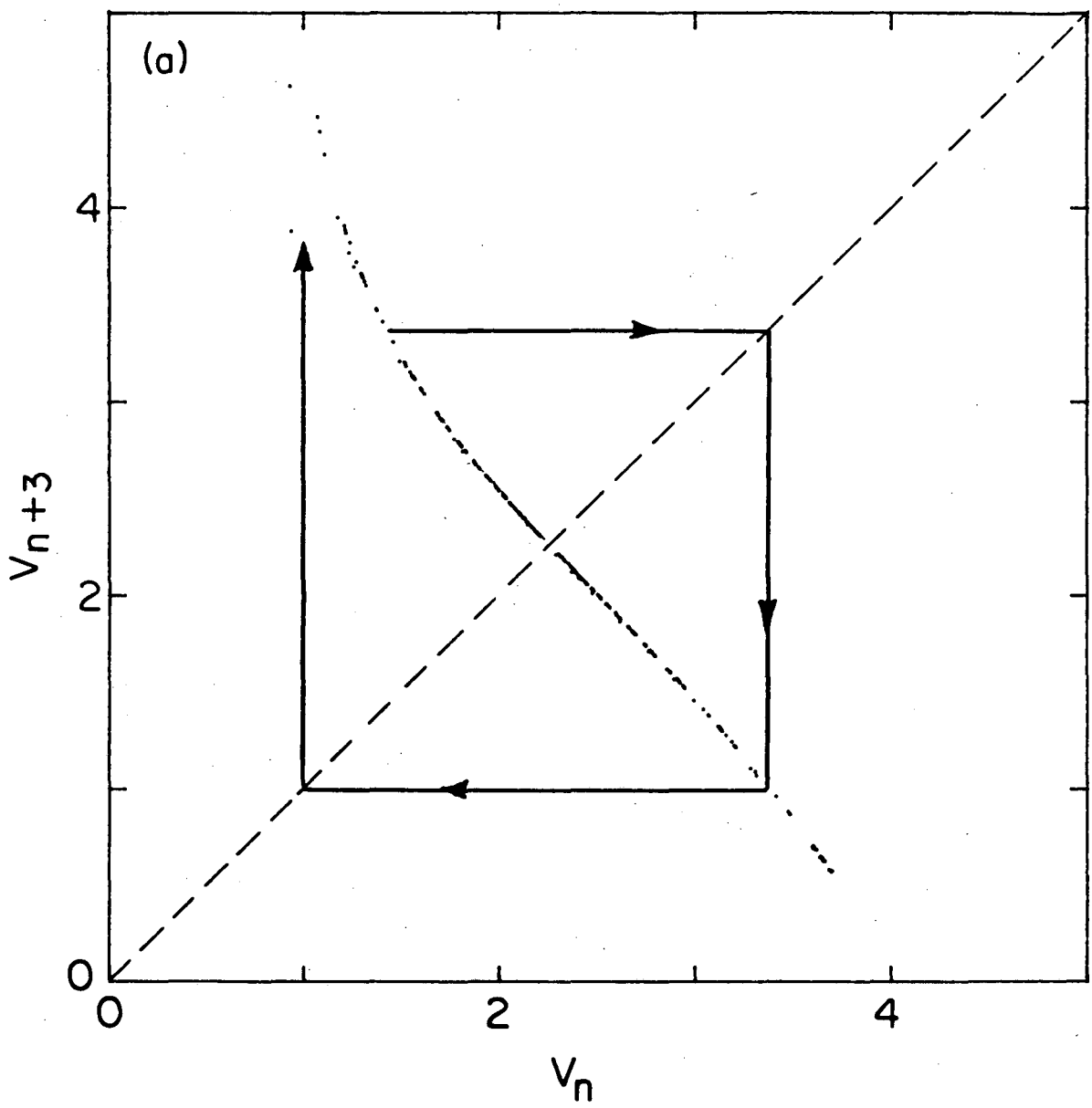

Figure 37. (a) Return map of the voltage for points near the iterate of the slipping mode identified by an "X" in Fig. 36. (b) Second iterate of the mapping in Fig. 37(a), which yields the sixth iterate of the original voltage sequence.

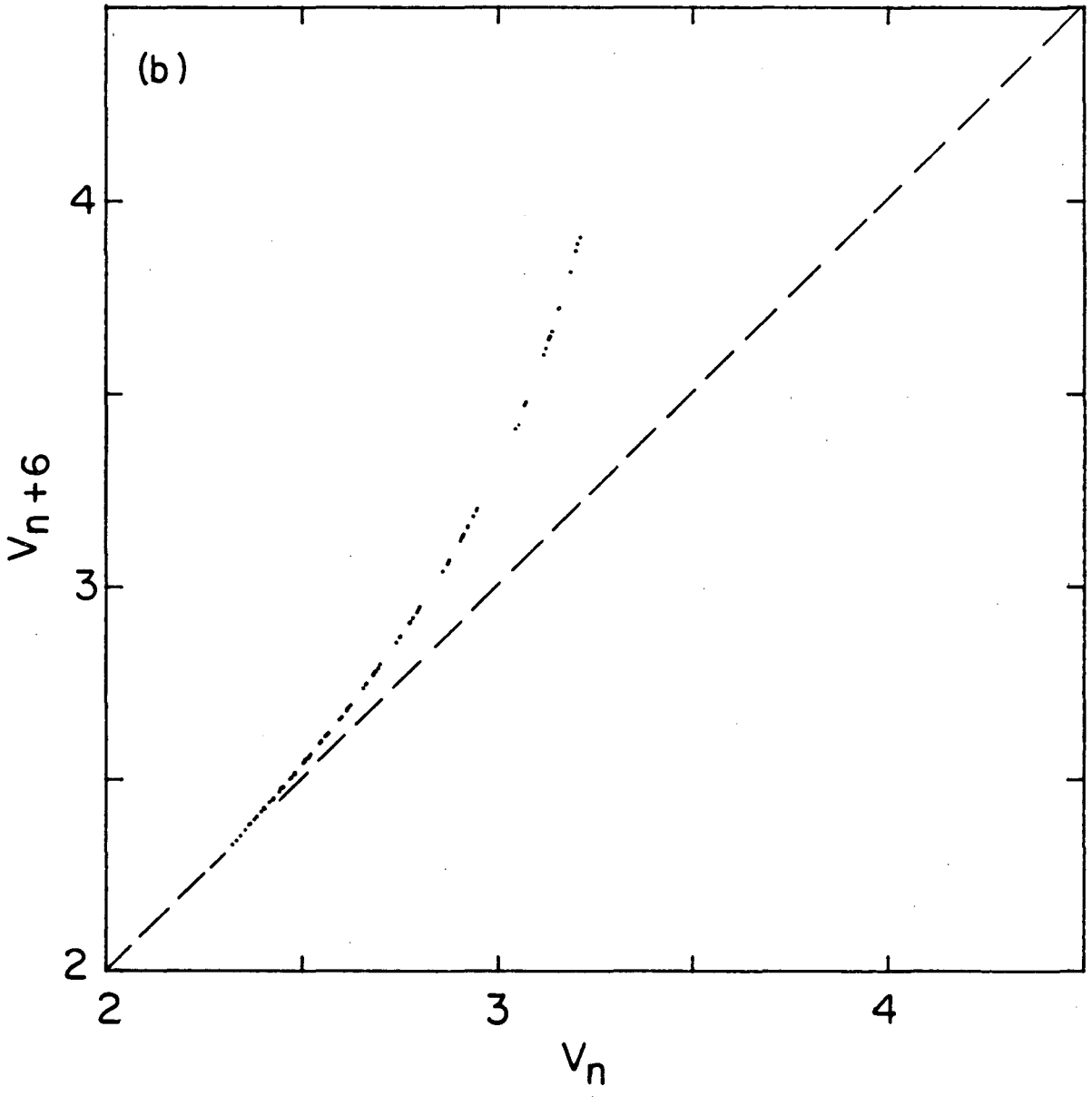

XBL 846-7027

departure of the mapping from -45° is approximately linear on the lower branch, and roughly quadratic on the upper branch. The curve shown illustrates how iterates that are injected close to the fixed point inevitably spiral away; this evolution originates in the quadratic shape of the upper branch.

We now compare the mapping of Fig. 37(a) with the simple model described in Sec. B. We obtain a new map, shown in Fig. 37(b), by taking the second iterate of the points on the upper branch of Fig. 37(a): This procedure corresponds to plotting v_{n+6} vs. v_n. The similarity between the mapping of Fig. 37(b) and the behavior near the origin in Fig. 30 is striking. We have performed a least squares fit to the function

$$v_{n+3} - v_{n,0} = -(1 + \varepsilon)(v_n - v_{n,0}) + \alpha(v_n - v_{n,0})^2 + \beta(v_n - v_{n,0})^3 + \gamma(v_n - v_{n,0})^4 \qquad (3.19)$$

for the points shown in Fig. 36(a), and find $v_{n,0} = 2.25669$, $\varepsilon = 0.02528$, $\alpha = 0.06521$, $\beta = -0.30064$, and $\gamma = 0.13260$. The fact that ε is small is consistent with the fact that the noise extends to low frequencies: The lower cut-off frequency in the spectrum of the noise should vary inversely as a power of ε (Procaccia and Schuster, 1983). Also, the significant quartic component allows for an asymmetry in the mapping about the fixed point, and hence permits a spectrum which is more 1/f-like than what one would expect from a simple period doubling ($S \sim \omega^{-1/2}$ for type III intermittency). We conclude that this system has a self-similar distribution of times spent in the vicinity of the period three limit cycle. However, the stability of the chaotic grabbing mode is not easily extracted from the Poincaré mapping of Fig. 36, since the mapping is not obviously one-dimensional and Eq. (3.9) cannot be solved in closed form. We emphasize, however, that this difficulty does not in-

validate the model discussed in Sec. B. If one were to compute the distribution of times spent in the rotating mode, one could still compute the power spectrum from Eq. (3.9).

Finally, there remains the question of why the computed 1/f region shown in Fig. 34 extends over such a limited range of frequencies. We have ruled out significant errors due to the truncations in the numerical methods. One expects a local truncation error, Δx_t, to give rise to a distortion of the power spectrum at frequencies below Δx_t. However, the power spectrum flattens out at frequences of about 10^{-3}, while Δx_t is about 10^{-9}. Instead, there are two other reasons that perhaps explain the low frequency cut-off. First, the mapping in Fig. 37(a) is not exactly tangential to the -45° line, and so deviates slightly from the mapping of Fig. 30. Second, the reinjection of the iterates back into the vicinity of the fixed point might not be entirely uniform and random as is assumed in the model. Both of these effects, especially the slope of the mapping, depend on the choice of parameters in a complicated way. However, one would expect that the mapping could be adjusted by varying one of the parameters, so that the 1/f region extended over a larger frequency range as the mapping became more ideal. The extreme sensitivity of the power spectrum to the bias current (Fig. 35) supports this argument. We note also that the region of 1/f noise was greater in the analog simulations (Fig. 32) than in the digital simulations, presumably because in the analog case one can more readily optimize the values of the appropriate parameters. We note, however, that because the mapping of the physical system must be analytical at the fixed point, it could never consist exclusively of a quadratic upper branch and a -45° linear lower branch intersecting at the fixed point.

Thus, although the mapping representing the physical system may approach the mapping of Fig. 30 arbitrarily closely, it may never achieve it precisely.

E. Concluding summary

We have shown analytically that a deterministic switching process represented by a one-dimensional mapping can produce a spectral density that scales as 1/f for a particular choice of parameters. Numerical simulations confirm the analytical results. We have investigated the applicability of this model to a current-biased Josephson tunnel junction, shunted with its self-capacitance and with a resistance in series with an inductance. Analog simulation and numerical integration of the differential equation representing this circuit demonstrate that, for appropriate parameters, the system switches deterministically between two modes, one a "grabbing mode" and the other a "slipping mode". This process is analogous to type III intermittency, and as such is a route to chaos. The switching process manifests itself as an excess low frequency noise with a frequency range and dependence that are determined by the nature of the evolution in phase space in the vicinity of an unstable oscillatory mode. The addition of a small amount of white noise, representing the Nyquist noise in the shunt resistor, destroys the excess low-frequency noise. Poincaré and return mappings show that the underlying dynamics can be represented by a one-dimensional mapping of one of the dynamical variables, namely the voltage across the junction. The fact that the 1/f power spectrum extends over only a modest range of frequencies is probably due to a small imprecision in the choice of parameters in the simulations, and to the analytical properties of the mapping.

There remains the question of the relationship of this work to experiments performed on real junctions, which inevitably exhibit Nyquist noise. As already mentioned, the spectra for both the noise-induced and deterministic processes are very similar, and one could not distinguish between the two processes from a study of the spectra alone. It is possible that a reduction in the ambient temperature, and hence in the level of Nyquist noise, could resolve this difficulty: One would expect the noise-induced process to be reduced and the deterministic process to be enhanced. One should bear in mind, however, that if the temperature is reduced sufficiently, quantum effects (Koch, Van Harlingen, and Clarke, 1982) will set a lower limit on the level of intrinsic noise. Thus, it appears that the full experimental demonstration of the ideas presented in this Chapter, although not necessarily out of the question, will be quite difficult. The contribution of this work lies in the demonstration that a system represented by a differential equation can exhibit deterministic yet chaotic hopping that can be explained in terms of a one-dimensional mapping.

CHAPTER IV

SIMULATION OF THE NOISE RISE IN THREE-PHOTON JOSEPHSON PARAMETRIC AMPLIFIERS

A. Introduction

One interesting application of the Josephson junction is in the parametric amplification of weak electromagnetic signals, such as those encountered in radio astronomy. Several different research groups in recent years have attempted to construct devices suitable for this purpose (for a review of the field, see, for example, Levinsen et al., 1980). However, in most cases, there has been observed an undesirable side-effect: Namely, a noise temperature which is an increasing function of signal gain. Numerous theories have been proposed to explain this "noise rise," but all have proved unsatisfactory in one respect or another. One such theory which has received much attention recently is the suggestion that chaos is responsible for the noise rise (Huberman, Crutchfield, and Packard, 1980; Pedersen and Davidson, 1981). This chapter describes simulations which were performed to test this hypothesis in the case of the three-photon Josephson parametric amplifier (Miracky and Clarke, 1983). The significant and new approach of this study is the inclusion of thermal noise as well as a complete model of the amplifier circuit in the simulation model.

The chapter is organized as follows. We begin with a brief summary of the principles of operation of parametric amplifiers (paramps) in general. This is followed by a history of the experiments which have been performed on both three- and four-photon Josephson paramps. We then catalog the theories which have been proposed to explain the noise rise, with particular emphasis placed on the chaos explanation. In this

regard, we examine the relevant nonlinear dynamics of the simplest model of the paramp, a circuit whose equation is identical to that of the sinusoidally-driven, damped pendulum [Eq. (1.1)]. We shall highlight the conditions under which chaos is expected to occur. The bulk of this chapter will deal then with the simulation results. It will become clear then that the role of the thermal noise is essential to provide an explanation for the noise rise which is consistent with the published experimental results.

B. Historical Overview

1. Parametric Amplification

Any nonlinear reactance can be used as the active element in a parametric amplifier. Traditionally, the nonlinear capacitance of a varactor diode has been used. However, the Josephson junction is an attractive alternative in light of its lower potential noise temperature and lower pump power required to achieve the same gain (typically -70 dBm pump power in the case of the Josephson junction, versus -10 dBm for the varactor diode). To see how the Josephson junction can function as a paramp, we start with the Josephson equations:

$$V = (\Phi_0/2\pi)\,\dot{\delta} \tag{4.1a}$$

and

$$I = I_0 \sin \delta. \tag{4.1b}$$

Taking the time derivative of the second equation and substituting for $\dot{\delta}$ in the first yields:

$$V = L_J\, dI/dt, \text{ where } L_J = \Phi_0/(2\pi I_0 \cos \delta). \tag{4.2}$$

The Josephson junction is thus equivalent to a nonlinear inductance. Under the influence of a strong ac drive at the so-called "pump" frequency ω_p, the variation of the phase extends into the nonlinear portion of the L_J-versus-δ curve. A mixing results among the frequency compo-

nents present in the input, leading to sum and difference frequencies in the output. It is customary to restrict consideration to those circuits for which only a single difference frequency, or "idler", has significant power coupled out of the junction. There are two single idler modes of operation of a Josephson paramp, the three- and four-photon, corresponding to the allowed modes in the presence or absence of a dc-bias current, respectively. [See Levinsen et al., (1980) for an analytical discussion of this point.] The relationships between the relevant frequencies are:

$$\omega_p = \omega_s + \omega_i \text{ (three-photon)} \tag{4.3a}$$

and

$$2\omega_p = \omega_s + \omega_i \text{ (four-photon).} \tag{4.3b}$$

Here ω_s is the signal frequency, and ω_i is the idler frequency. The relationship between the various frequencies in the two modes, as well as an illustration of the amplification process, is given in Fig. 38. From practical considerations it is easier to supply a single matching circuit for the signal and idler in both modes, so experiments are usually designed such that these two frequencies are approximately equal. This is the usual "quasi-degenerate" form of parametric amplification. Hence, for the four-photon mode, $\omega_p \approx \omega_s \approx \omega_i$, and, for the three-photon mode, $(1/2)\omega_p \approx \omega_s \approx \omega_i$. By way of comparison, less power is required to achieve equal power gain in the three-photon mode, as the dc-bias current serves to more easily bias the phase into the nonlinear portion of the L_J-versus-δ curve. However, this advantage is offset by the need for two separate waveguides for the signal/idler and pump.

2. Experimental History

The Josephson paramp, operated in the four-photon mode, was first experimentally demonstrated by Feldman, Parish, and Chiao (1975). They

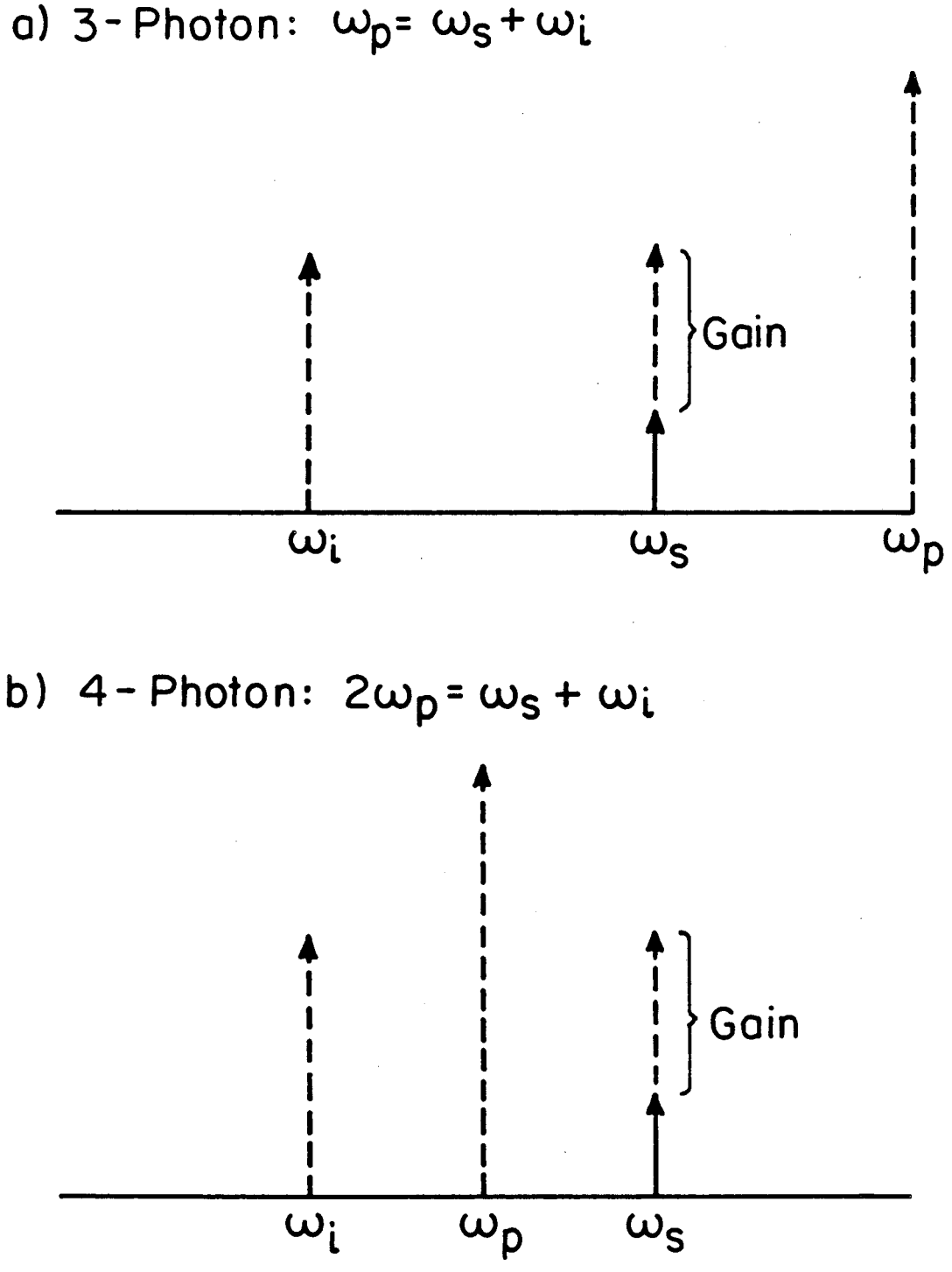

Figure 38. Schematic representation of parametric amplification in both (a) three- and (b) four-photon modes. ω_p, ω_s, and ω_i are the pump, signal, and idler frequencies respectively. The arrows indicate that the frequency components are monochromatic. The vertical scale is arbitrary.

showed gain at 37 GHz, using unbiased microbridges, and named their device the SUPARAMP (Superconducting Unbiased PARametric AMPlifier). Numerous researchers have subsequently extended the device technology. Taur and Richards (1977) have demonstrated comparable performance in a point contact pumped at 36 GHz. In an attempt to couple the relatively low impedance junction more efficiently to the characteristic waveguide impedance, Wahlsten, Rudner, and Claeson (1978) experimented with series-arrays of junctions operated at 10 Ghz. Although they generally found improved performance compared to individual junctions, they, like all of the others, were still plagued by the problem of noise rise.

The three-photon paramp was pioneered by several Danish researchers. Mygind et al. (1979) operated with low-noise performance at 35 GHz using a single junction. Although an extensive theory of amplification and noise performance in three-photon paramps was developed by Soerensen et al. (1980), it stopped short of explaining the observed noise rise. Thus, it was assumed that a single mechanism must be at work in producing the noise rise in both modes, in spite of the rather different amplification processes involved in the separate cases. The inability to understand and hence avoid the noise rise has prevented the Josephson paramp from widespread application. The need, however, still exists for improved low-noise high frequency amplifiers, regardless of the success of the superconductor-insulator-superconductor (SIS) mixer.

3. Theories of the Noise Rise

This phenomenon of the noise rise is nearly ubiquitous yet still remains unexplained. Ever since its first observation there have been attempts to uncover its origins. Simple linearized theories, even including thermal noise, fail to give a noise rise. Chiao et al. (1978) have

proposed a model of phase instability noise to explain the noise rise in the four-photon microbridge case, which seems in reasonable accord with experiments. However, the extension to finite capacitance, as for tunnel junctions, requires numerical or analog computer methods. Feldman and Levinsen (1981) have constructed a model which suggests that the paramps are susceptible to bias point instabilities, although they concede that their argument is "piecemeal and unrigorous."

The question of the noise rise has recently received renewed attention along with the widespread interest in nonlinear systems and chaos. Huberman, Crutchfield, and Packard (1980) first suggested that chaos might be the explanation for the noise in the four-photon case, and there has subsequently been a considerable literature on the subject. They studied the equation:

$$\ddot{\phi} + \dot{\phi}/\tau + \Omega_0^2 \sin \phi = \Gamma \sin \Omega t, \qquad (4.4)$$

which, like Eq. (1.1), is the equation for the driven, damped pendulum and the ac-biased Josephson tunnel junction. For $\tau = 5$, they found that complicated behavior set in for $\Omega/\Omega_0 \leq 0.8$ and $\Gamma \geq 0.6$. Such behavior included Feigenbaum period-doubling cascades followed by chaos, which manifested itself by the appearance of broad-band noise. Pedersen and Davidson (1981) concluded that chaos **could** indeed explain the noise rise in the four-photon amplifier, while Levinsen (1982) concluded that chaos **could not** be the explanation in **either** the three- or four-photon case. (However, Levinsen failed to observe a noise rise to begin with in his simulations.) Levinsen points out that an important aspect of the real amplifiers has usually been neglected in the other studies of chaotic behavior, namely the circuit that couples the signal to and from the junction.

Given this history of Josephson paramps and their noise rise, it is useful to summarize here the remaining unanswered questions and ambiguities. First, since the gain of the amplifier is intimately related to the impedance presented by the coupling circuit, any model that attempts to explain the noise rise must include this element. With the exception of Levinsen's (1982) inconclusive attempt, this has not been done. From a practical perspective, no experiment is ever performed without it, hence it is immaterial whether chaos is intrinsic to the bare junction system, or to the one including the (in general, reactive) coupling circuit. It is likely that these reactances alter the response of the junction to the pump signal enough such that comparisons between calculations based on the bare junction model and published experimental results will not be in good agreement. The need for simulation methods which address this question is apparent.

The second major shortcoming of previous studies has been the neglect of thermal noise in the simulations. As the experiments described in Chapter II (Miracky, Clarke, and Koch, 1983) have demonstrated, noise in systems close to bifurcations can result in rather drastic and unexpected consequences. It would seem then unwise to to ignore its effects a priori.

For these reasons, we have performed analog simulations of the three-photon mode, including a calibrated thermal noise source and a model for the coupling circuit. On the basis of these results, we identify the source of the noise rise in the three-photon case. We conclude the chapter with a brief discussion of the implications of this work for future device development.

C. Analog Simulations

The circuit model which we have simulated, first suggested by Levinsen (1982), is illustrated in Fig. 39. The junction itself was represented by the electronic analog described in Chapter II (Fig. 11). An active circuit (Fig. 40) was constructed to represent the ungrounded low-loss inductor in the coupling circuit. Voltage oscillators with large external series resistors served as the current sources. The pseudo-random number generator circuit described in Chapter II functioned as the thermal noise source. Passive elements were used to represent the remaining components of the circuit. We assume the resistively shunted junction model with $\beta_C = 2\pi I_0 R_J^2 C/\Phi_0 = 26.3$ for all simulations discussed here; I_0 is the critical current, $1/R_J$ is the quasiparticle conductance, and C is the self-capacitance.

We report here simulations for $\omega_p/\omega_0 = 1.12$, where $\omega_0 = \sqrt{(2\pi I_0/\Phi_0 C)}$ is the maximum plasma frequency. Although Kautz (1981b) states that chaotic solutions exist only for $1/R_J C \leq \omega_p \leq \omega_0$, we have discovered no significant difference between simulations for $\omega_p/\omega_0 = 1.12$, $\omega_p/\omega_0 = 0.93$, and $\omega_p/\omega_0 = 0.84$, except in the pump amplitude I_p required for maximum gain. In real parametric amplifiers, one generally uses a circulator to couple the signal into and out of the junction. We represent this element, as well as any other coupling reactances, in our model by a resonant circuit tuned to the signal frequency, $\omega_s = 1/\sqrt{(L'C')}$. We chose values of L', C', and of the series and load resistors R' and R_L to achieve a Q for the coupling circuit, $\sqrt{(L'/C')}/(R'+R_L)$, of about 20. We also maintained the conditions $R' = R_L$ and $R'+R_L \approx R_J$ necessary to achieve near-optimum noise performance (Soerensen et al., 1980). Finally, a white noise current $I_N(t)$ was included to represent the Johnson

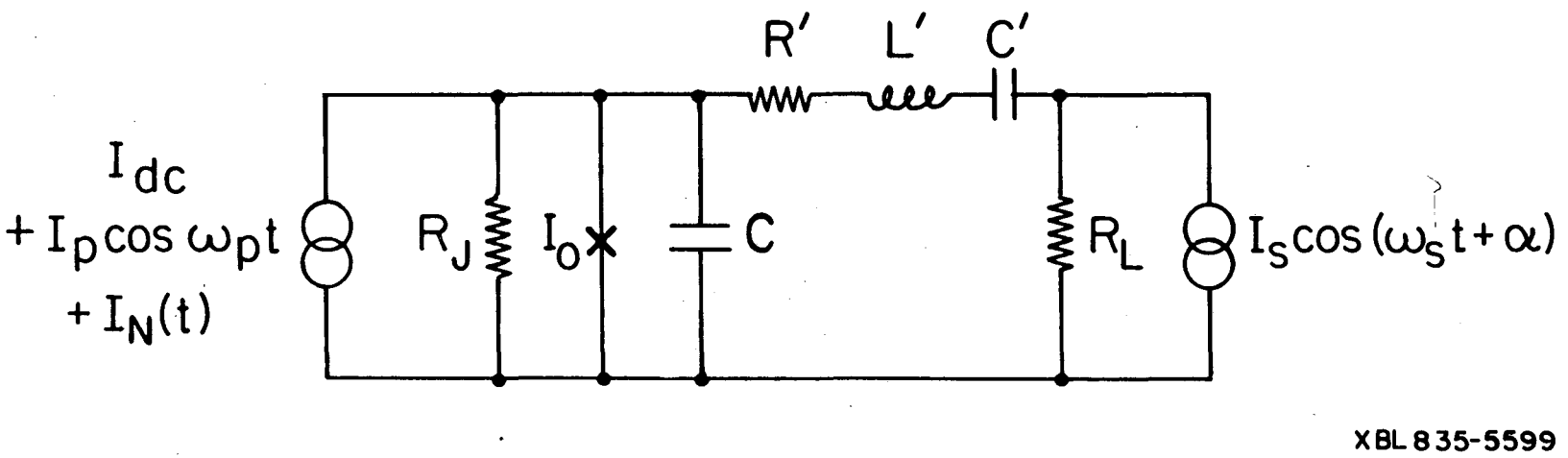

Figure 39. Circuit for analog simulation of three-photon Josephson parametric amplifier.

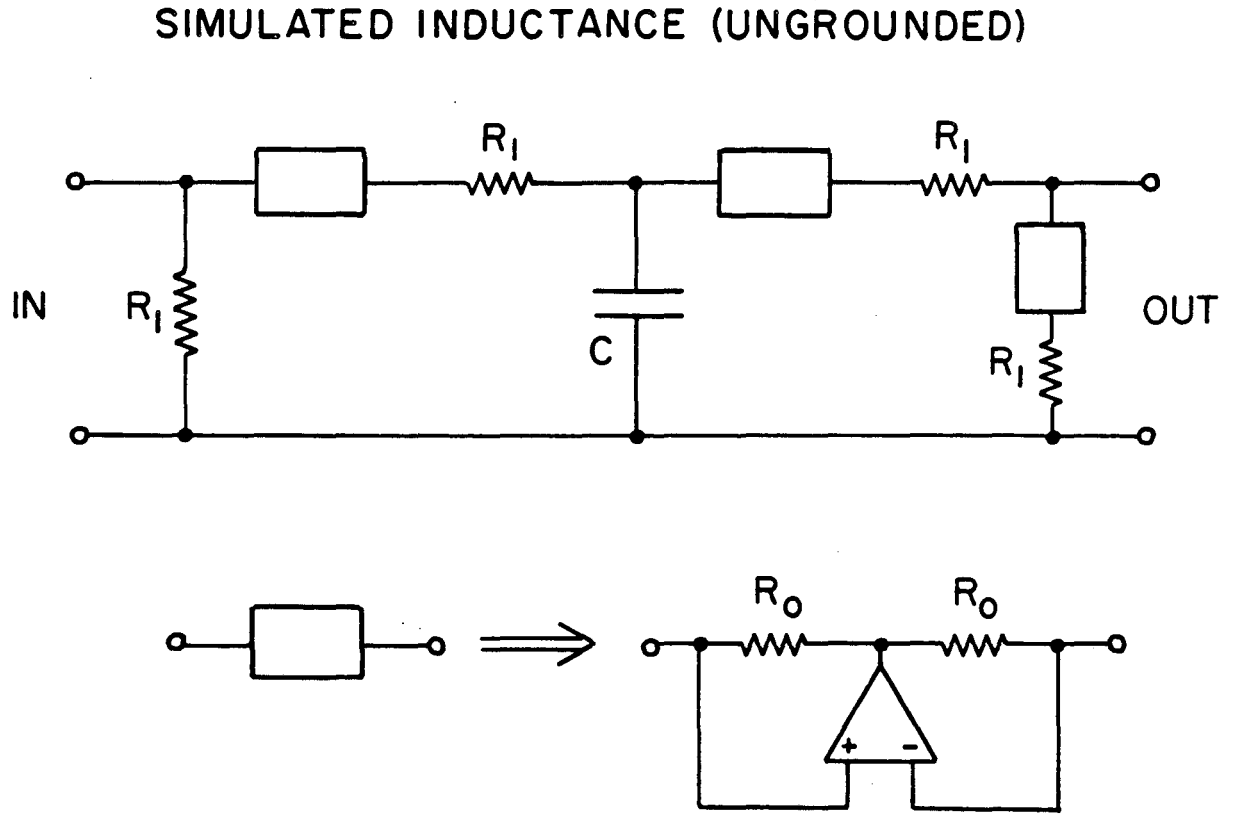

Figure 40. Circuit schematic for the active ungrounded inductance used in the simulations of the Fig. 39 circuit.

noise in the shunt conductance of the junction. The magnitude of this noise is characterized by $\Gamma = 2\pi k_B T/I_0\Phi_0$.

We followed the standard procedure in setting up the correct pump and dc-bias levels. With low pump power and a small signal at $\omega_s = \omega_p/2$, we adjusted the dc-bias current, I_{dc}, until signal gain and an idler at frequency $\omega_i = \omega_p - \omega_s \approx \omega_s$ were observed. We then increased the pump amplitude I_p, adjusting I_{dc} to achieve maximum gain. Maximum gain occurs when (Soerensen et al., 1980):

$$\omega_s = \omega_0[J_0(\eta)]^{1/2}[1 - (I_{dc}/I_0)^2]^{1/4},$$

where $\eta = 2eV_p/h\omega_p$ and V_p is the implicitly-defined voltage across the junction at the pump frequency.

Fig. 41 illustrates representative examples of our results. In Fig. 41(a), we plot the spectral density of the voltage across R_L for $I_p/I_0 = 0$ and $I_p/I_0 = 0.682$ (the point of maximum gain) in the absence of added thermal noise (the residual noise level corresponds to $\Gamma = 6.1\times10^{-7}$). The idler is approximately equal to the signal in amplitude, which is what one would expect from the Manley-Rowe relations (Loecherer and Brandt, 1982). The smaller peaks at frequencies below ω_i and above ω_s represent resonances associated with the coupling circuit (Getsinger and Matthaei, 1964). The signal gain G_S is 19.9 dB, while the noise gain G_N at frequency ω_s increases by 31 dB as I_p/I_0 is increased from zero to its value for maximum gain. (The signal gain G_S is the ratio of the power at $\omega = \omega_s$ for $I_p/I_0 = 0.682$ to that at $I_p/I_0 = 0$; the noise gain G_N is the ratio of the noise powers at $\omega \approx \omega_s$ for the same two pump levels.) For larger values of I_p or I_{dc}, a bifurcation occurs to an oscillation at $\omega_p/2$. This behavior is well-documented experimentally (Pedersen et al., 1980), and is a useful means of showing that the maximum

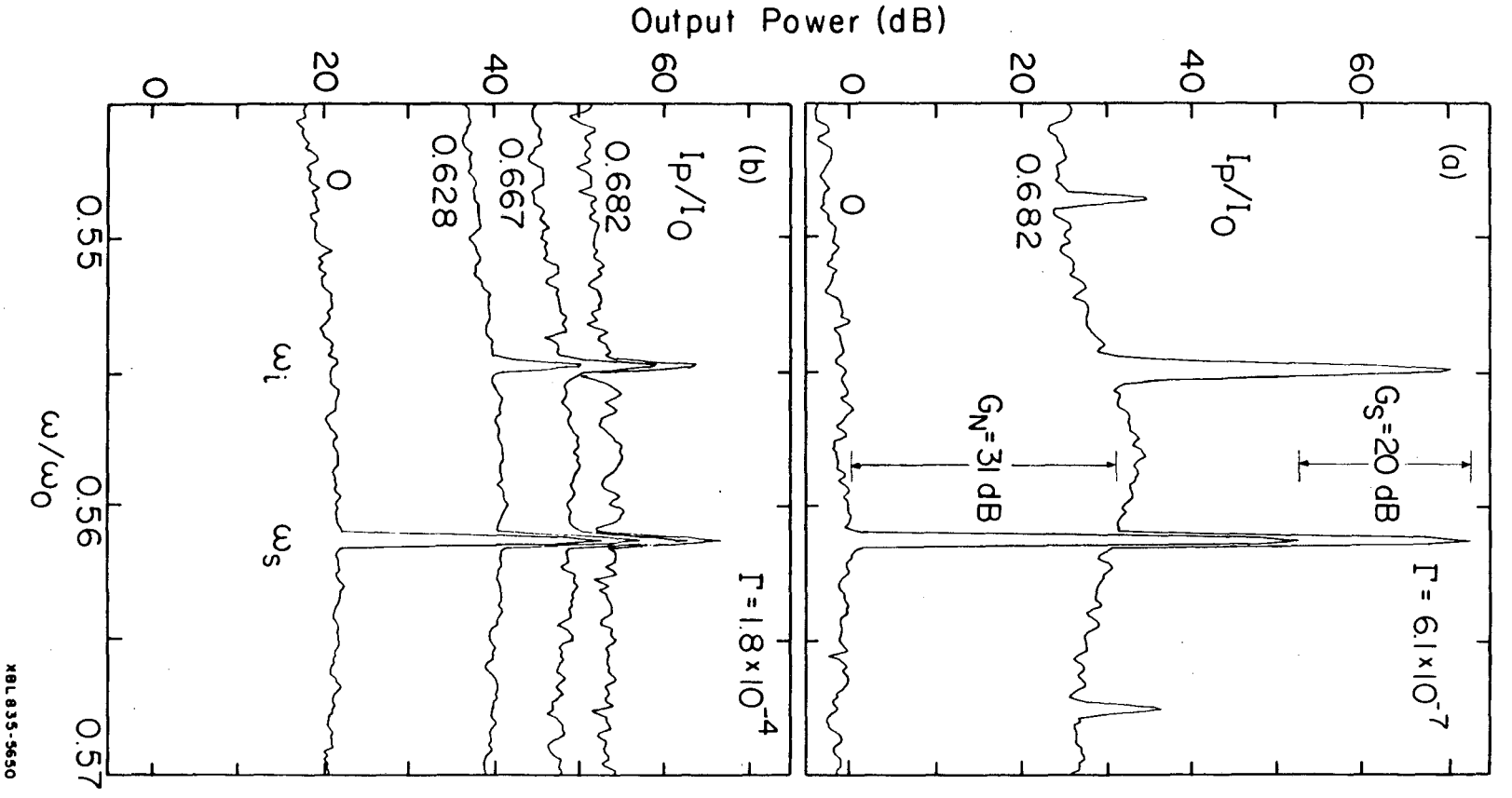

Figure 41. Spectral density of voltage across R_L for analog parametric amplifier with β_{C_7} = 26.3 and ω_p/ω_0 = 1.12 for various pump powers. In (a) $\Gamma = 6.1\times10^{-7}$ while in (b) $\Gamma = 1.8\times10^{-4}$. In both cases, the 0-dB reference level is the noise level at ω_s in (a).

gain condition has just been passed. At the bifurcation point, signal amplification drops sharply. Furthermore, there is **no** evidence for chaotic solutions at nearby bias points.

Figure 41(b) shows the results for the same range of pump amplitudes with $\Gamma = 1.8\times10^{-4}$, or T = 4.2 K for I_0 = 1 mA. The maximum signal gain decreased to 14.0 dB from its noise-free value of 19.9 dB. More importantly, the noise level near ω_s has increased far more sharply than the signal, by 32 dB as the gain is increased from unity to its maximum value.

An important issue in the history of both the three- and four-photon amplifiers has been the exact dependence of the noise temperature T_N on the signal gain G_S. To address this question, in Fig. 42 we plot G_N/G_S (a quantity proportional to T_N) vs G_S, where we varied G_S by varying I_p with I_{dc} kept fixed at its value for maximum gain. For $\Gamma = 6.1\times10^{-7}$ (upper curve) T_N rises somewhat as G_S rises to about 7 dB, and is constant for higher values of G_S. Thus, for $G_S > 7$ dB, T_N is independent of G_S, as one would expect for a useful amplifier. On the other hand, for $\Gamma = 1.8\times10^{-4}$ (lower curve), the noise temperature rises steadily as G_S is increased, by 18 dB as the gain increases from 0 to 14 dB. We note that T_N rises more rapidly than G_S for values of G_S below about 10 dB, and more slowly than G_S for higher values of G_S. This deviation from a linear relationship between T_N and G_S is very compatible with the experimental results of Mygind et al. (1979) for values of G_S up to about 8 dB. However, it is difficult to make meaningful comparisons of the magnitudes of T_N obtained from our simulations with those obtained from real devices without more accurate information on the parameters of the real junction and, in particular, of the coupling circuit (Levinsen

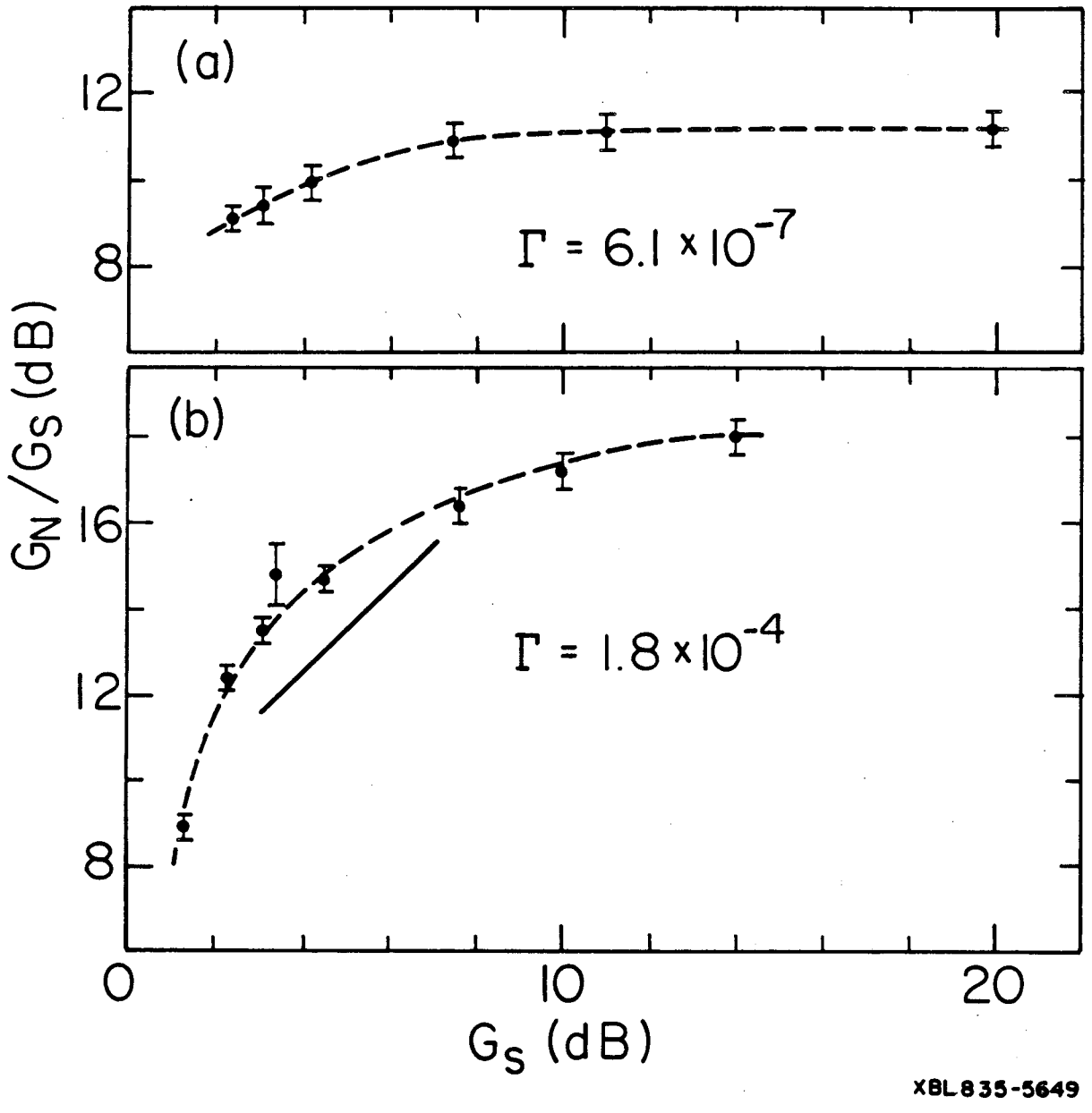

Figure 42. G_N/G_S (proportional to T_N) vs G_S for (a) $\Gamma = 6.1\times10^{-7}$ and (b) $\Gamma = 1.8\times10^{-4}$. Solid line represents T_N proportional to G_S.

et al., 1980; Soerensen et al., 1980).

To explore whether there is a well-defined threshold for the onset of the noise rise, we measured G_S and G_N for several values of Γ; the results are summarized in Table 4.1. Even for values of Γ as low as 0.42×10^{-5} (corresponding to a temperature of 0.1 K for I_0 = 1 mA), the noise rise is clearly present. The ratio G_N/G_S is almost independent of temperature over the range $0.1\ K \leq T \leq 0.42\ K$ (for I_0 = 1 mA). Thus, only a low level of thermal noise is necessary to trigger the noise rise.

D. Discussion

From these results, we can draw three conclusions about the noise rise in three-photon parametric amplifiers. First, chaos is excluded as a possible explanation. It is an inescapable fact that to achieve significant levels of gain the amplifier must be operated at values of bias current and pump power below the threshold for bifurcation to period two. The Feigenbaum period-doubling cascade, followed by chaos, does ensue for larger values of bias current and/or pump power. However, such phenomena occur well beyond the region of signal amplification and hence could not be a factor in practical devices. Second, the noise rise occurs only when a nonzero level of thermal noise is present. In the absence of noise, the system is uniquely in either the fundamental, unbifurcated mode below the infinite gain point, or in the bifurcated mode above it, depending on parameter values. Without noise, there can be no bridging of these two modes. Third, the noise rise is most likely the result of occasional hopping, induced by thermal noise, between a bias point in the unbifurcated region and an unstable one in the bifurcated region. Qualitatively, one would expect this picture to give rise

TABLE 4.1. Dependence of G_S, G_N, and G_N/G_S on level of thermal noise.

Γ ($\times 10^{-5}$)	G_S (dB)	G_N (dB)	G_N/G_S (dB)
0.061	19.9 $\pm$ 0.1	31.1 $\pm$ 1.1	11.2 $\pm$ 1.1
0.42	18.8 $\pm$ 0.1	36.6 $\pm$ 0.7	17.8 $\pm$ 0.7
4.2	16.7 $\pm$ 0.1	36.3 $\pm$ 0.7	19.6 $\pm$ 0.7
8.4	15.6 $\pm$ 0.1	34.7 $\pm$ 0.5	19.1 $\pm$ 0.5
18.0	14.0 $\pm$ 0.1	32.0 $\pm$ 0.7	18.0 $\pm$ 0.7

to a noise temperature that increases with gain: One increases the gain by biasing the amplifier nearer to the threshold for a period-doubling bifurcation, but the probability of noise-induced hopping unfortunately increases in tandem with it.

Finally, we emphasize that it is most unlikely that the specific mechanism we have presented here for the noise rise in the three-photon amplifier (noise effects near a period-doubling) accounts for the noise rise in the four-photon amplifier, for which the amplification process involves significantly different dynamics. If, however, the four-photon paramp possesses an instability of the **same** period as the pump near the infinite gain point, then thermal noise could trigger hopping between modes. It is conceivable that this could produce a noise rise in an analogous fashion.

E. Conclusions

We have shown that the noise rise in three-photon Josephson paramps is a consequence of noise-induced hopping near a dynamical instability, which, unfortunately, coincides with the infinite gain point. It would seem then that the noise rise is unavoidable in the three-photon paramp. It is possible though that at significantly lower temperatures (say, below 100 mK: see Table 4.1), the thermal noise alone might be below the threshold for the triggering of the hopping. However, at these temperatures, quantum noise originating in zero-point fluctuations in the shunting resistance (Koch, Van Harlingen, and Clarke, 1982) dominates thermal noise and may yet prevent satisfactory paramp performance. In either case, a dilution refrigerator would still be required, thus detracting from the attractiveness of the Josephson paramp vis-a-vis varactors or masers.

It is also possible that a suitable choice of parameters might result in adequate gain without a noise rise. For example, higher quality junctions (i.e., greater R_J's) might be helpful, as would a greater understanding of the role the coupling circuit reactances play in the circuit dynamics. At present, this is only speculation; further analyses and controlled experiments are needed to test these ideas.

We conclude this chapter by commenting on alternative approaches. Very recently, Silver et al. (1983) have suggested constructing paramps by shunting a junction with an external inductance (rf SQUID). Their analysis suggests that sufficient gain can be obtained under bias conditions far removed from the bifurcation threshold. Further experiments are needed though to demonstrate the utility of this type of paramp.

APPENDIX

CALCULATION OF PERIOD DOUBLING IN A JOSEPHSON CIRCUIT

We summarize in this Appendix analytic calculations performed by Wiesenfeld, Knobloch, Miracky, and Clarke (1984), which predict the first period-doubling bifurcation arising in Eq. (2.6) as i is reduced from a large value. These calculations, as will be shown, agree remarkably well with both analog simulations and digital computations. Moreover, the method used demonstrates a systematic scheme for achieving greater accuracy.

We start with Eq. (2.6):

$$\beta_L\beta_C\dddot{\delta} + \beta_C\ddot{\delta} + \dot{\delta}(1 + \beta_L\cos\delta) + \sin\delta = i. \tag{A.1}$$

It is known that for $i>1$, the junction voltage v possesses a dc component as well as an oscillatory part. Since $\dot{\delta} = v$ in these units, we write

$$\delta = \bar{v} + x(\tau), \tag{A.2}$$

where $\bar{v}$ is some constant, and x is a periodic function of time τ [see Eq. (2.3)]. Now introduce a new time u, defined as

$$u = \bar{v}\tau. \tag{A.3}$$

Then

$$\delta' = 1 + x', \tag{A.4}$$

where primes denote differentiation with respect to u. Equation (A.1) becomes:

$$\beta_L\beta_C\bar{v}^3x''' + \beta_C\bar{v}^2x'' + \bar{v}x' + \bar{v}\beta_L[\sin(u+x)]' + \sin(u+x) = i - \bar{v}. \tag{A.5}$$

Equation (A.5) is now analyzed using the method of harmonic balance (Jordan and Smith, 1977). Assuming that x is periodic, we write

$$x(u) = \sum_{n=1}^{\infty} A_n \sin(nu + \phi_n), \tag{A.6}$$

where A_n and ϕ_n are constants to be determined. After substituting (A.6) into (A.5) we balance coefficients of each Fourier mode independently. This leads to an infinite set of nonlinear coupled transcendental algebraic equations. It is expected that A_n diminishes as n increases, so for tractability we arbitrarily truncate the expansion (A.6) and solve the resulting equations. The lowest order approximation would be

$$x(u) = A_1 \sin(u + \phi_1), \tag{A.7}$$

implying

$$\delta(u) = u + A_1 \sin(u + \phi_1). \tag{A.8}$$

After substituting this into Eq. (A.5) and neglecting Bessel functions $J_m(A_1)$ for $m \geq 3$ (this is a good approximation for $A_1 \leq 1$), we obtain:

$$J_1 \sin\phi_1 = i - \bar{v}, \tag{A.9}$$

$$A_1\bar{v}(1 - \beta_L\beta_C\bar{v}^2) + \bar{v}\beta_L(J_0 - J_2)\cos\phi_1 - (J_0 + J_2)\sin\phi_1 = 0, \tag{A.10}$$

and

$$\beta_C\bar{v}^2 A_1 - \bar{v}\beta_L(J_0 + J_2)\sin\phi_1 + (J_2 - J_0)\cos\phi_1 = 0, \tag{A.11}$$

where the Bessel functions J_m are evaluated at A_1.

Given β_L, β_C, and i, these equations may be solved for $\bar{v}$, A_1, and ϕ_1. Figure 43 compares the results from an analog simulation of the Fig. 1 circuit with the values of $\bar{v}$ and A_1 obtained from Eqs. (A.9) - (A.11). Also shown are the results of integrating the evolution equation (A.1) directly on a digital computer, as was done in Chapter III. It is seen that the calculations reproduce remarkably well the values obtained from the digital computer, agreeing to within 1% over a wide range of parameter values. The analog circuit also gives 1-2% agreement for the quantity $\bar{v}$, while there is a systematic discrepancy of about 10% for the amplitude A_1. In both cases, the disagreement can be accounted for by the uncertainties involved in the analog measurements.

It is reasonable to presume that the agreement will become better as

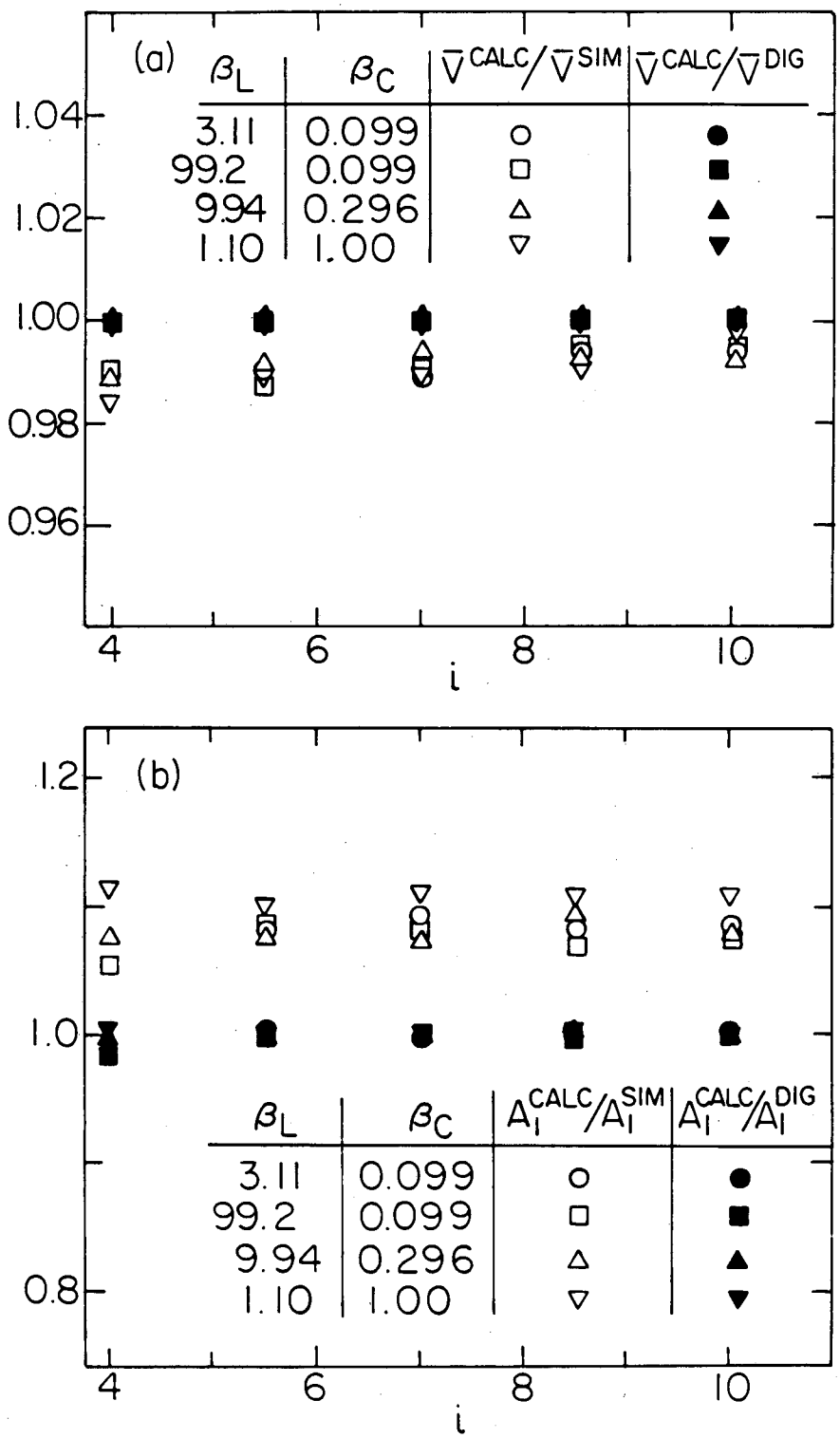

Figure 43. Comparison of harmonic balance calculations with analog simulations (open symbols) and digital computations (closed symbols) for a variety of parameter values. Results shown for (a) mean voltage $\bar{v}$ and (b) amplitude of phase oscillation A_1.

more terms in Eq. (A.6) are retained. If one uses

$$x(u) = A_1\sin(u + \phi_1) + A_2\sin(2u + \phi_2) \qquad (A.12)$$

instead of Eq. (A.7), five equations in the five unknowns $\bar{v}$, A_1, A_2, ϕ_1, and ϕ_2 are obtained. Figure 44 compares the ratio A_2/A_1 from this calculation with that obtained for the analog simulator using a power spectrum analyzer. Very good agreement is evident.

The stability of this basic oscillation $\delta_0(u)$ is tested by assuming a perturbation $\xi(u)$ about it, and then following its evolution. A stable or unstable basic oscillation would be identified by whether $\xi(u)$ decays or grows with time, respectively.

We start by substituting $\delta = \delta_0 + \xi$ into Eq. (A.1) and linearizing about δ_0. The following equation in ξ results:

$$\bar{v}^3\beta_L\beta_C\xi''' + \bar{v}^2\beta_C\xi'' + \bar{v}\xi' + \bar{v}\beta_L(\xi\cos\delta_0)' + \xi\cos\delta_0 = 0. \qquad (A.13)$$

This equation can be analyzed using Floquet theory (Jordan and Smith, 1977). For an equation with real coefficients, such as (A.13), three possibilities are allowed: period-doubling instabilities, period-one instabilities, and Hopf instabilities. In fact, only the former are possible in Eq. (A.1) (Wiesenfeld et al., 1984). In this case, the basic oscillation $\delta_0(u)$ period doubles [i.e., a perturbation $\xi(u)$ possessing components at frequencies mu/2 (m an odd integer) is not damped out] if a real Floquet multiplier becomes less than -1.

To determine whether a period doubling occurs for a given set of parameters β_L, β_C, and i, first the basic oscillation $\delta_0(u)$ is computed. Then a perturbation $\xi(u)$ of the form

$$\xi(u) = \sum_{m \text{ odd}} [\gamma_m\cos(mu/2) + \alpha_m\sin(mu/2)] \qquad (A.14)$$

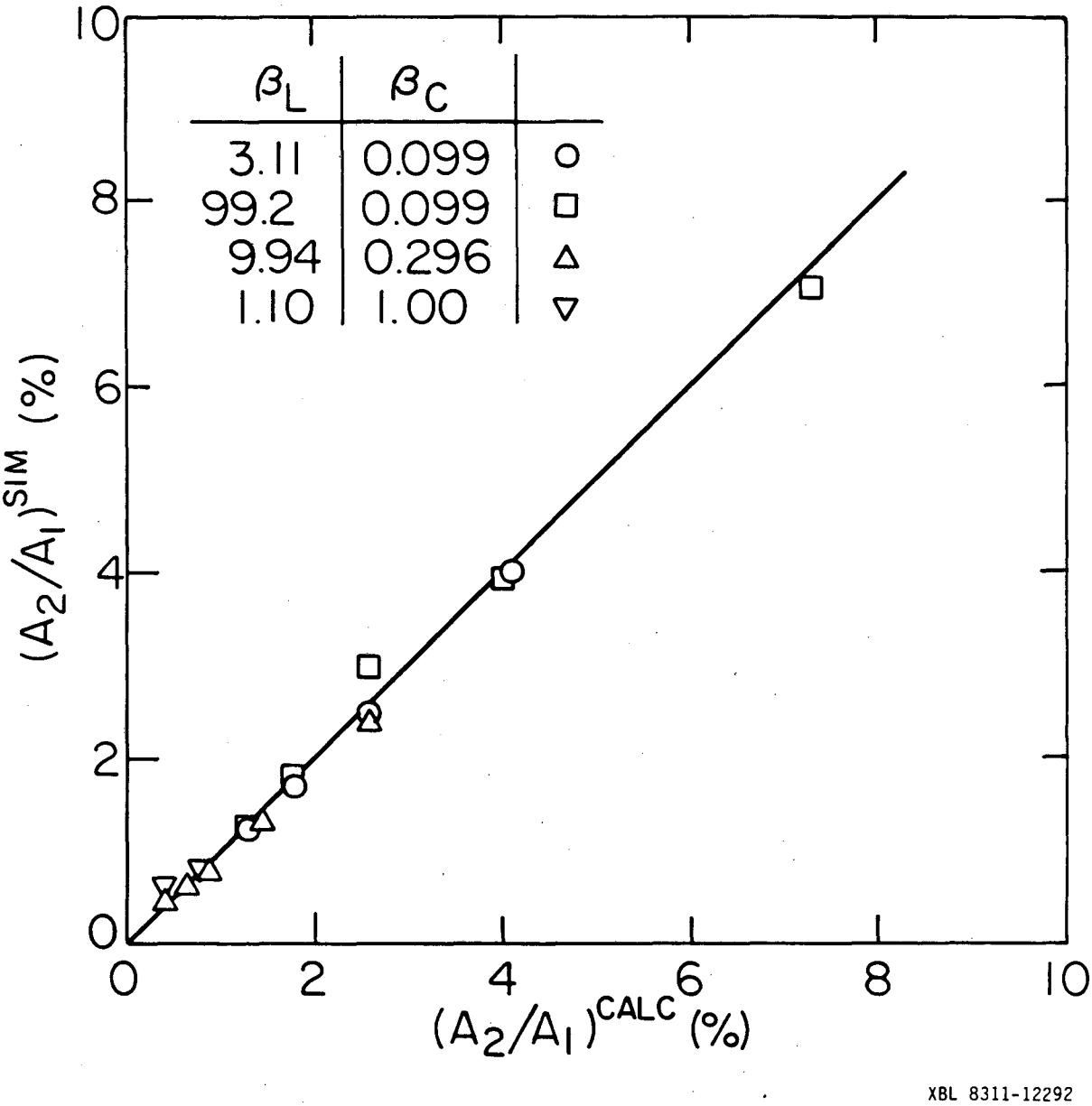

Figure 44. Ratio of second-harmonic amplitude A_2 to first-harmonic amplitude A_1 for analog simulations vs harmonic balance calculations.

is assumed, and substituted into Eq. (A.13). Period doubling is signalled when the determinant of the coefficient matrix, obtained when the Fourier components of Eq. (A.13) are matched, vanishes.

Figure 45 compares the results of this calculation with both digital computations and analog simulations for $\beta_C=0.0986$, giving the critical value of bias current $i=i_{crit}$ for the onset of period doubling for various values of β_L. In order to obtain accurate results, it is important that an accurate representation of δ_0 be used. The figure presents two theoretical curves. The solid line uses the crudest approximation for δ_0, obtained by assuming the existence of only the single harmonic [see Eq. (A.8)] in the basic oscillation. The dashed-dotted curve (see inset) assumes Eq. (A.12) to obtain better estimates of A_1, ϕ_1, and $\bar{v}$, but still uses Eq. (A.8) for the period-doubling part of the calculation. Obviously, these are only the first of a systematic sequence of calculations which should converge to the exact answer. From Fig. 45 we see that good accuracy is already achieved for the crudest approximation, the more refined approach becoming important for higher values of β_L. The first correction accounts for about one-third of the discrepancy between the calculation and the digital integration for $\beta_L=14$.

The results of the analog simulations agree with the results of the digital computations and analytical calculation to a much greater accuracy in Fig. 45 than one might have expected from the results summarized in Fig. 43(b). As this agreement is more consistent with the results in Fig. 43(a), we conclude that it is the oscillation **frequency**, rather than the amplitude, which is of greatest importance in determining when period doubling sets in.

An interesting feature predicted by our calculation is that there is

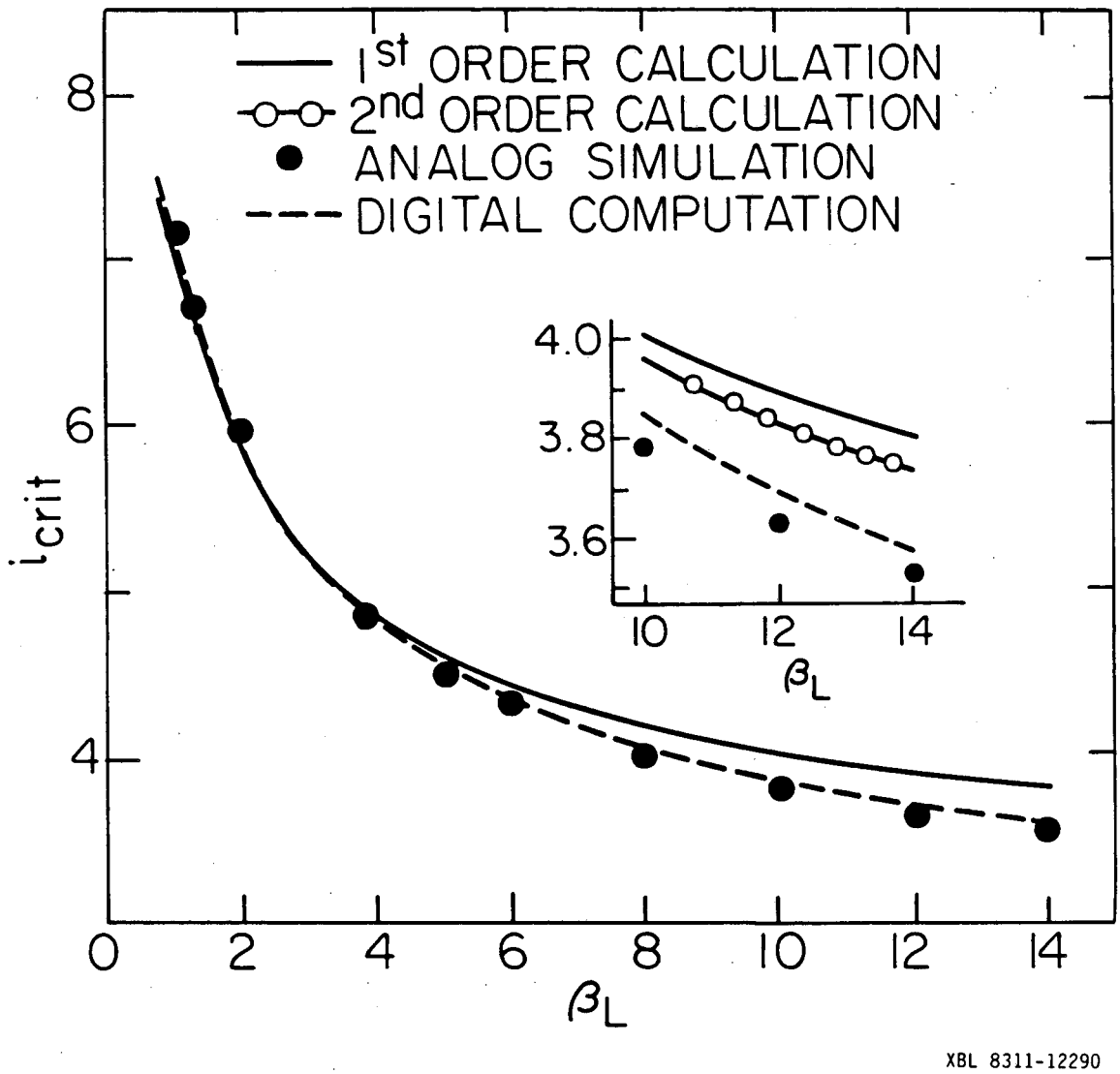

Figure 45. Onset of period doubling: i_{crit} vs β_L for $\beta_C = 0.0986$. Solid curve represents calculations based on the first-order approximation Eq. (A.7), while the dashed-dotted curve (inset) uses the second-order approximation Eq. (A.12). Dashed line gives the results of digital computations, while the solid circles are from analog simulations.

a minimum value of $\beta_L=\beta_{L,min}$ (for fixed β_C) for which the period-doubling instability can occur. This behavior is also observed in the analog simulations. For $\beta_C=0.1$, we find the theoretical value $\beta_{L,min}=0.72$ as compared with the value determined from the analog simulation $0.77<\beta_{L,min}<0.84$.

REFERENCES

1) Abramowitz, M. and I.A. Stegun (eds.), 1964, "Handbook of Mathematical Functions," National Bureau of Standards, Washington, D.C.

2) Arecchi, F.T. and F. Lisi, 1982, Hopping mechanism generating 1/f noise in nonlinear systems, Phys. Rev. Lett. 49, 94.

3) Barone, A. and G. Paterno, 1982, "Physics and Applications of the Josephson Effect," John Wiley and Sons, New York.

4) Beasley, M.R., D. D'Humieres, and B.A. Huberman, 1983, Comment on "Hopping mechanism generating 1/f noise in nonlinear systems," Phys. Rev. Lett. 50, 1328.

5) Ben-Jacob, E., I. Goldhirsch, Y. Imry, and S. Fishman, 1982, Intermittent chaos in Josephson junctions, Phys. Rev. Lett. 49, 1599.

6) Berge, P., M. Dubois, P. Manneville, and Y. Pomeau, 1980, Intermittency in Rayleigh-Benard convection, J. Phys. (Paris) 41L, 341.

7) Calander, N., T. Claeson, and S. Rudner, 1981, A subharmonic Josephson relaxation oscillator--amplification and locking, Appl. Phys. Lett. 39, 504.

8) -----, 1982a, Relaxation oscillations in inductively shunted Josephson tunnel junctions, Physica Scripta 25, 837.

9) -----, 1982b, Shunted Josephson tunnel junctions: High frequency, self-pumped low noise amplifiers, J. Appl. Phys. 53, 5093.

10) Chiao, R.Y., M.J. Feldman, D.W. Petersen, B.A. Tucker, and M.T. Levinsen, 1978, Phase instability noise in Josephson junctions, in "Future Trends in Superconductive Electronics," A.I.P. Conf. Proc. 44, New York.

11) Claeson, T., 1983, Superconducting tunnel junctions in high frequency radiation detectors, in "Advances in Superconductivity,"

B. Deaver and J. Ruvalds (eds.), Plenum Press, New York.

12) Clarke, J., 1980, Advances in SQUID magnetometers, IEEE Trans. Electron Devices ED-27, 1896.

13) Dempsey, D.G., M.T. Levinsen, and B.T. Ulrich, 1975, Energy storage and subharmonic oscillations in Josephson junctions, IEEE Trans. Magn. MAG-11, 811.

14) D'Humieres, D., M.R. Beasley, B.A. Huberman ,and A. Libchaber, 1982, Chaotic states and roads to chaos in the forced pendulum, Phys. Rev. A26, 3483.

15) Dubois, M., M.A. Rubio, and P. Berge, 1983, Experimental evidence of intermittencies associated with a subharmonic bifurcation, Phys. Rev. Lett. 51, 1446.

16) Dutta, P. and P.M. Horn, 1981, Low-frequency fluctuations in solids: 1/f noise, Rev. Mod. Phys. 53, 497.

17) Eckmann, J.-P., 1981, Roads to turbulence in dissipative dynamical systems, Rev. Mod. Phys. 53, 643.

18) Feigenbaum, M.J., 1978, Quantitative universality for a class of nonlinear transformations, J. Stat. Phys. 19, 25.

19) -----, 1979, The universal metric properties of nonlinear transformations, J. Stat. Phys. 21, 669.

20) Feldman, M.J. and M.T. Levinsen, 1981, Theories of the noise rise in Josephson PARAMPS, IEEE Trans. Magn. MAG-17, 834.

21) Feldman, M.J., P.T. Parrish, and R.Y. Chiao, 1975, Parametric amplification by unbiased Josephson junctions, J. Appl. Phys. 46, 4031.

22) Geisel, T. and J. Nierwetberg, 1984, Intermittent diffusion: A chaotic scenario in unbounded systems, Phys. Rev. A29, 2305.

23) Getsinger, W.J. and G.L. Matthaei, 1964, Design of up-converters

and parametric amplifiers, IEEE Trans. Microwave Theory Tech. MTT-12, 77.

24) Gibbs, H.M., F.A. Hopf, D.L. Kaplan, and R.L. Shoemaker, 1981, Observation of chaos in optical bistability, Phys. Rev. Lett. 46, 474.

25) Goldhirsch, I., Y. Imry, G. Wasserman, and E. Ben-Jacob, 1984, Studies of the intermittent-type chaos in ac- and dc-driven Josephson junctions, Phys. Rev. B29, 1218.

26) Guckenheimer, J. and P.J. Holmes, 1983, "Nonlinear Oscillations, Dynamical Systems, and Bifurcations of Vector Fields," Springer-Verlag, New York,.

27) Gwinn, E.G. and R.M. Westervelt, 1984, Intermittency and low frequency noise in the damped driven pendulum, submitted to the 17th International Conference on Low Temperature Physics, Karlsruhe.

28) Huberman, B.A., J.P. Crutchfield, and N.H. Packard, 1980, Noise phenomena in Josephson junctions, Appl. Phys. Lett. 37, 750.

29) Ito, K., 1980, Chaos in the Rikitake two-disc dynamo system, Earth Plane. Sci. Lett. 51, 451.

30) Jordan, D.W. and P. Smith, 1977, "Nonlinear Ordinary Differential Equations," Oxford University Press, Oxford.

31) Josephson, B.D., 1962, Possible new effects in superconductive tunneling, Phys. Lett. 1, 251.

32) Kautz, R.L., 1981a, The ac Josephson effect in hysteretic junctions: Range and stability of phase lock, J. Appl. Phys. 52, 3528.

33) -----, 1981b, Chaotic states of rf-biased Josephson junctions, J. Appl. Phys. 52, 6241.

34) Koch, R.H., D.J. Van Harlingen, and J. Clarke, 1982, Measurements of quantum noise in resistively shunted Josephson junctions,

Phys. Rev. B26, 74.

35) Koch, R.H., R.F. Miracky, and J. Clarke, 1984, unpublished.

36) Lambert, J.D., 1973, "Computational Methods in Ordinary Differential Equations," John Wiley and Sons, New York.

37) Levinsen, M.T., N.F. Pedersen, O.H. Soerensen, B. Dueholm, and J. Mygind, 1980, Externally pumped millimeter-wave Josephson junction parametric amplifier, IEEE Trans. Electron Devices ED-27, 1928.

38) Levinsen, M.T., 1982, Even and odd subharmonic frequencies and chaos in Josephson parametric junctions: Impact on parametric amplifiers?, J. Appl. Phys. 53, 4294.

39) Loecherer, K.-H. and C.-D. Brandt, 1982, "Parametric Electronics," Springer-Verlag, Berlin.

40) Mandelbrot, B.B., 1977, "Fractals: Form, Chance, and Dimension," Freeman and Co., San Francisco.

41) Manneville, P., 1980, Intermittency, self-similarity, and 1/f spectrum in dissipative dynamical systems, J. Phys. (Paris) 41, 1235.

42) Manneville, P. and Y. Pomeau, 1979, Intermittency and the Lorenz model, Phys. Lett. A75, 1.

43) -----, 1980, Different ways to turbulence in dissipative dynamical systems, Physica (Utrecht) 1D, 219.

44) May, R.M., 1976, Simple mathematical models with very complicated dynamics, Nature (London) 261, 459.

45) Metropolis, N., M.L. Stein, and P.R. Stein, 1973, On finite limit sets for transformations on the unit interval, J. Combinatorial Theory 15A, 25.

46) Miracky, R.F., J. Clarke and R.H. Koch, 1983, Chaotic noise observed in a resistively shunted self-resonant Josephson tunnel

junction, Phys. Rev. Lett. 50, 856.

47) Miracky, R.F. and J. Clarke, 1983, Simulation of the noise rise in three-photon Josephson parametric amplifiers, Appl. Phys. Lett. 43, 508.

48) Miracky, R.F., M.H. Devoret, and J. Clarke, 1984, Deterministic hopping in a Josephson circuit described by a one-dimensional mapping, submitted to Phys. Rev. A.

49) Mygind, J., N.F. Pedersen, O.H. Soerensen, B. Dueholm, and M.T. Levinsen, 1979, Low-noise parametric amplification at 35 GHz in a single Josephson tunnel junction, Appl. Phys. Lett. 35, 91.

50) Newhouse, S., D. Ruelle, and F. Takens, 1978, Occurrence of strange axiom A attractors near quasi-periodic flows on T^m, $m \geq 3$, Commun. Math. Phys. 64, 35.

51) Octavio, M. and C. Readi Nasser, 1984, Chaos in a dc bias Josephson junction in the presence of microwave radiation, to be published in Phys. Rev. Lett.

52) Ott, E., 1981, Strange attractors and chaotic motions of dynamical systems, Rev. Mod. Phys. 53, 655.

53) Pedersen, N.F., O.H. Soerensen, B. Dueholm, and J. Mygind, 1980, Half-harmonic parametric oscillations in Josephson junctions, J. Low Temp. Phys. 38, 1.

54) Pedersen, N.F. and A. Davidson, 1981, Chaos and noise rise in Josephson junctions, Appl. Phys. Lett. 39, 830.

55) Pomeau, Y. and P. Manneville, 1980, Intermittent transition to turbulence in dissipative dynamical systems, Commun. Math. Phys. 74, 189.

56) Procaccia, I. and H. Schuster, 1983, Functional renormalization-

group theory of universal 1/f noise in dynamical systems, Phys. Rev. A28, 1210.

57) Silver, A.H., R.D. Sandell, J.P. Hurrell, and D.C. Pridmore-Brown, 1983, SQUID parametric amplifier, IEEE Trans. Magn. MAG-19, 622.

58) Silver, A.H., R.D. Sandell, and J.Z. Wilcox, 1983, SQUID Voltage controlled oscillator, IEEE Trans. Magn. MAG-19, 625.

59) Soerensen, O.H., B. Dueholm, J. Mygind, and N.F. Pedersen, 1980, Theory of the singly quasidegenerate Josephson junction parametric amplifier, J. Appl. Phys. 51, 5483.

60) Sullivan, D.B., R.L. Peterson, V.E. Kose, and J.E. Zimmerman, 1970, Generation of harmonics and subharmonics of the Josephson oscillation, J. Appl. Phys. 41, 4865.

61) Taur, Y. and P.L. Richards, 1975, Relaxation oscillations in point-contact Josephson junctions, J. Appl. Phys. 46, 1793.

62) Taur, Y. and P.L. Richards, 1977, Parametric amplification and oscillation at 36 GHz using a point contact Josephson junction, J. Appl. Phys. 48, 1321.

63) Taylor, B.N., W.H. Parker, D.N. Langenberg, and A. Denestein, 1967, On the use of the ac Josephson effect to maintain standards of electromotive force, Metrologia 3, 89.

64) Teitsworth, S.W., R.M. Westervelt, and E.E. Haller, 1983, Nonlinear oscillations and chaos in electrical breaksown in Ge, Phys. Rev. Lett. 51, 825.

65) Testa, J., J. Perez, and C. Jeffries, 1982, Evidence for universal chaotic behavior of a driven oscillator, Phys. Rev. Lett. 48, 714.

66) Tritton, D.J., 1977, "Physical Fluid Dynamics," Van Nostrand-Reinhold, New York.

67) Voss, R.F., 1983, Comment on "Hopping mechanism generating 1/f noise in nonlinear systems," Phys. Rev. Lett. 50, 1329.

68) Wahlsten, S., S. Rudner, and T. Claeson, 1978, Arrays of Josephson tunnel junctions as parametric amplifiers, J. Appl. Phys. 49, 4248.

69) Wiesenfeld, K., E. Knobloch, R.F. Miracky and J. Clarke, 1983, Calculation of period-doubling in a Josephson circuit, Phys. Rev. A29, 2102.

70) Zappe, H.H., 1983, Josephson computer technology, in "Advances in Superconductivity," B. Deaver and J. Ruvalds (eds.), Plenum Press, New York.

71) Zimmerman, J.E. and A.H. Silver, 1967, Coherent radiation from high-order quantum transitions in small-area superconducting contacts, Phys. Rev. Lett. 19, 14.

TECHNICAL INFORMATION DEPARTMENT
LAWRENCE BERKELEY LABORATORY
UNIVERSITY OF CALIFORNIA
BERKELEY, CALIFORNIA 94720